THE UNIVERSITY OF CALGARY

The Acceleration of Low Energy Charged Particles at Interplanetary Shock Waves

BY

James M. Murtha

A THESIS

SUBMITTED TO THE FACULTY OF GRADUATE STUDIES

IN PARTIAL FULFILLMENT OF THE REQUIREMENTS FOR THE

DEGREE OF MASTER OF SCIENCE

DEPARTMENT OF PHYSICS

CALGARY, ALBERTA

March, 1989

ISBN 0-315-50361-0

THE UNIVERSITY OF CALGARY

FACULTY OF GRADUATE STUDIES

The undersigned certify that they have read, and recommend to the Faculty of Graduate Studies for acceptance, a thesis entitled, "The Acceleration of Low Energy Charged Particles at Interplanetary Shock Waves" submitted by James M. Murtha in partial fulfillment of the requirements for the degree of Master of Science.

Supervisor, Dr. D. Venkatesan
Department of Physics
University of Calgary

Dr. R.B. Hicks
Department of Physics
University of Calgary

Dr. J.W. Haslett
Department of Electrical Engineering
University of Calgary

Date March 6, 1989

Abstract

This thesis investigates the acceleration of low energy charged particles in the heliosphere as a result of the passage of an interplanetary shock wave. Some form of shock acceleration seems to be the most promising means to account for observations of particle fluxes therein.

Available Voyager 2 spacecraft data reveal the existence of three recurrences of two corotating shock pairs during the time period of 1979, DOYS 100-180. The evidence supporting this is presented for the first time. The effects of the shock passages are seen in the Voyager 2 Low Energy Charged Particle experiment (30.0-3500 keV/ion). The evolution of the energy spectrum through the time of the shock passages indicates an efficient means of acceleration in the lower energy channels of the spacecraft sensor, with a source population whose energies are < 35 keV. The sectored particle data, accumulated in eight 45° sectors of the LECP scan plane, were transformed to the co-moving plasma frame and are presented in both the up and downstream regions of one of the candidate shock events. The anisotropic distributions in these regions are seen to coincide with those discussed in the literature. The results indicate an upstream field-aligned particle flow away from the shock and a particle distribution peaked perpendicular to the field downstream.

In addition, an attempt was made to simulate the forward shock indicated by the Voyager 2 data at DOY 138, hour 01. The computer simulation used superimposed a zero-mean, perpendicular random magnetic field component upon a mean field component in both the up and downstream regions, thus providing the opportunity for pitch angle scattering and therefore extended particle–shock

interaction times. The simulation numerically integrates, fully relativistically, the Lorentz force equation describing the motion of a charged particle in the presence of electromagnetic fields. The parameters used in the simulation that were critical to the acceleration process are presented, and the basis of their choice and extent of their validity are discussed.

The comparison between the real and simulated angular distributions in the vicinity of the shock is quantified by the use of the Spearman rank-order correlation coefficient. It is found that there is better agreement between the real and simulated upstream data than is displayed in the downstream data. A large, anti-shockward particle anisotropy is observed upstream of the shock in both the real and simulated data, consistent with shock drift theory. Upstream, it is found that particles whose energies lie in the PL01–PL04 energy range (30—215 keV/nucleon) are more influenced by the passage of the shock, in both the real and simulated data. The degree of anisotropy found in the simulated data is much larger than that observed in the real data, particularly at these lower energy ranges. The lack of an expected field-perpendicular downstream particle anisotropy in the simulated data remains a puzzle, and possible reasons for this are suggested. The good correspondence seen between the simulated and observed angular distributions upstream of the shock wave lends support to the shock acceleration theory expected to be applicable in this situation.

Acknowledgements

The list of people who contributed to the writing of this thesis, either directly or indirectly, must be recognized. For without the help of any of the following people, the completion of the work would be either made much more difficult or, in some instances, impossible.

I would like to thank the Department of Physics at the University of Calgary for providing support in the form of Graduate Teaching Assistantships during my time as a graduate student, and for summer support, travel, and accommodation at the Johns Hopkins University/Applied Physics Laboratory in the form of NSERC (Ottawa) grant A69-1565. In addition, I would like to thank the departments of Academic Computing Services and SuperComputing Services at the University of Calgary for their support during the analysis and simulation phases of this study.

I am indebted to the people of the Space Science Group at the JHU/APL; particularly to Dr. S.M. Krimigis for use of the Voyager data and his willingness to allow physics undergraduates to experience first hand the excitement of applied science, and to Dr. R.B. Decker for his infinite patience in answering the many questions of a excited physics undergraduate experiencing applied science for the first time. I would like to thank Dr. Robb Decker especially for the use of his model simulation, the results of which are presented within. Support was also provided through JHU/APL subcontract 601566 to Dr. D. Venkatesan.

During my stay over two 4 month periods (May - September, 1985 and 1986), and two subsequent week-long trips, incredible hospitality was provided by Mr. and Mrs. L. Sturm, Mr. and Mrs. R. Johnson, and Mrs. Jackie Weitzel. The

friendliness of each of these people was very much appreciated during my trips to Laurel, Maryland.

Most importantly, I would like to thank my graduate supervisor, Dr. D. Venkatesan, for providing the opportunity to study and work in a facility such as the JHU/APL as a participant in his collaborative programs with Dr. S.M. Krimigis. His guidance during this time was instrumental in my success as a graduate student at the University of Calgary.

Dedication

For

all my

friends.

Contents

List of Tables

List of Figures

Chapter 1

THE HELIOSPHERE

1.1 The Solar Influence

The Sun is, of course, the most dominant physical body in the Solar System. It is not surprising then that a study involving the acceleration of charged particles in the heliosphere (by definition, *the region of the solar influence*) should start with a brief review of the physical processes involving the Sun. It will be seen that the modulation of cosmic rays in the heliosphere is a direct result of, and depends very sensitively upon, processes continuously ongoing within and around the Sun.

The *in situ* observations of heliospheric plasmas and magnetic fields provided by the Pioneer spacecraft since 1973 and by the Voyager spacecraft nearly one half of a solar cycle later in 1977 have provided investigators with a wealth of information. The refinement of existing theories as well as the development of many others has been an ongoing process since this time. Many reviews have been written which are specifically concerned with the plasmas and fields as detected by these spacecraft *(Burlaga, 1984; Smith and Wolfe, 1979; Smith and Wolfe, 1977; Axford, 1977; Burlaga, 1971)*. Features of these reviews will be dealt with, where appropriate, throughout this thesis.

The present model of the interplanetary magnetic field within the heliosphere will be outlined in a later section. However, it is first necessary to understand the physical interaction between the solar wind and the solar magnetic field. The

physics involving the description of the solar wind are to be reviewed in the next section. These relations will aid in understanding the latter chapters.

1.1.1 The Solar Wind

It will be shown explicitly in the next section that a highly conducting plasma, such as the solar wind, in motion with respect to a magnetic field will result in a physical coupling between the fluid flow and the conceptual magnetic field lines. It is because of the presence of this magnetic field that the equations of magnetohydrodynamics, rather than those of ordinary hydrodynamics, are used in the general description of the heliosphere. Both magnetohydrodynamics and hydrodynamics are a subset of a branch of physics referred to as continuum mechanics, which attempts to describe the macroscopic properties of a fluid, the solar wind plasma in the present case.

Continuum mechanics abandons the concept of the dynamics of individual particles within the fluid it is attempting to describe. Rather, it is the dynamics of an *element* of the fluid which is of concern. Local variables such as density, velocity and energy are defined as continuous functions of time and space. The dependent variables of magnetohydrodynamics (MHD) are the bulk velocity, mass density and pressure.

There exists an elegant mathematical formalism which connects the observed features of the particles constituting the fluid, the charge and energy, with the macroscopic variables of the MHD theory. This connection is via the concept of the dynamical *phase space* and the particle *phase space distribution function*. These are concepts familiar in the fields of statistical mechanics and the kinetic

theory of gases.

In this framework, the positions and momenta of the particles are denoted by q_i and p_i, where i refers to the components of the vectors $\vec{q}$ and $\vec{p}$ *(Goldstein, 1980; McQuarry, 1976)*. Therefore, for N such particles there is defined a $6N$-dimensional phase space in the coordinates $(q_1, q_2, \ldots, q_{3N}, p_1, p_2, \ldots, p_{3N})$. One point in this phase space, a *phase point*, describes the microscopic dynamical state of the system at some instantaneous time. The distribution of the particles within this $6N$-dimensional phase space is described by a function $f(q_j, p_j, t), j = 1, \ldots, 3N$. This function can be construed as a density of phase points such that $f(q_j, p_j, t)dq_j dp_j$ is the number of particles whose coordinates in the phase space are between (q_j, p_j) and $(q_j + dq_j, p_j + dp_j)$. Note that the distribution function $f(q_j, p_j, t)$ has an explicit dependence on time as well as an implicit dependence through the variables $q_j(t)$ and $p_j(t)$.

The number density, ρ_n, of particles in the system is obtained by integrating over momentum space:

$$\rho_n(q,t) = \int f(q,p,t)dp \tag{1.1}$$

where the subscript j has been dropped for convenience; it is understood that there are $3N$ values of the variables q and p. The total number of particles in the system is then obtained by integrating over all phase space:

$$N = \int\int f(q,p,t)dqdp \tag{1.2}$$

It is easily shown that the number of phase points in an arbitrary phase volume,

$\mathcal{V}$, is a conserved quantity. The number of phase points within $\mathcal{V}$ is:

$$\mathcal{N} = \int_{\mathcal{V}} f(q,p,t)dqdp \tag{1.3}$$

where the limits of integration define $\mathcal{V}$. The rate of change with time of $\mathcal{N}$ is given by:

$$\frac{d\mathcal{N}}{dt} = \int_{\mathcal{V}} \frac{\partial f}{\partial t} dqdp \tag{1.4}$$

However, the rate of change of $\mathcal{N}$ is also the rate at which phase points *flow* through the volume $\mathcal{V}$. The rate of flow of the phase points is given by $f\vec{\mathcal{U}}$, where $\vec{\mathcal{U}}$ is the bulk fluid velocity in phase space,

$$\vec{\mathcal{U}} = (\dot{q}_1, \dot{q}_2, \ldots, \dot{q}_{3N}, \dot{p}_1, \dot{p}_2, \ldots, \dot{p}_{3N})$$

The rate of flow of phase points through the surface $\mathcal{S}$ enclosing $\mathcal{V}$ is $f\vec{\mathcal{U}} \cdot \hat{n} d\mathcal{S} \equiv f\vec{\mathcal{U}} \cdot d\vec{\mathcal{S}}$. Integrating over the surface:

$$\frac{d\mathcal{N}}{dt} = -\int_{\mathcal{S}} f\vec{\mathcal{U}} \cdot d\vec{\mathcal{S}} \tag{1.5}$$

where the negative sign implies $\frac{d\mathcal{N}}{dt} < 0$ for a flow of phase points out of $\mathcal{V}$. Transforming this surface integral to a volume integral by utilizing Gauss' divergence theorem,

$$\frac{d\mathcal{N}}{dt} = -\int_{\mathcal{V}} \nabla \cdot (f\vec{\mathcal{U}}) dqdp \tag{1.6}$$

Since $\mathcal{V}$ is an arbitrary volume in phase space, the integrands of equations 1.4 and 1.6 must be equal. By equating these expressions, a continuity equation for $f(q,p,t)$ results,

$$\frac{\partial f}{\partial t} + \nabla \cdot (f\vec{u}) = 0 \tag{1.7}$$

Equation 1.7 is a statement of the conservation of phase points in the dynamical phase space. This equation can be put in an alternate form familiar to those who study classical mechanics,

$$\frac{\partial f}{\partial t} + [H, f] = 0 \tag{1.8}$$

where H is the *Hamiltonian function* of the system, and $[H, f]$ denotes the *Poisson bracket*:

$$[H, f] = \sum_{j=1}^{3N} \left(\frac{\partial H}{\partial p_j} \frac{\partial f}{\partial q_j} - \frac{\partial H}{\partial q_j} \frac{\partial f}{\partial p_j} \right)$$

McQuarrie *(1976)* identifies 1.8 as the *Liouville equation* and regards it as the most fundamental equation in statistical mechanics. The *Liouville theorem* is the statement of the conservation of phase points in an arbitrary element in phase space. An explicit proof of Liouville's theorem follows directly from differentiation of $f(q, p, t)$ with respect to time:

$$\frac{df}{dt} = \frac{\partial f}{\partial t} + \sum_{j=1}^{3N} \left(\frac{\partial f}{\partial q_j} \frac{\partial q_j}{\partial t} + \frac{\partial f}{\partial p_j} \frac{\partial p_j}{\partial t} \right) \tag{1.9}$$

or, simplifying:

$$\begin{aligned} \frac{df}{dt} &= \frac{\partial f}{\partial t} + \sum_{j=1}^{3N} \left(\dot{q}_j \frac{\partial f}{\partial q_j} + \dot{p}_j \frac{\partial f}{\partial p_j} \right) \\ &= \frac{\partial f}{\partial t} + \sum_{j=1}^{3N} \left(\frac{\partial H}{\partial p_j} \frac{\partial f}{\partial q_j} - \frac{\partial H}{\partial q_j} \frac{\partial f}{\partial p_j} \right) \end{aligned}$$

$$= \frac{\partial f}{\partial t} + [H, f]$$
$$= 0$$

where use has been made of the canonical equations of motion,

$$\dot{q}_j = \frac{\partial H}{\partial p_j}$$
$$\dot{p}_j = -\frac{\partial H}{\partial q_j}$$

The last step in the above sequence of equations follows from 1.8. Since $\frac{df}{dt} = 0$, f must be a constant.

The most frequent form of the equation involving the conservation of $f(q, p, t)$ is known as the Boltzmann equation. The Boltzmann equation refers to the distribution function $f(\vec{x}, \vec{v}, t)$, involving velocity rather than momentum. The Boltzmann equation is merely a restatement of equation 1.7. Separating the spatial and velocity divergences,

$$\frac{\partial f}{\partial t} + \nabla \cdot (f\dot{\vec{x}}) + \nabla_v \cdot (f\dot{\vec{v}}) = 0 \tag{1.10}$$

where $\nabla_v = \left(\frac{\partial}{\partial v_x}\hat{e}_x + \frac{\partial}{\partial v_y}\hat{e}_y + \frac{\partial}{\partial v_z}\hat{e}_z\right)$ is the gradient operator in velocity space. Identifying $\dot{\vec{x}} = \vec{v}$ and $\dot{\vec{v}} = \vec{F}/m$, the above becomes:

$$\frac{\partial f}{\partial t} + \nabla \cdot (f\vec{v}) + \nabla_v \cdot (f\vec{F}/m) = 0$$

but this may be rewritten as,

$$\frac{\partial f}{\partial t} + \vec{v} \cdot \nabla f + \vec{F}/m \cdot \nabla_v f = 0 \tag{1.11}$$

Equation 1.11 is referred to as the *collisionless* Boltzmann equation; the effect of collisions between the particles has not been included in the above discussion. A collision term can be added to the right hand side of 1.11, however in the case of tenuous fluids (such as the solar wind) the collision term is safely neglected. If the force is strictly an electromagnetic force, the collisionless Boltzmann equation is sometimes referred to as the *Vlasov equation*. Equation 1.11 is the primary equation in the theory of the modulation of cosmic rays in the heliosphere.

The aforementioned fluid equations of continuum mechanics can be derived directly from the first three moments of the Boltzmann equation *(Siscoe, 1983; Chen, 1984)*. The zero-th order moment of 1.11 results in the continuity equation:

$$\frac{\partial \rho}{\partial t} + \nabla \cdot (\rho \vec{U}) = 0 \tag{1.12}$$

The first moment of 1.11 yields the momentum equation, sometimes referred to as the *Euler equation*:

$$\rho \left[\frac{\partial \vec{U}}{\partial t} + (\vec{U} \cdot \nabla)\vec{U} \right] = \rho_c \vec{F} - \nabla p \tag{1.13}$$

The second moment of 1.11 provides the energy transport equation:

$$\frac{\partial}{\partial t}\left[\frac{1}{2}\rho U^2 + I\right] + \nabla \cdot \left[\left(\frac{1}{2}\rho U^2 + I\right)\vec{U} + p\vec{U} + \vec{q}\right] = \vec{J} \cdot \vec{E} \tag{1.14}$$

In 1.12 to 1.14, $\vec{U}$ is the fluid bulk velocity, ρ is the mass density, ρ_c is the charge density, p is the pressure (taken as a scalar here), I is the internal energy, $\vec{q}$ is the heat flux vector, and $\vec{J}$ is the current density.

The solar wind is considered as the fluid in this model. However, it is recognized that the equations of magnetohydrodynamics constitute a physical model only. As pointed out by Burlaga *(1984)*, it has not been shown rigorously that continuum mechanics exactly describes the conditions of the heliosphere. Magnetohydrodynamics is simply adopted as the best theory to date, subject to revisions. Barnes *(1983)* implies that this model is not to be applied to small scales in the heliosphere; that is, on scales where the local ion and electron gyroradii and gyroperiods are not negligible. In fact, these time and spatial scales are much smaller in general than those describing the Coulomb collisions of the solar wind particles and therefore the solar wind is strictly a *collisionless plasma.* It is only because of the flow—field line coupling that the heliosphere can be described somewhat from within the framework of magnetohydrodynamics.

It was first Parker *(1958, 1965)* who considered in detail that the outer atmosphere of the Sun, the corona, was not static but was rather in a dynamical state. Earlier analysis regarding the peculiar nature of the tails of comets by Biermann led to the discovery of the *solar corpuscular radiation.* He had speculated that it was because of a pressure resulting from a corpuscular outflow radial from the Sun that comet tails were always observed in a direction radially opposed to the Sun.

Parker used the familiar equations of hydrodynamics to show that the solar corona must expand supersonically, and in a radial direction, into the solar system. Specifically, he employed the equation of hydrostatic equilibrium (Bernoulli's equation),

$$\nabla p = F_g \tag{1.15}$$

(where F_g is the gravitational force upon the fluid element) the continuity equation, 1.12, and the momentum equation, 1.13 to show that for a coronal temperature profile, $T(r)$, that falls less rapidly than $1/r$, the only steady state of the solar atmosphere is an expansion to supersonic velocities at large distances. The solar wind, then, is a highly conducting fluid (plasma) with a velocity which is generally radial from the sun.

The bulk properties of the solar wind can be summarized *(Gibson, 1973)*: the flow velocity varies from 400 to 700 kilometers per second, the hydrogen ion number density from 1 to 10 per cubic centimeter, and the temperature from 5×10^4 to 5×10^5 kelvin.

Barnes *(1983)* stresses the variability of the solar wind:

> *The solar wind does not flow quietly. It seethes and undulates, fluctuating on time scales that range from the solar rotation period down to fractions of milliseconds.*

The physics of plasma oscillations is a very rigorous topic and will be dealt with only in simplistic terms where needed in this thesis. The particular type of plasma wave of importance for the present purposes is the *Alfvén wave*. The Alfvén wave is an MHD wave whose propagation vector is parallel to the mean magnetic field. The restoring forces in such a plasma oscillation are the electrostatic forces which are generated as the constituent charged particles in the plasma are separated by the fluctuation. The Alfvén wave propagates along the mean magnetic field with a constant velocity of about 40 km/s *(Barnes, 1983)*. Most of the solar wind fluctuations are of MHD scale; that is, their time and spatial scales are much larger

than the local proton gyroperiod and gyroradius, respectively.

It is the very presence of the solar wind fluctuations, and their effect upon the local magnetic field, which makes possible the *magnetic scattering* of the high energy cosmic rays. This is the essence of this thesis. The entirety of modulation theory depends upon the scattering of cosmic rays in the solar wind.

1.1.2 The Frozen Field Condition

It is the close relationship between the solar wind and the solar magnetic field, combined with the fluctuations present in the the solar wind, which have the important dynamical effect upon the high energy cosmic rays. Any charged particle moving in the presence of an electromagnetic field is subject to the well known Lorentz force. In the case of a constant and uniform magnetic field the particle trajectory is well understood, the equation of motion is readily integrated. However, if fluctuations exist within the magnetic field the trajectory is drastically affected. These effects will be discussed in detail in a later section.

If the fluctuations in the solar wind plasma can somehow be transferred to the magnetic field through which it flows, it can be qualitatively understood how the motion of any heliospheric charged particles can be affected by processes which are related to the sun. It is the purpose of this section to prove that for an infinitely conducting plasma moving through an ambient magnetic field, there is a physical coupling between the flowing plasma and the conceptual magnetic lines of force.

The proof outlined here is that presented by Holt and Haskel *(1965)*. The essence of the proof involves the derivation of two equations; one involving the velocity of an element of the infinitely conducting plasma and one involving the

velocity of a magnetic line of force. It will be seen that the two equations are identical, thereby it can be concluded that the velocity of the flowing plasma must equal the velocity of the field line.

The generalized *Ohm's law* is, in cgs-Gaussian units:

$$\vec{J} = \sigma \left[\vec{E} + \frac{1}{c} \left(\vec{V}_p \times \vec{B} \right) \right] \tag{1.16}$$

where $\vec{J}$ is the current density $(= q_i \rho_i V_i + q_e \rho_e V_e)$, σ is the plasma conductivity, and $\vec{V}_p$ is the center of mass fluid flow velocity of a plasma element. For an ideal MHD case, it is assumed that the plasma conductivity is infinite. Obviously then, from 1.16, for a finite current density to exist,

$$\vec{E} + \frac{1}{c} \left(\vec{V}_p \times \vec{B} \right) = 0 \tag{1.17}$$

This can be combined with a Maxwell equation,

$$c \nabla \times \vec{E} = -\dot{\vec{B}}$$

to give,

$$\nabla \times \left(\vec{V}_p \times \vec{B} \right) = \dot{\vec{B}} \tag{1.18}$$

This is an equation involving the velocity of the plasma element through the magnetic field.

Another Maxwell equation,

$$\nabla \cdot \vec{B} = 0$$

can be combined with the vector identity,

$$\nabla \cdot \left(\nabla \times \vec{F}\right) = 0$$

where $\vec{F}$ is an arbitrary vector, to give:

$$\vec{B} = \nabla \times (\phi \nabla \psi) \tag{1.19}$$

That is, the magnetic field is represented by the curl of an arbitrary vector $\phi \nabla \psi$. Using the following identity (where f is an arbitrary scalar),

$$\nabla \times (f\vec{F}) = \nabla f \times \vec{F} + f \nabla \times \vec{F} \tag{1.20}$$

$\vec{B}$ can be represented as:

$$\begin{aligned} \vec{B} &= \nabla\phi \times \nabla\psi + \phi \nabla \times \nabla\psi \\ &= \nabla\phi \times \nabla\psi \end{aligned} \tag{1.21}$$

where the second term is zero since the curl of the gradient of a scalar function is zero. Geometrically, the above equation states that a line of magnetic force can be thought of as the intersection of two constant surfaces, $\phi(x, y, z, t)$ and $\psi(x, y, z, t)$.

Let the line of magnetic force be in motion with a velocity of $\vec{V}_B$. This is equivalent to letting the surfaces ϕ and ψ move with the same velocity. Taking the time derivative of these constant functions,

$$\frac{d\phi}{dt} = \frac{\partial \phi}{\partial t} + \vec{V}_B \cdot \nabla\phi = 0$$
$$\frac{d\psi}{dt} = \frac{\partial \psi}{\partial t} + \vec{V}_B \cdot \nabla\psi = 0$$

or,

$$-\dot{\phi} = \vec{V}_B \cdot \nabla\phi \tag{1.22}$$

$$-\dot{\psi} = \vec{V}_B \cdot \nabla\psi \tag{1.23}$$

Now forming the cross product $\vec{V}_B \times \vec{B}$ using 1.21,

$$\vec{V}_B \times \vec{B} = \vec{V}_B \times (\nabla\phi \times \nabla\psi)$$

where the right hand side is merely a triple vector product, therefore,

$$\vec{V}_B \times \vec{B} = \left(\vec{V}_B \cdot \nabla\psi\right) \nabla\phi - \nabla\psi \left(\vec{V}_B \cdot \nabla\phi\right) \tag{1.24}$$

Substituting equations 1.22 and 1.23 into 1.24,

$$\vec{V}_B \times \vec{B} = -\dot{\psi}\nabla\phi + \dot{\phi}\nabla\psi$$

Taking the curl of both sides of this equation,

$$\nabla \times \left(\vec{V}_B \times \vec{B}\right) = \nabla \times \left(\dot{\phi}\nabla\psi\right) + \nabla \times \left(-\dot{\psi}\nabla\phi\right) \tag{1.25}$$

Expanding the right hand side of this using 1.20,

$$\nabla \times \left(\vec{V}_B \times \vec{B}\right) = \dot{\phi}\left(\nabla \times \nabla\psi\right) + \nabla\dot{\phi} \times \nabla\psi - \dot{\psi}\left(\nabla \times \nabla\phi\right) - \nabla\dot{\psi} \times \nabla\phi$$

where the first and third terms on the right hand side vanish because again they are the curl of a gradient. The right hand side simplifies:

$$\nabla \times \left(\vec{V}_B \times \vec{B}\right) \;=\; \nabla\dot{\phi} \times \nabla\psi - \nabla\dot{\psi} \times \nabla\phi$$

$$
\begin{aligned}
&= \nabla\dot{\phi} \times \nabla\psi + \nabla\phi \times \nabla\dot{\psi} \\
&= \frac{\partial}{\partial t}(\nabla\phi \times \nabla\psi) \\
&= \frac{\partial \vec{B}}{\partial t} \qquad (1.26)
\end{aligned}
$$

Therefore it is seen that equations 1.18 and 1.26 are identical and it can be concluded that the velocity of the plasma element, $\vec{V}_p$, and that of the magnetic field line, $\vec{V}_B$, must be the same. It is then proved explicitly that there is a physical coupling between the flowing solar wind plasma and the magnetic field through which it flows.

Of course, an infinitely conducting plasma is only an idealization which cannot occur in reality, although for the conditions appropriate to the heliosphere it is a very good approximation. The quantity defining the efficiency of the plasma—field coupling is the *magnetic Reynolds number*, R_m:

$$R_m = \frac{4\pi}{c^2}\sigma V_p L \qquad (1.27)$$

where σ is the conductivity of the plasma which has a bulk fluid flow V_p, and L is the characteristic length of the magnetic field. For $R_m \gg 1$, the plasma—field coupling is very strong; that is, the fluid velocity and the magnetic field are *frozen* together. For $R_m \ll 1$, the coupling is very weak. In this case, the magnetic field is relatively unperturbed by the motion of the flowing plasma. Also note from equation 1.18 that if the plasma flow is either parallel or anti-parallel to the magnetic field, then the field is unaffected.

The magnetic Reynolds number is proportional to both the conductivity and flow velocity of the plasma. Since the conductivity is inversely proportional to

the rate of collisions of the plasma particles, it follows that for tenuous plasmas, such as the solar wind, the conductivity is very high and therefore $R_m \gg 1$. As a result of this, it is generally concluded that the solar wind and the interplanetary magnetic field are rigidly coupled in the heliosphere.

The energy densities of the mass flow of the solar wind plasma and the interplanetary magnetic field determine which is the dominant partner in the coupling process. The energy density of the solar wind mass flow is:

$$\epsilon_{sw} = \frac{1}{2}\rho V_p^2$$

and the energy density of the interplanetary magnetic field is:

$$\epsilon_{\vec{B}} = \frac{B^2}{8\pi}$$

It is easily seen that for typical conditions in the heliosphere that $\epsilon_{sw} \gg \epsilon_{\vec{B}}$, 4500 eV/cm^3 versus 60 eV/cm^3 *(Fisk, 1974)*. It is the mass flow of the solar wind plasma which dominates the coupling process.

It is seen then that the outward radial flow of the solar wind carries with it the otherwise idealized solar magnetic dipole field. To complicate this, the solar rotation has a peculiar effect upon the structure of the interplanetary magnetic field (IMF). The model of the IMF is based upon these two processes; the *frozen-in* magnetic field lines, and the solar rotation.

With an understanding of the basic physics involved, it is appropriate to next discuss the current idealized model of the the heliospheric IMF structure. The modulation of cosmic rays in the heliosphere must start with a thorough description of the interplanetary conditions.

1.1.3 The Model of the IMF

The basic model of the interplanetary magnetic field structure is the result of the early work of Parker, and it is often referred to as the *Parker Model.* The model IMF is a direct result of the processes described in the preceding section, namely the field—flow coupling, and the solar rotation. It is understood that the sun undergoes a differential rotation, a faster rotation rate exists at the solar equator than at the poles, but it is the overall rotation which is immediately important.

As a result of these two processes, the field lines are seen to follow a distinctive *Archimedean spiral* pattern as given by:

$$r = V_{sw}t + b$$

$$\phi = \phi_o + \Omega t \sin\theta$$

where r is the heliocentric radial distance, V_{sw} is the solar wind speed, ϕ is the longitudinal coordinate, ϕ_o is the longitude of the origin of the field line, Ω is the solar rotation rate, and θ is the co-latitude. The constant b is the radial distance at which the (spherically symmetric) coronal plasma outflow becomes supersonic.

The components of the Parker field in the heliocentric spherical coordinate system, $\vec{B} = (B_r, B_\theta, B_\phi)$, are *(Quenby, 1983a)*:

$$\begin{aligned} B_r &= B_o \left(\frac{b}{r}\right)^2 \\ B_\theta &= 0 \\ B_\phi &= B_o \left(\frac{b}{r}\right)^2 \frac{\Omega r}{V_{sw}} \sin\theta \end{aligned} \tag{1.28}$$

The angle that a model field line makes with the radial direction at some radial distance r is given by Ψ, the so-called *garden hose angle*, where

$$\begin{aligned} \tan\Psi &= \frac{B_\phi}{B_r} \\ &= \frac{\Omega r}{V_{sw}} \sin\theta \end{aligned} \tag{1.29}$$

Extensions to Parker's original model have included the possibility that the solar dipole field axis does not exactly coincide with the solar rotation axis. For an angle ν separating these axes, the magnetic field is described by *(Quenby, 1983a)*:

$$\vec{B} = B_o \left(\frac{b}{r}\right)^2 \left[\hat{e}_r - \frac{\Omega r}{V_{sw}} \sin\theta\right] \left\{1 - 2H\left[\theta - \left(\frac{\pi}{2} + \nu \sin\left(\phi - \frac{\Omega r}{V_{sw}}\right)\right)\right]\right\}$$

where $H(x)$ is the Heaviside step function,

$$H(x) = \begin{cases} 0 & x < 0 \\ 1 & x > 0 \end{cases}$$

It can be seen in the above expression for $\vec{B}$ that the magnetic field changes sign at a certain boundary mathematically described by the term which is the argument of the Heaviside step function. The boundary which separates the inward and outward direction of the magnetic field is known as the *current sheet*. The current sheet is given by:

$$\theta_{cs} = \frac{\pi}{2} + \nu \sin\left(\phi - \frac{\Omega r}{V_{sw}}\right) \tag{1.30}$$

Figure 1.1 is a diagram of the heliospheric current sheet as given by equation 1.30. The polarity of the IMF is opposite on the two sides of the current

Heliospheric Current Sheet

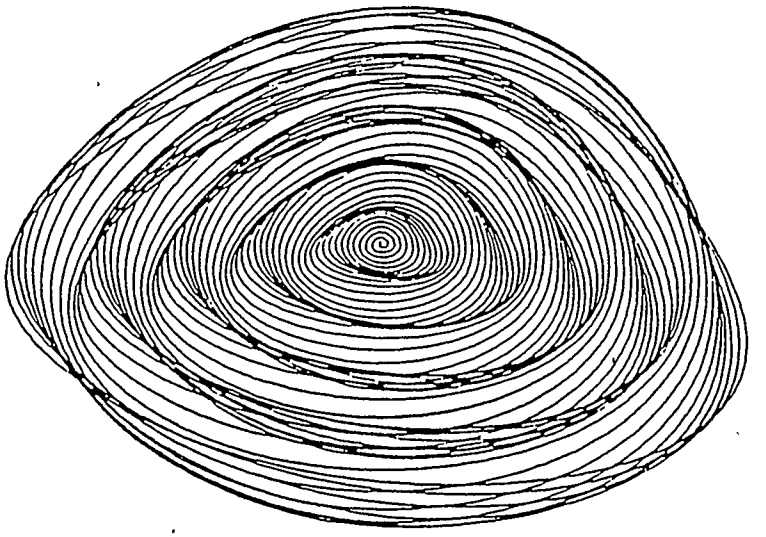

Figure 1.1: The Heliospheric Current Sheet
As given by equation 1.30, the current sheet represents the boundary between opposite polarities of the interplanetary magnetic field. Here ν is taken to be 7.5°, the solar wind speed is 400 km/s, and the solar rotation rate is 1/27 days. The diameter of the above diagram is 60 A.U.

sheet. It will be seen in chapter three how this *sector structure* appears in the Voyager magnetic field data.

It is convenient to now define a coordinate system that is used in a later chapter to describe the IMF as observed by Voyager 2. It is a heliocentric rectangular cartesian system defined by the three unit vectors $(\hat{e}_r, \hat{e}_t, \hat{e}_n)$. This system is known as the *Radial-Tangential-Normal* (RTN) coordinate system. The vector $\hat{e}_r$ is in the positive radial direction, the vector $\hat{e}_t$ is measured 90° counterclockwise to $\hat{e}_r$, and $\hat{e}_n$ completes the right-handed orthogonal triad. In these coordinates, the IMF is described by three coordinates:

$$\vec{B} = (B_r, B_t, B_n)$$

Alternatively, the IMF vector can be expressed as a magnitude and two angles:

$$\vec{B} = \left(|\vec{B}|, \lambda_B, \delta_B\right) \tag{1.31}$$

where λ_B is the angle measured counterclockwise from the radial direction which describes the projection of $\vec{B}$ onto the R-T plane, and δ_B is the elevation angle of $\vec{B}$ from the R-T plane:

$$\lambda_B = \tan^{-1}\left(\frac{B_t}{B_r}\right)$$
$$\delta_B = \sin^{-1}\left(\frac{B_n}{|\vec{B}|}\right)$$
$$|\vec{B}| = \sqrt{B_r^2 + B_t^2 + B_n^2}$$

It is very easy to see the occurrence of a sector boundary change in the angle λ_B. At larger radial distances, the azimuthal component of the Parker field, B_ϕ, becomes increasingly larger. As a result, the value of λ_B at larger radial distances is generally near either 90° or 270° depending on which sector the detector is in. The detection of a sector boundary is then very evident in the value of λ_B, it changes almost immediately from one general average value to the other (in the resolution of the data to be presented).

1.2 Charged Particles in the Heliosphere

The study of cosmic rays is a relatively young science. It was only slightly after the turn of the century that, through a series of balloon experiments, V. F. Hess

was able to undoubtedly conclude that the origin of the then mysterious ionizing radiation was in fact extra-atmospheric. Subsequent balloon flights verified these observations; at a height of nine kilometers above the surface of the earth the ionization rate was found to be more than ten times its surface value.

The history of the study of cosmic rays can be broadly divided into four major periods *(Dorman, 1974)*. The first period, 1926–1934, began just after the identification of the source of the *secondary component*, those particles created via collisions of the original extra-atmospheric *primary* cosmic rays with the constituents of the upper atmosphere. During this period, the variation in the intensity of cosmic rays was discovered, and the search for the origin of this variability began.

The second period, 1935–1950, saw the continuous recording and systematic study of the penetrating secondary μ-meson component. The appearance of the principal problems of the variations of the intensity of the primary cosmic rays also surfaced during this time. It was realized that a thorough study of the time variations of cosmic rays would yield pertinent information regarding the sun and interplanetary medium.

The third period, 1951–1956, involved the recording of other secondary components as well as the development of the theory of the meteorological effects of secondaries. It was at this time that the energy spectra of the primary cosmic rays was first studied and the nature of their origin was first speculated.

The fourth period extends from 1957, when the first satellite recording the extra-atmospheric spectra was launched, to the present. Of course, not included by Dorman was the advent of the spacecraft era which provided data from the farther reaches of the heliosphere. Spacecraft data such as that provided by the

Pioneer and Voyager programs have evolved the cosmic ray time variation studies into time and spatial studies.

1.2.1 Cosmic Rays

Cosmic rays are highly energetic charged particles which are observed in the interplanetary medium. Their energies are much larger than the energy of the solar wind particles (which is typically less than 50 eV for electrons and 10 eV for protons). The energy range of observed cosmic ray particles is enormous, extending over fourteen orders of magnitude from 10^6 eV to 10^{20} eV.

The charged particles are merely the atomic nuclei of common elements. The distribution of these incident nuclei corresponds approximately to that found in the accessible galaxy. Protons account for $\sim$ 90% and alpha particles (helium nuclei) $\sim$ 10% of the cosmic ray constituents, with ions of heavier elements constituting the remaining $\sim$ 1%. Table 1.1 *(Pomerantz, 1971)* lists the composition of the primary cosmic radiation.

It is generally recognized that there are two varieties of cosmic rays; those which have a definite solar origin, called solar cosmic rays, and those which presumably have an extra-heliospheric origin, called galactic cosmic rays. While the origin of solar cosmic rays is generally accepted to be from events such as solar flares, the origin of galactic cosmic rays is not so obvious.

In view of the previous subsection regarding the structure of the IMF, it follows that if galactic cosmic rays are in fact of *non-local* origin they will have to perform work to flow into the heliosphere against the outflow of the solar wind and the coupled magnetic field irregularities. If this is the case, the cosmic ray

Element	Atomic Number	Cosmic Ray Abundance (%)	Cosmic Abundance (%)
H	1	93.0	91.0
He	2	6.3	9.1
Li, Be, B	3,4,5	0.1	10^{-7}
C,N,O,F	6,7,8,9,	0.4	0.1
Ne-K	10-19	0.1	0.01
Ca-Zn	20-30	0.04	10^{-3}
Ga-U	31-92	10^{-6}	10^{-6}
>U	>92	?	?

Table 1.1: The Composition of Primary Cosmic Radiation
The distribution of cosmic ray particles is very nearly equal to that of the corresponding nuclei found in the accessible galaxy. The gap in the data for very heavy nuclei demonstrates the relative rarity of these particles.

intensity should increase with increasing radial distance from the sun. Attempts to quantitatively measure this using spacecraft data have made use of the cosmic ray radial gradient:

$$G_r = \frac{\ln\left(\frac{R_1}{R_2}\right)}{\Delta r}$$

where R_1 and R_2 are count rates of two detectors and $\Delta r = (r_1 - r_2)$ is the radial separation of the two detectors. In general, there are two types of radial gradients defined. The first, the *integral* radial gradient, refers to data from a detector at $\sim$ 1 A.U. and another detector at large radial distances. The second, the *differential* radial gradient, refers to data from two detectors which are at radial distances greater than 1 astronomical unit.

Best estimates of the differential radial gradients are calculated with the Voyager 1 and Voyager 2 data and the Pioneer 10 and Pioneer 11 data *(Van Allen and*

Randall, 1985; Venkatesan et al., 1984; Venkatesan et al., 1985). These studies indicate the presence of a positive radial gradient with an approximate average value of 2 to 4%/A.U. This indicates the spacecraft at a larger radial distance is detecting a larger cosmic rate count rate. This would seem to be consistent with a non-local origin theory—the cosmic radiation appears to be of extra-heliospheric origin.

Furthermore, these same studies indicate that the differential radial gradient is decreasing at an approximately constant rate of 0.4%/A.U./year. If the heliosphere possessed a static boundary this would suggest that the spacecraft are approaching the boundary of the cosmic ray modulation. (A radial gradient of zero implies both spacecraft have equal count rates.) In fact, the size of the heliosphere is thought to oscillate in synchronization with the solar cycle. Irrespective of this fact it appears that the modulation size is of finite extent and the spacecraft may soon detect the modulation boundary, outside of which the cosmic ray intensity may be constant and isotropic.

It has been noted though, that proponents of the local origin theory of cosmic rays still exist. Alfvén is a primary example. It is still his contention that there is a mechanism within the solar system which is responsible for accelerating particles to hundreds of MeV, perhaps even to the GeV range *(Krimigis and Venkatesan, 1988).* It has been noted also that the majority of cosmic ray detection has been limited to the helioequatorial plane, with the exception of Voyager 1 since the 1980 Saturn encounter, and that perhaps the definitive origin theory must wait until further out-of-the-ecliptic data is available.

1.2.2 Cosmic Ray Modulation Theory

The attempt to describe the bulk cosmic ray behavior under prevailing circumstances in the heliosphere is referred to as *modulation theory*. The cosmic rays are modulated by the current conditions in the interplanetary medium. Modulation theory was developed soon after the model of the IMF was refined. In fact, Quenby *(1983a)* indicates that the relevant effects governing the modulation of cosmic rays were identified by 1965, although the relative importance of the various effects were still to be decided. The purpose of this section is to introduce the modulation theory. The remaining chapters do not explicitly refer to the solar modulation effects but the acceleration of charged particles by shocks in the heliosphere is very much a related topic. Many excellent review articles exist that consider in detail the topic of modulation theory *(Jokipii, 1971; Fisk, 1974; Gleeson and Webb, 1980; Quenby, 1983a; Quenby, 1983b)*.

To briefly summarize the previous sections, it can be said that the solar wind is a collisionless plasma which flows supersonically and radially from the sun. It drags with it the passive solar magnetic field, complete with any irregularities, or *scattering centers*, that may be present within. The effect of the solar rotation is to produce a large-scale Archimedean spiral mean field. The result upon the charged cosmic rays is evident.

The charged cosmic rays attempt to helix along the mean field lines but are scattered by the magnetic irregularities present. The outflow of the solar wind serves to convect radially outward these scattering centres. Thus there is a convection outwards of galactic cosmic rays which are trying to stream into the inner

heliosphere. In the case of solar cosmic rays, the scattering centers in the magnetic field impede the outflow of the solar particles *(Fisk, 1983a)*.

The motion of cosmic rays in the interplanetary medium is sometimes regarded as a diffusive process. The charged particles interact elastically with the magnetic irregularities at random intervals such that the motion of the particles becomes, in the limit, diffusive. In general then, there must be a component of the diffusion perpendicular to the mean field. In fact, there is no clear evidence that the particles diffuse as they encounter the scattering centers. A diffusive approximation is merely a mathematical model which yields results that compare favorably with observations.

Let $u(\vec{r}, T, t)$ be the cosmic ray number density per unit interval of kinetic energy T at some radial distance r. Let $\vec{S}$ be the differential current density, or *streaming*, the number of particles in a particular energy interval which cross a unit area normal to the streaming. The equation of continuity of the number of particles is then, in the fixed frame of reference *(Fisk, 1983b; Quenby, 1983a)*:

$$\frac{\partial u}{\partial t} + \nabla \cdot \vec{S} + \frac{\partial}{\partial T}\left(\vec{V}_{sw} \cdot \nabla P\right) = 0 \tag{1.32}$$

where $\vec{V}_{sw}$ is the velocity of the solar wind. The third term above represents the work done upon the cosmic ray pressure gradient by the solar wind. The isotropic particle pressure is given by *(Fisk, 1983b)*:

$$P = \frac{\alpha^* T u}{3} \tag{1.33}$$

with

$$\alpha^* = \frac{(T + 2T_\circ)}{(T + T_\circ)}$$

where $T_\circ$ is the particle rest energy. The streaming as measured in the fixed frame is given by the sum of two processes:

$$\vec{S} = C\vec{V}_{sw}u - \kappa \cdot \nabla u \tag{1.34}$$

The first term of equation 1.34 is derived from a Taylor expansion of the statement of Liouville's theorem, that the particle distributions are the same in two different coordinate systems. The transformation is then made between the particle distribution function to differential number density in kinetic energy *(Gleeson and Webb, 1980, Appendix B)*. The term $C = 1 - \frac{1}{3u}\frac{\partial(\alpha^* T u)}{\partial T}$ is the *Compton-Getting coefficient*, which takes into account the artificial anisotropies as observed in the fixed frame which are a result of the relative motion between the fixed (observation) reference frame and the solar wind frame. This effect is discussed in detail in chapter 5. The second term is the diffusive streaming term, where κ is a diffusion tensor.

Substituting equations 1.33 and 1.34 into the conservation equation 1.32, results in a *Fokker-Planck* equation for u,

$$\frac{\partial u}{\partial t} = \nabla \cdot (\kappa \cdot \nabla u) - \nabla \cdot \left(\vec{V}_{sw}u\right) + \frac{1}{3}\left(\nabla \cdot \vec{V}_{sw}\right)\frac{\partial}{\partial T}\left(\alpha^* T u\right) \tag{1.35}$$

Equation 1.35 is the basic equation regarding the modulation of cosmic rays in the heliosphere. This equation is often expressed in a spherical polar coordinate system with the assumption of spherical symmetry *(Quenby, 1983a)*:

$$\frac{\partial u}{\partial t} = \frac{1}{r^2}\frac{\partial}{\partial r}\left(r^2 \kappa_{rr}\frac{\partial u}{\partial r} - r^2 V_{sw} u\right) + \frac{1}{3r^2}\frac{\partial}{\partial r}\left(r^2 V_{sw}\right)\frac{\partial}{\partial T}\left(\alpha^* T u\right) \tag{1.36}$$

where κ_{rr} is the radial diffusion coefficient given by,

$$\kappa_{rr} = \kappa_{\parallel}\cos^2\Psi + \kappa_{\perp}\sin^2\Psi$$

where $\kappa_{\parallel}$ and $\kappa_{\perp}$ are diffusion coefficients parallel and perpendicular to the mean magnetic field, and Ψ is the garden-hose angle.

It is instructive to discuss the physical interpretation of the terms in equation 1.36. The first term on the right hand side describes the diffusive effects, and the second is due to the convection outwards of the scattering centers. The third term represents the change in $u(\vec{r}, T, t)$ due to energy changes. It describes the adiabatic deceleration of the charged particles as a result of the diverging solar wind geometry. (The term $\frac{1}{r^2}\frac{\partial}{\partial r}\left(r^2 V_{sw}\right)$ is the rate at which a volume element expands as it moves radially out in the solar wind.) It is exactly these terms which have been known for over 25 years, but have been subject to constant refinement.

It should be noted that sometimes an additional term is included in the Fokker-Planck equation that accounts for *statistical acceleration (Fisk, 1983c)*. Statistical acceleration is a result of the scattering of the charged particles with magnetic field irregularities which move relative to the solar wind. This is essentially a first-order Fermi acceleration process; that is, a particle will gain (lose) energy when it is magnetically trapped between two convergent (divergent) scattering centers. The mechanical analogy of a first-order Fermi process is an object undergoing elastic collisions with two surfaces with a relative radial velocity with respect to one another.

Equation 1.36 can only be solved analytically after some simplifying assumptions have been made *(Jokipii, 1971; Fisk, 1971; Fisk, 1974)*. Among the various assumptions employed is the aforementioned spherical symmetry assumption, after which the Fokker-Planck can be expressed as above, as a function of only one spatial coordinate. Other assumptions are discussed in the review papers. Numerical solutions are often an alternative to the assumption technique. More freedom is incorporated into techniques which involve numerical solutions, however numerical techniques are at best approximate and often simplifying assumptions are still required *(Fisk, 1971)*.

Even though the modulation theory of cosmic rays was discussed in terms of a diffusive process, and even though no clear evidence exists to suggest that this should be an appropriate assumption, the results provided by the Fokker-Planck equation compare quite reasonably with observations. Because of this, equation 1.35 is likely to remain as the primary equation regarding the modulation of cosmic rays in the heliosphere.

1.2.3 The Time and Spatial Variations of Cosmic Ray Modulation

This chapter has reviewed the pertinent heliospheric physics required in a discussion of the factors which influence the behavior of charged particles in the interplanetary medium. It has been seen how processes involving the sun, namely the solar wind, the solar magnetic field and the solar differential rotation significantly affect the presence of charged particles.

It is intuitive then that any major periodicities or variations in these factors will be indicated in the observed cosmic ray data. Indeed this is the case. There

are several large-scale intensity variations observed in the data which are easily explainable within the context of solar wind variations.

On the grandest scale, there is the eleven year period of the solar cycle, as often characterized by the periodicity in the number of sunspots observed. The current model of this solar cycle is referred to as the *Babcock-Leighton* model. In essence, this model is successful in explaining many of the observed features of the solar cycle—the migration of the sunspots to the solar equator (as indicated by the *Maunder diagram*), the opposite polarity of the sunspot pairs, and reversals in the surface magnetic field.

The effect upon the incident cosmic rays is extraordinary. At the solar maximum the intensities of the high-energy particles are at a minimum, and at the solar minimum the intensities are greatest. This is a direct result of the outward convection of the magnetic irregularities which tends to deflect any charged particles away from the inner heliosphere. Intensity profiles for the current solar cycle are provided in Murtha, *(1986)*. Within are cosmic ray intensities as recorded by Pioneer 10 and 11, Voyager 1 and 2, IMP-8 (an earth-bound satellite), as well as two neutron monitors, Deep River and Alert. All available data indicate the last solar maximum (cosmic ray minimum) occurred in late 1980 and early 1981. The data were averaged over 27 days to avoid any higher frequency variations.

The next most predominant variation evident in the cosmic ray intensities is due to the 27 day synodic rotation period of the sun. Any long-lived center of activity (e.g. a coronal hole) upon the sun will result in a high speed solar wind stream which will have immediate effects upon the modulation of cosmic rays. A primary example of this type of effect will be discussed in detail in chapter

3; corotating interaction regions bounded by a forward-reverse shock pair have a distinct signature in the particle and magnetic field data.

There is also a small-amplitude diurnal variation recognized as the result of the earth's rotation. There is expected to be a maximum particle intensity at approximately 1800 hours local time. At this time the locality of the observer is approximately 90° east of the sun-earth line where the mean magnetic field, or arms of the Archimedean spiral, pummel it directly. The amplitude of the diurnal variation is only about 0.4% *(Pomerantz, 1971)*.

Superimposed upon these periodic effects are numerous transient effects. Most common are perturbations in the IMF as a result of solar flares. Solar flares are active regions upon the surface of the sun which are frequently associated with sunspots, and are generally predominant at solar maximum. An observed phenomenon related to flares and streams is a Forbush decrease. This is characterized by a sudden decrease in the particle data ($\sim$ hours) followed by a slow recovery to pre-interruption levels ($\sim$ days).

1.3 Objectives of the Thesis

With a basic introduction to the physical description of the heliosphere reviewed in this first chapter, the objectives of the remainder of this thesis can now be presented. As the title suggests, the effect upon the heliospheric low energy charged particles by interplanetary shock waves is to be investigated. Particle, magnetic field, and solar wind plasma data from the Voyager spacecraft, particularly those of Voyager 2, are presented during a time period in which several recurrences of two

candidate corotating shock pairs are observed. The modulation of the local low energy charged particle population in the immediate vicinity of these shock waves is observed, and the observations are compared to those theoretically expected.

Chapter two introduces the phenemenon of a magnetohydrodynamic shock wave. The important mathematical description of the relationship of the upstream field and plasma quantities and those downstream is discussed, as well as the importance of the *shock geometry* upon the acceleration of the charged particles. The two main acceleration mechanisms thought to be dominant, the *shock drift* and *Fermi* acceleration processes, are presented and the relationship between their efficiency and the shock geometry is explained.

The intent of chapter three is to introduce the primary data interval of concern. The Voyager 2 field and plasma data are presented over the time period of 79/080/00 to 79/180/23 and the hypothesis that there are observed three recurrences of two corotating shock pairs is first suggested. Evidence supporting that the observed features are in fact associated with corotating shocks is presented. Finally, the shock geometry, as given by the single parameter θ_{Bn} (the acute angle between the upstream mean magnetic field vector and the upstream vector normal to the shock plane) for the anticipated shocks is calculated.

Chapter four investigates the low energy charged particle intensity enhancements associated with the passage of the anticipated shock waves. The evolution of the particle differential energy spectrum over the entire data interval is presented and discussed in terms of particle acceleration at the shock fronts.

The angular distributions as recorded by the Low Energy Charged Particle experiment aboard Voyager 2 during a selected time interval within the primary

data interval are presented in chapter five. The techniques used in the transforming of the data from the spacecraft, or observation, frame to the pertinent co-moving, or solar wind plasma frame are discussed in detail. In addition to the observed data, also presented in chapter five are the results of a numerical simulation which attempts to model the acceleration processes considered important in the particular event for which the observed data is presented. The fundamentals of the simulation are discussed, particularly the choice of the model's input parameters as based upon the observed data (where available). The angular distributions of both the real and simulated data are presented in the form of pitch angle distributions and anisotropy plots. The up and downstream particle anisotropies are discussed in view of the current theories.

Chapter 2

SHOCK WAVES IN THE HELIOSPHERE

2.1 Shock Waves

The fluid dynamics of a plasma, such as the solar wind, are generally described by the macroscopic equations discussed in chapter one, subsection 1.2.1. In the case of magnetohydrodynamics, it was seen that it was necessary to include Maxwell's equations in the description. It will be discussed in this chapter how *shock waves* within this plasma fluid are described in general, and how certain idealistic approximations make the description much easier.

Small plasma oscillations are often treated under the assumption that the amplitudes of the oscillating quantities (the bulk flow velocity, particle number density, and electric field) are very small. Under this assumption, physically interesting and important plasma phenomena can be derived. Mathematically, this assumption is employed via the *linearization* of the macroscopic fluid equations, specifically the Euler and the continuity equations, and Poisson's equation.

The process of linearization involves assuming the oscillating quantity, say $\vec{U}$, varies only slightly from its equilibrium value, $\vec{U}_\circ$, by a perturbation amount $\vec{U}_1$ *(Chen, 1984)*. In this manner, the oscillating quantities are given by:

$$\vec{U} = \vec{U}_\circ + \vec{U}_1 \tag{2.1}$$

$$\rho_n = \rho_{no} + \rho_{n1} \tag{2.2}$$

$$\vec{E} = \vec{E}_o + \vec{E}_1 \tag{2.3}$$

These equations are then substituted into the continuity, Euler, and Poisson equations describing an initially uniform and neutral plasma. At this point, terms higher than first order in the variables are neglected. This is a result of the assumption of small amplitudes; terms quadratic (and higher) in the variables are assumed negligibly small. This technique results in the well known equations for the *plasma frequency*, ω_p, and the *ion acoustic speed* in the plasma, v_s (in cgs Gaussian units):

$$\omega_p = \left(\frac{4\pi\rho_{no}e^2}{m}\right)^{\frac{1}{2}} \tag{2.4}$$

$$v_s = \left(\frac{k_b T_e}{M}\right)^{\frac{1}{2}} \tag{2.5}$$

where e is the electronic charge, m is the electronic mass, k_b is the Boltzmann constant, T_e is the electron temperature (the ion temperature was assumed to be zero in equation 2.5), and M is the mass of the ions.

However, it must be remembered that 2.4 and 2.5 are the result of linear effects alone. For larger amplitudes the higher order terms are not negligible and must be considered in any such derivations. Shock waves are one result of the inclusion of nonlinear terms in the description of plasma waves.

The effect of considering nonlinear terms results in a wave whose pressure, density, velocity and temperature gradients increase across the wavefront as the wave propagates *(Chen, 1984; Boyd and Sanderson, 1969)*. These gradients can increase to the point where dissipative effects such as viscosity and heat conduction

become important. Boyd and Sanderson *(1969)* thus define a shock wave as *the steady profile produced by the balance of nonlinear and dissipative effects.*

The generally complicated physics involved in the complete description of the effects of a shock wave can be simplified by two assumptions: It can be assumed that the shock front is planar and infinitesimal in thickness, and that it has a propagation velocity parallel to a vector which is normal to the plane. (More generally, the shock front can be spherical, but in this case the plane is taken as the tangent plane to the point where a charged particle crosses the shock front.) In this representation internal effects are ignored and the shock front is considered as merely a discontinuity in the upstream and downstream plasma properties.

The dynamics of any charged particle in the neighborhood of the shock front is governed by the macroscopic fields on either side of the shock, and the shock is taken as the plane at which the fields upstream differ from those downstream. This is easily justified by noting that a particle's gyroradius in the heliosphere is generally much larger than the extent of the thickness of a shock, and so the particle is not affected significantly by the internal structure of the shock. A set of equations can be derived which relate the upstream and downstream fluid properties, and thus a particle's trajectory can be computed across a shock front.

2.2 Magnetic Rankine-Hugoniot Equations

Regarding the shock as a simple discontinuity in the fluid properties, separating the uniform and static upstream and downstream fields, a set of equations have been recognized which relate the macroscopic plasma properties on either side of

the shock. This set of equations is referred to as the magnetic Rankine-Hugoniot equations.

It can be shown that the magnetic Rankine-Hugoniot equations originate from the macroscopic plasma fluid equations of chapter one and the Maxwell equations. Specifically, the conservation form of the fluid equations *(Boyd and Sanderson, 1969)*, the divergence of the magnetic field, and the curl of the electric field are integrated across the shock front. If $\hat{n}$ is the unit vector in the direction of the shock's velocity (coincident with the shock unit normal), then the Rankine-Hugoniot equations in the reference frame moving with the shock are given by, in Gaussian cgs units *(Boyd and Sanderson, 1969)*:

$$\left[\rho\vec{U}\cdot\hat{n}\right]_1^2 = 0 \tag{2.6}$$

$$\left[\rho\vec{U}\left(\vec{U}\cdot\hat{n}\right) + \left(p + B^2/8\pi\right)\hat{n} - \left(\vec{B}\cdot\hat{n}\right)\vec{B}/4\pi\right]_1^2 = 0 \tag{2.7}$$

$$\left[\vec{U}\cdot\hat{n}\left\{\left(\rho I + \frac{1}{2}\rho U^2 + B^2/8\pi\right) + \left(p + B^2/8\pi\right)\right\} - \left(\vec{B}\cdot\hat{n}\right)\left(\vec{B}\cdot\vec{U}\right)/4\pi\right]_1^2 = 0 \tag{2.8}$$

$$\left[\vec{B}\cdot\hat{n}\right]_1^2 = 0 \tag{2.9}$$

$$\left[\hat{n}\times\left(\vec{U}\times\vec{B}\right)\right]_1^2 = 0 \tag{2.10}$$

where $[Y]_1^2 \equiv Y_2 - Y_1$ is a difference operator. In this co-moving reference frame

$\vec{U}$ is the plasma flow into (upstream, subscript '1') or out of (downstream, subscript '2') the shock front.

Equation 2.6 is a statement about the conservation of mass flow through the shock, 2.7 is the conservation of fluid momentum through the shock, and 2.8 is the conservation of flow energy through the shock. Equations 2.9 and 2.10 relate the static and uniform upstream and downstream magnetic fields. In the event of fluctuating field quantities, the magnetic field values referred to in the magnetic Rankine-Hugoniot equations can be taken as the mean fields *(Decker, 1988)*. Given the upstream plasma parameters, the corresponding downstream quantities are easily found using equations 2.6 – 2.10.

A careful inspection of these equations reveals the importance of the $\left(\vec{B} \cdot \hat{n}\right)$ term. The angle between the mean upstream magnetic field and the upstream shock unit normal is referred to as the *shock angle*, θ_{Bn}, where

$$\theta_{Bn} = \cos^{-1}\left(\frac{\vec{B}_1 \cdot \hat{n}}{|\vec{B}_1|}\right)$$

It will be discussed in a later section that the efficiency of the acceleration of charged particles at interplanetary travelling shocks is quite sensitive to the value of θ_{Bn}. Shocks are broadly classified into two categories depending upon the value of θ_{Bn}. Shocks with $\theta_{Bn} < 45°$ are termed *quasi-parallel* shocks since the mean upstream field is approximately parallel (or antiparallel, depending upon which sector the shock is observed in) to the shock normal, and conversely shocks with $\theta_{Bn} > 45°$ are termed *quasi-perpendicular* shocks.

It is instructive to discuss in detail the various methods of determining the shock normal from the available satellite or spacecraft data.

2.3 The Shock Normal

Because of the sensitive relationship between the value of θ_{Bn} and the efficiency of the particle acceleration process, much work has been devoted in developing accurate methods which measure this angle. A value of θ_{Bn} cannot be directly measured; instead it must be inferred from the observed plasma and magnetic field discontinuities which are a result of the shock.

The particular method employed in the determination of θ_{Bn} depends entirely upon the availability of certain data as well as the integrity of the available data. Methods have been developed for single or multiple spacecraft observations, for accurate plasma data, for accurate magnetic field data, or any combination of the above conditions. In the absence of plasma data it is assumed magnetic field data are available, and vice versa. However, the combination of both accurate plasma and field data is highly preferable. Generally, more elegant and accurate means of determining the shock geometry require a more full data set. It is instructive to review briefly some of these methods before describing how the shock normal angle was calculated for the present data set.

The simplest shock normal method requires no data and is to simply assume that the shock propagates approximately along its normal which is pointed approximately in the positive radial direction. For a constant solar wind speed then, the shock angle is a function only of the radial distance from the sun (based upon the Parker model of the interplanetary magnetic field). Chao and Chen *(1985)* have used this type of assumption in a study which calculates the distribution of θ_{Bn} in the solar wind. This distribution is calculated based upon the distributions of

the upstream magnetic field vector and the angle between the shock normal and the radial direction. Each component of the upstream magnetic field is assumed to follow a Gaussian distribution about some mean value. The average value of the angle between the shock normal and the radial direction was taken to be zero but with a large variance, up to 45° at a radial distance of 5 A.U. This is too large an uncertainty for practical purposes.

The next simplest method is via the *velocity coplanarity* method. This method assumes the up and downstream solar wind velocity vectors are coplanar and in a plane perpendicular to the shock plane. When the magnetic field is small *(Abraham-Shrauner, 1972)* the components of $\vec{U}_2$ and $\vec{U}_1$ parallel to the shock are equal and the difference $\left(\vec{U}_2 - \vec{U}_1\right)$ is in the approximate direction of the shock normal:

$$\hat{n} \approx \frac{\vec{U}_2 - \vec{U}_1}{\mid \vec{U}_2 - \vec{U}_1 \mid} \tag{2.11}$$

A method similar to the velocity coplanarity method is the *magnetic coplanarity* method. This method assumes that the up and downstream magnetic field vectors are coplanar in a plane perpendicular to the shock front, the *normal* plane. It can be shown *(Kessel, 1986)* from the Rankine-Hugoniot conditions that $\vec{B}_2$ and $\vec{B}_1$ are indeed coplanar. The Rankine-Hugoniot condition 2.9 states that the normal component of the magnetic field is conserved through the shock front and so the difference $\Delta\vec{B} = \vec{B}_2 - \vec{B}_1$ lies in the intersection of the normal plane and the shock plane (see Figure 2.1). The cross product of $\vec{B}_1$ into $\vec{B}_2$ is entirely in the shock plane and the cross product of this vector with $\Delta\vec{B}$ should be in the normal direction. Thus θ_{Bn} is found from:

$$\hat{n} = \frac{\left(\vec{B}_1 \times \vec{B}_2\right) \times \Delta\vec{B}}{\mid \left(\vec{B}_1 \times \vec{B}_2\right) \times \Delta\vec{B} \mid} \tag{2.12}$$

It is noted that for a small angle between $\vec{B}_1$ and $\vec{B}_2$, a large error is present in $\left(\vec{B}_1 \times \vec{B}_2\right)$ when large fluctuations are present in the field data. Note that equation 2.12 is singular for exactly perpendicular shocks.

More preferable methods of determining the geometry of a shock are by the so-called *mixed data* methods. This refers to cases where both plasma and field data are available and reliable. A version of an equation yielding $\hat{n}$ by this method is given by *(Abraham-Shrauner, 1972)*:

$$\hat{n} = \frac{\left[\left(\vec{U}_2 - \vec{U}_1\right) \times \vec{B}_1\right] \times \left(\left(\frac{\rho_2}{\rho_1}\right)\vec{U}_2 - \vec{U}_1\right)}{\mid \left[\left(\vec{U}_2 - \vec{U}_1\right) \times \vec{B}_1\right] \times \left(\left(\frac{\rho_2}{\rho_1}\right)\vec{U}_2 - \vec{U}_1\right) \mid} \tag{2.13}$$

where ρ_2 and ρ_1 are the upstream and downstream plasma mass densities. This method assumes $\left(\vec{U}_2 - \vec{U}_1\right)$ and $\vec{B}_1$ are coplanar and lie within the normal plane. This method is generally more accurate than the magnetic coplanarity method because the angle between $\left(\vec{U}_2 - \vec{U}_1\right)$ and $\vec{B}_1$ is usually larger than that between $\vec{B}_1$ and $\vec{B}_2$, and is therefore less sensitive to field fluctuations. Abraham-Shrauner and Yun *(1976)* provide other equations for $\hat{n}$ which are merely alternate versions of equation 2.13.

A least squares method of determining the best-estimate of the values of $\vec{B}_1$, $\vec{B}_2$, $\left(\vec{U}_2 - \vec{U}_1\right)$, ρ_2, and ρ_1 has been developed by Lepping and Argentiero *(1971)*. The best-estimate values are then used in one of the previous equations, 2.12 or 2.13, to determine $\hat{n}$. However, it is pointed out by Viñas and Scudder *(1986)* that solutions provided by the Lepping and Argentiero method may not be unique due

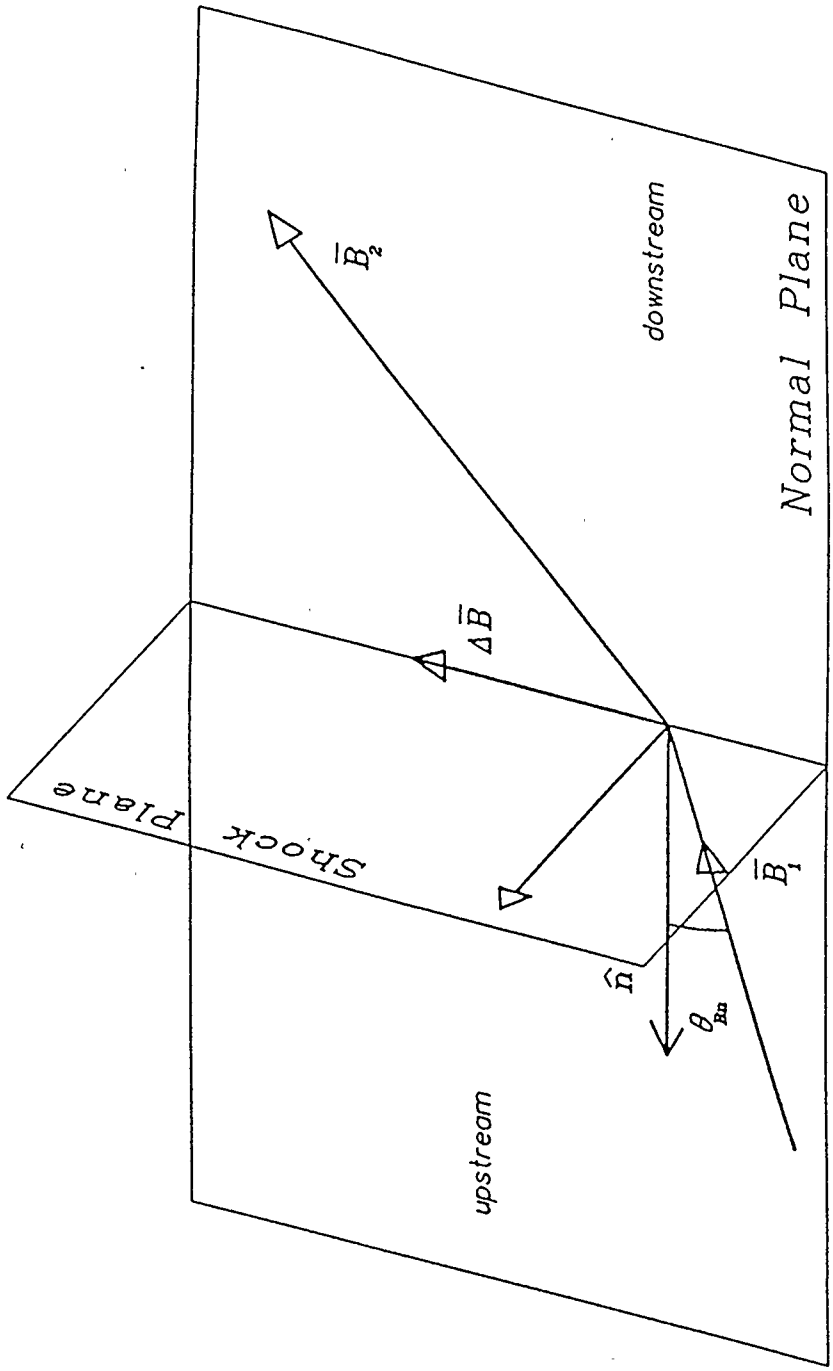

Figure 2.1: The Shock Geometry of the Magnetic Coplanarity Method
According to this method of determining the shock normal, and hence θ_{Bn}, the vector $(\vec{B}_1 \times \vec{B}_2)$ is crossed with $\Delta\vec{B}$ and the resultant is in the direction of the shock normal. This result is normalized as given by equation 2.12.

to the large size of the 11-dimensional parameter space.

Viñas and Scudder *(1986)* have subsequently presented an iterative numerical method for determining the 'geometrical characteristics' of a shock that is said to be reliable at all angles, unlike the coplanarity methods discussed. This method is also a nonlinear least squares method which is performed not on the original 11 parameters of Lepping and Argentiero, which are *intertwined*, but upon 11 separable parameters which can be derived from the original data. The uniqueness of the solution is demonstrated.

Finally, multiple spacecraft methods of inferring the shock geometry have been suggested. These methods assume that the spacecraft are close enough together or that the shock properties do not vary appreciably in the transit time from one spacecraft to the other(s). In general, these conditions are too restrictive and single spacecraft measurements are considered more reliable. Gazis, Lazarus, and Hester *(1985)* describe in detail multi-spacecraft techniques of determining shock parameters.

2.4 Particle Acceleration at Interplanetary Shocks

Shock waves are expected to exist in a variety of situations throughout the universe. Shocks, for example, are proposed to exist at the boundary of supernova remnants. It is by acceleration at these regions that galactic cosmic rays are expected to attain their high energies of approximately 10^{14} eV, according to the extra-galactic theory on cosmic ray origin. On even a larger scale, another shock wave is expected to exist at the termination of the galactic wind *(Jokipii and Morfill, 1985)*, analogous

to the shock expected at the termination of the solar wind. However, the shocks considered in the present study are those found within the heliosphere and which have an origin related to solar processes.

Forman and Webb *(1985)* describe three classes of shocks that exist in the heliosphere:

- Planetary Bow Shocks
- Corotating Shocks
- Travelling Interplanetary Shocks

A discussion of acceleration processes in the region of a planetary bow shock is bypassed as the main physics of such processes is demonstrated sufficiently by the second and third classes. A special issue of the *Journal of Geophysical Research* is concerned with the physics of planetary bow shocks *(**86**, 4317–4536, 1981)*.

A corotating shock, or shock pair as will be seen, results from the interaction between a fast solar wind stream and the slower normal flow of the solar wind. These types of shocks have a tendency to be formed during times of solar minimum, when the characteristic Archimedean spiral arms of the IMF have a better chance to form. Energetic particle enhancements, indicative of an acceleration process, are observed at both shocks in a corotating structure.

Travelling interplanetary shocks are a result of solar impulsive events. A major solar flare acts as a piston which generates a large interplanetary shock wave which propagates approximately radially outwards from the Sun.

Figure 2.2 is a schematic view of the heliosphere, indicating the various classes of possible shocks. As well as planetary bow shocks, corotating shocks, and travelling

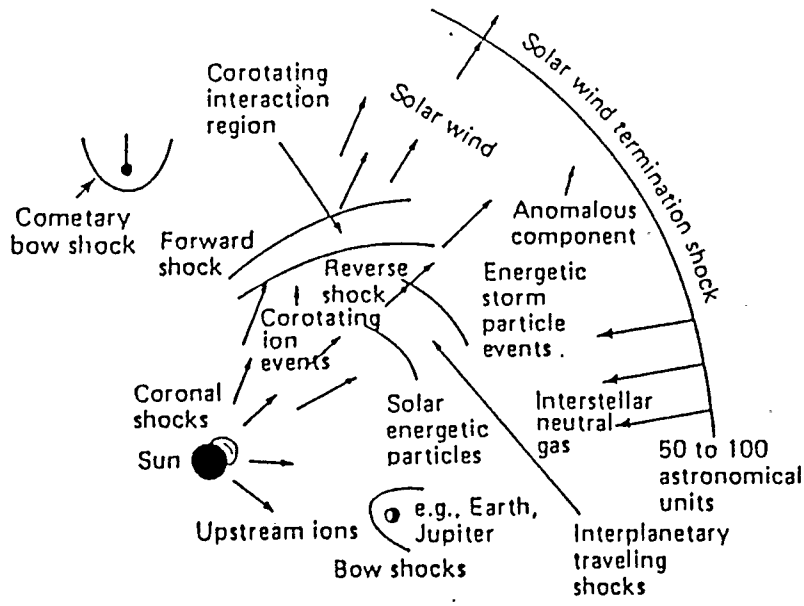

Figure 2.2: Shock Acceleration Regions in the Heliosphere
This diagram schematically indicates the possible regions of charged particle acceleration within the heliosphere. Acceleration is *observed* at planetary bow shocks, corotating shocks, and transient shocks such as those due to solar flares. Acceleration is *hypothesized* at cometary bow shocks and at the heliospheric boundary shock *(Krimigis and Venkatesan, 1988)*.

(transient) shocks, it is seen that perhaps cometary bow shocks and the heliospheric boundary shock are possible regions of charged particle acceleration.

It is well understood that the particular effect of the shock upon the present high-energy charged particle population depends significantly upon the local shock geometry, as described by the shock angle θ_{Bn}. On average, these types of interplanetary shocks are governed by different geometries and hence different acceleration mechanisms are associated with each. Consequently, two acceleration models have been developed. These acceleration processes, namely the *diffusive* and the *shock drift* acceleration methods, will be discussed in detail in this section. It will be

seen that each method is generally associated with a particular optimum shock geometry, and that each is characterized by particular particle enhancements.

2.4.1 Shock Drift Acceleration (SDA)

Consider the shock geometry as shown in Figure 2.3. This is a diagram of a quasi-perpendicular shock wave, the angle between the mean upstream magnetic field and the upstream shock normal, θ_{Bn}, is approximately 75°. Note that the downstream magnetic field is refracted, has the same normal component as the upstream field, and has a greater magnitude than the upstream mean field as described by the magnetic Rankine-Hugoniot relations. A particle can have a trajectory such that it traverses the infinitesimally thin shock front twice in a single gyroperiod. As such, it experiences a *kink* in the magnetic field from the upstream to the downstream region. It is also important to note that the magnetic field in this diagram is directed upstream, if the shock were observed in another magnetic sector the magnetic field may very well be observed to be in the opposite direction. In other words, the relative direction of the mean magnetic field depends upon which magnetic sector the shock is observed in, as discussed in chapter one.

Assume that the magnetic field is essentially homogeneous upstream and downstream of the shock (at least for several particle gyroradii). The absence of any large amplitude fluctuations in the magnetic field provides the cosmic rays with no scattering centers which serve to alter the otherwise helical trajectory. Because of this condition, the acceleration at quasi-perpendicular shocks is sometimes referred to as *scatter-free* acceleration.

There is an induced electric field, as observed in the shock frame (in which the

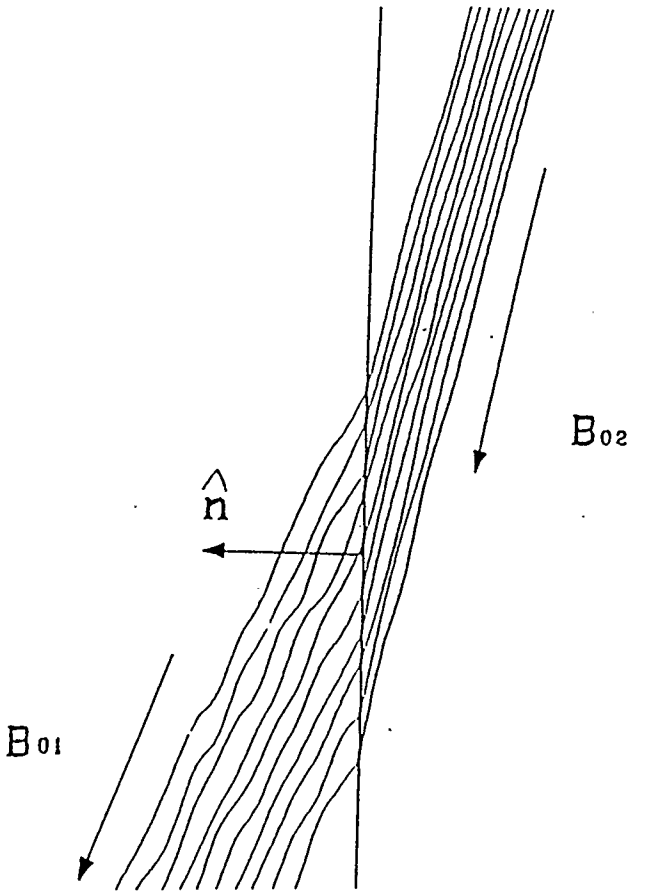

Figure 2.3: The Geometry of a Quasi-Perpendicular Shock

This schematic diagram of the geometry of a quasi-perpendicular shock displays the refraction of the magnetic field downstream, the conserved normal component of the magnetic field and the resultant increase in magnitude of the magnetic field across the shock front as described by the magnetic Rankine-Hugoniot equations. A particle which exists within a gyrodiameter of the shock front will experience a *kink* in the magnetic field as it crosses the shock front twice per gyroperiod. The value of the shock normal angle, θ_{Bn}, in this case is 75°.

magnetic Rankine-Hugoniot equations were presented), given by

$$\vec{E} = -\frac{\vec{U}_1 \times \vec{B}_{01}}{c} \tag{2.14}$$

where $\vec{B}_{01}$ is the mean upstream magnetic field and $\vec{U}_1$ is the (shock frame) flow velocity of the upstream plasma (carrying with it the magnetic field) into the shock front. The direction of the electric field in Figure 2.3 is out of the paper.

The jump conditions immediately indicate that this electric field is equivalent in both the upstream and the downstream regions. A charged particle will experience an acceleration, or a *drift*, along this induced electric field. Particles with a charge Zq will increase their energy by an amount $(Zq)(|\vec{E}|)(d)$ where d is the distance particles drift in the electric field. Ions are accelerated in a direction parallel to the electric field and electrons are accelerated anti-parallel to the electric field.

The physical interpretation of the induced electric field is easily understood if one considers the force upon a low energy charged particle from a different reference frame. Consider a reference frame fixed to the upstream magnetic field. In this frame, the shock has a velocity of $-\vec{U}_1$. A particle in the vicinity of the shock front, and with the approximate same velocity as the shock, experiences a transverse magnetic deflecting force (a *Lorentz force*), $\vec{F}_m$, given by

$$\vec{F}_m = -\frac{q(\vec{U}_1 \times \vec{B}_{01})}{c} \tag{2.15}$$

Now consider an observer in the shock frame. He observes a charged particle accelerating in a direction out of the paper and concludes that the motion of the upstream magnetic field induces an electric field in this direction. The force upon

the charged particle by this electric field is given by

$$\vec{F}_e = q\vec{E} \tag{2.16}$$

Of course, $\vec{F}_m$ and $\vec{F}_e$ must be equal since they describe the motion of the same particle. Equating 2.15 and 2.16 one obtains equation 2.14, the value for the induced electric field as observed in the shock frame.

It is obvious that a particle can gain more energy if it interacts with the shock more than once, or more specifically, for a longer time. An interaction actually consists of many shock crossings by the particle. An interaction is defined to end when a particle propagates to a distance from the shock which is greater than a gyroradius. The significant factor is the parallel component of the particle's velocity along the magnetic field lines. If the velocity of the intersection of a field line with the shock front, $\vec{V}_t$, where $\vec{V}_t = -\vec{U}_1 \sec\theta_{Bn}$, is faster than the parallel component of the particle's velocity, and the particle is upstream, then the shock will overtake the particle and the shock drift acceleration may occur. If the particle is initially downstream, the shock will never interact with the particle. Conversely, if $\vec{V}_t$ is less than the parallel component of the particle's velocity, upstream particles will outrun the shock and downstream particles will overtake the shock and again SDA may occur. These dynamics become very important if mechanisms such as $\nabla\vec{B}\|\vec{B}$ magnetic scattering centres exist either up or downstream which will cause the particles to reflect back towards the shock; that is, if multiple interactions are to exist.

2.4.2 Diffusive Shock Acceleration

In contrast to the case of SDA, the diffusive acceleration mechanism does rely upon the imhomogeniety of the magnetic field in the region of the shock front both up and downstream. The presence of magnetic fluctuations provides the opportunity for the particles to be scattered in *pitch angle*, the angle between the particle's instantaneous velocity vector and that of the local magnetic field. That is, $\nabla\vec{B}\|\vec{B}$ magnetic scattering centers exist in the upstream and downstream magnetic fields.

Consider the quasi-parallel geometry in Figure 2.4. The value of θ_{Bn} with respect to the mean upstream field is 25° in this diagram. Immediately obvious is the refraction of the downstream field, it is significantly less than that for the quasi-perpendicular case. As a result, the increase in magnitude across the shock is less for quasi-parallel shocks. The physical process which is of importance in the diffusive acceleration mechanism is not only related to the up and downstream magnetic fields but to the up and downstream plasma flow velocities as well.

In the shock frame, the magnitude of the normal component of the downstream plasma flow velocity is less than that of the upstream flow velocity. As a result of this difference in velocity, the upstream and downstream scattering centers (that is, the MHD waves present in the plasma) converge. The MHD waves in the plasma are convected with approximately the plasma flow speed. This is exactly the well known first order Fermi mechanism: a charged particle will be accelerated if it is trapped between two convergent magnetic scattering centers. This is because of an attempt by the particle to conserve its first adiabatic invariant. This is referred to as diffusive acceleration because the same set of equations used in the more general

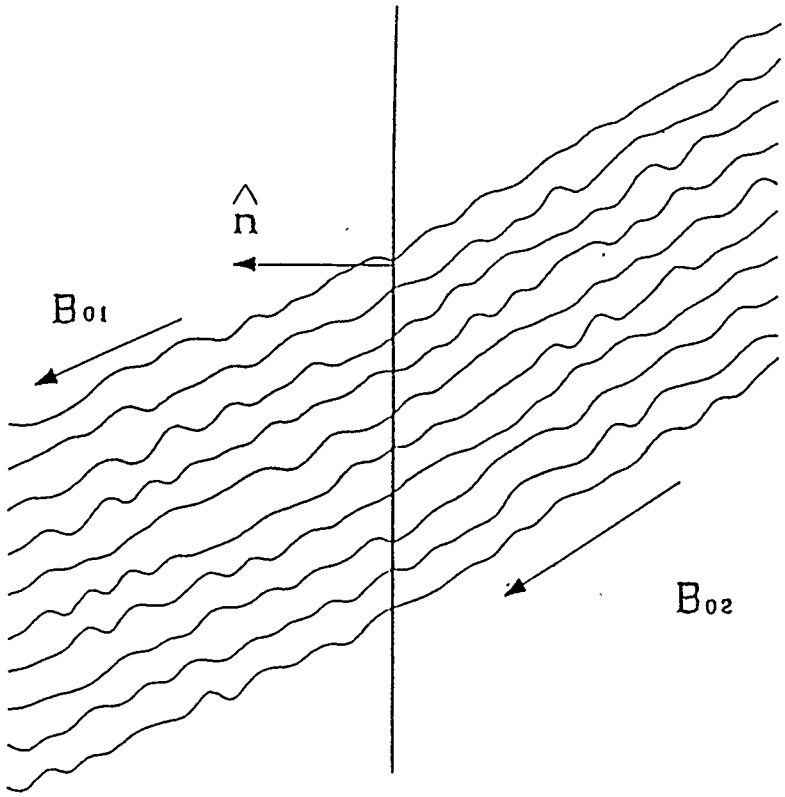

Figure 2.4: The Geometry of a Quasi-Parallel Shock

This schematic diagram represents the geometry of a quasi-parallel shock in the heliosphere. The downstream magnetic field lines are only slightly refracted and the increase in the magnitude of the magnetic field across the shock is much less than that for quasi-perpendicular shocks. The MHD waves, or *scattering* centers, in the up and downstream plasmas provide the opportunity for charged particles to be scattered in pitch angle. Particle trajectory reversals are possible in this geometry indicating a Fermi first-order acceleration mechanism may occur.

description of cosmic ray modulation in the heliosphere can be used to describe this situation.

Finally, it is important to note that the SDA and diffusive acceleration mechanisms need not be considered to operate independently. Each mechanism can contribute to the total acceleration of a charged particle for a shock whose geometry is oblique, its value of θ_{Bn} being between the values used in the description of quasi-parallel and quasi-perpendicular shocks. This point will be returned to in chapter five. The simulation described in chapter five attempts to combine both mechanisms by introducing magnetic fluctuations in both the upstream and downstream magnetic fields. The presence of the flucutations provides the opportunity for diffusive acceleration to occur as well as increasing the shock-particle interaction time via particle trajectory reversals, making the SDA mechanism more effective.

Chapter 3

THE DATA INTERVAL

3.1 The Voyager Plasma and Field Data

The data to be presented in this chapter was supplied by the Space Science group at The Johns Hopkins University/Applied Physics Laboratory. This data consists of the magnetic field and solar wind plasma data as obtained by the Voyager 1 and 2 spacecraft during the time interval from day-of-year (DOY) 100 to DOY 180, in the year 1979. The particle data for this same time period will be presented in chapter four.

The trajectories of Voyagers 1 and 2, in the heliocentric coordinate system, over the time interval DOY 100–180, 1979 are presented in Figure 3.1. The coverage was excellent during this interval in anticipation of the impending Voyager 2-Jupiter encounter on DOY 190, 1979. The trajectory of Voyager 1 is indicated by the dashed line, that of Voyager 2 by the solid line. It is seen that the two spacecraft were never separated by more than $\sim 5°$ in heliolongitude and $\sim 0.35°$ in heliolatitude during this interval. The larger gradient in the heliolatitude and heliolongitude curves of Voyager 1 are a result of its DOY 64, 1979 interaction with Jupiter. During this interval the spacecraft increased their radial distance from the Sun at almost an equal rate of ~ 0.004 A.U. per day.

The remainder of this section deals with a brief review of the description of corotating features in the heliosphere, the presentation of the available Voyager

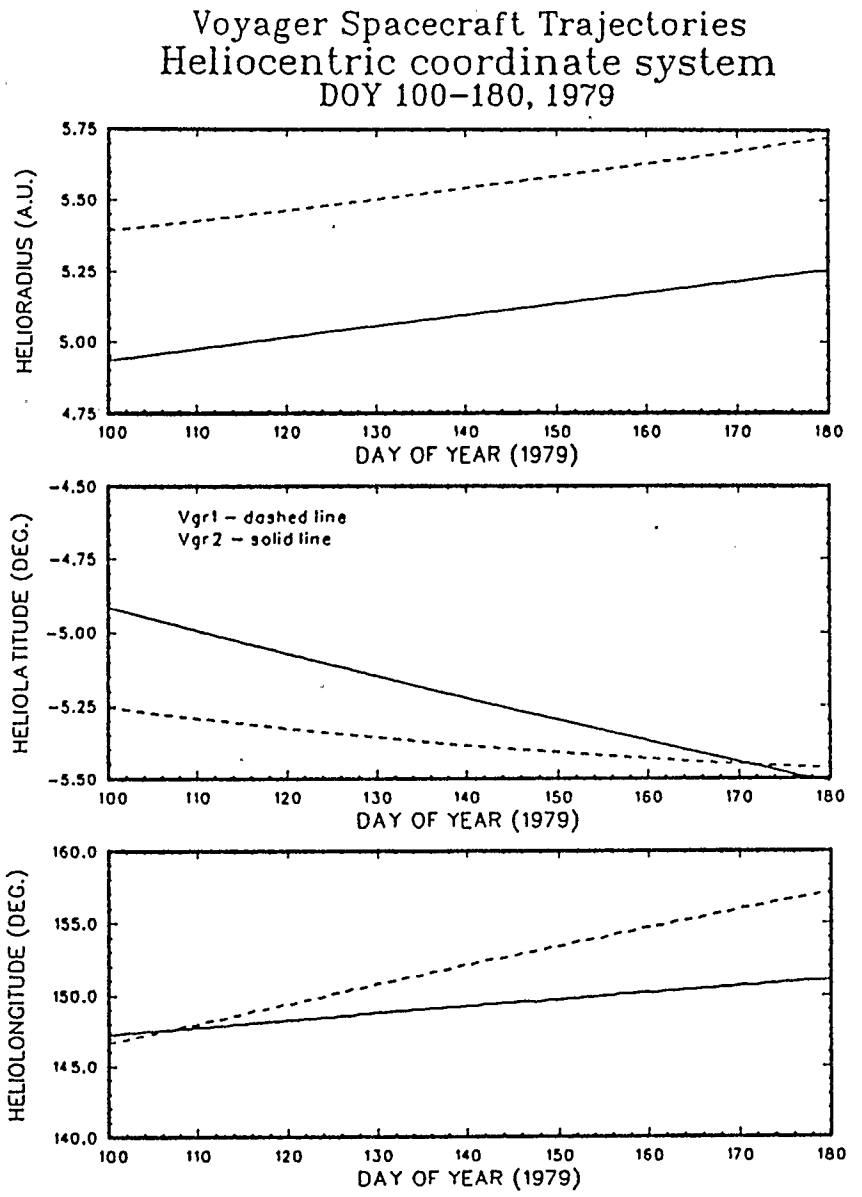

Figure 3.1: The Voyager Spacecraft Trajectories, DOY 100–180, 1979
The trajectories of both Voyager spacecraft over the time interval DOY 100–180, 1979 are presented. The trajectory of Voyager 1 appears as the dashed line, that of Voyager 2 as the solid line. Over this interval the two spacecraft are very nearly radially aligned.

solar wind and magnetic field data, and the determination of the propagation speed of features observed in the data. The next section is concerned with the positive recognition of corotating features over the data interval as observed by both Voyager spacecraft. Evidence indicating the presence of three recurrences of two corotating interaction regions in the data is presented, as well as any suggesting that there are associated corotating shock pairs. Finally, the results of the determination of the shock normal angles for the probable shocks are presented.

3.1.1 Corotating Interaction Regions

As the name suggests, a corotating interaction region (CIR) is a feature observed in the solar wind and/or field data which corotates with the arms of the Archimedean spiral of the Parker model of the IMF. The existence of CIR's was expected even before the direct observations by the Pioneer and Voyager spacecraft. Several very readable review articles regarding the spacecraft observations have appeared *(Burlaga, 1971; Smith and Wolfe, 1977; Smith and Wolfe, 1979; Burlaga, 1984; Hundhausen, 1985; Smith, 1985)*. A brief description of the formation of a CIR in the heliosphere as well as the effects it has upon the local conditions follows.

A CIR is the result of the interaction between a high-speed stream from a polar coronal hole, for example *(Smith, 1985)*, and the slower plasma ahead of it. The source of the high speed stream could also be from a relatively long lasting solar flare *(Steinolfson et al., 1975)*. Hundhausen and Burlaga *(1975)* have discussed the origin of such an interface between a slow and fast moving stream set at 1 A.U., based on a gas dynamic model. They conclude that variations in temperature within the solar envelope can result in the high speed stream. Figure 3.2 is a

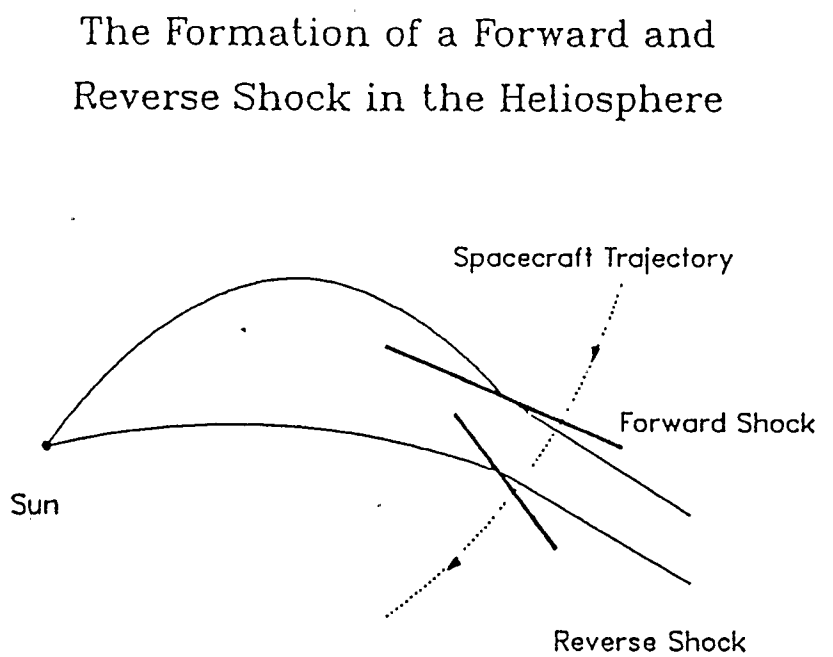

Figure 3.2: The Formation of Heliospheric Forward and Reverse Shock Pairs
A high-speed stream will carry with it a field line which will advance into the slower plasma and associated field lines upstream. The compression of the region between the two streams, the *interaction region* will be counteracted by the magnetic pressure within. The large magnetic, pressure, density, and velocity gradients that build up can steepen into shock waves at the regions indicated.

schematic diagram of how a CIR might form. A high speed stream is emitted from the Sun as shown in the bottom streamline in the figure. Since the longitudinal component of the IMF is inversely proportional to the solar wind speed (recall chapter 1, section 1.2.3), it is easily seen that the field lines attached to the high speed stream compress the field lines and plasma in the direction of the rotation.

Figure 3.2 is only a two-dimensional representation of a corotating interaction region, Siscoe *(1976)* provides a model of a corotating interaction in three dimen-

sions. The general shape has been described as that of a Chinese pennant, the latitudinal extent of the CIR increasing with radial distance.

A quick calculation based upon the ideal (Parker) IMF model indicates that a field line attached to a typical high-speed plasma flow of 750 km/s will intersect a field line attached to a normal stream of 400 km/s originating from a solar longitude of 60° ahead of the high-speed source at a radial distance of about 2.2 astronomical units. Of course, there will exist a magnetic pressure inside of the interaction region which will prevent an actual intersection of the field lines. As a result of the impinging high speed stream into the slower plasma upstream, large pressure, density and velocity gradients will form, providing the opportunity for a shock wave to form as discussed in chapter 2.

As indicated in Figure 3.2, two shock waves may result as the steepening of the velocity and pressure gradient increases. The leading shock is referred to as the *forward shock* and the trailing shock is referred to as the *reverse shock*. The names refer to the direction of propagation as viewed from within the interaction region, the region contained by the high and slow speed streams. Both shocks propagate in the same direction in the inertial frame, of course, the reverse shock having the smaller helioradial propagation speed. The trajectory of a spacecraft initially upstream of the forward shock is shown, in the corotating reference frame. The spacecraft samples these regions in sequence: upstream of the forward shock, downstream of the forward shock, downstream of the reverse shock, and finally upstream of the reverse shock. This sequence has a specific signature in the plasma and field data.

Figure 3.3 schematically indicates the expected intensity profiles of the local

Morphological Features in a
Corotating Interaction Region

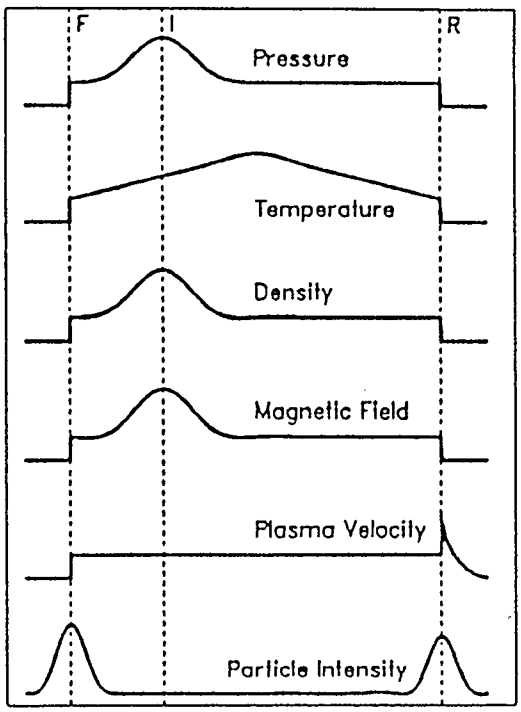

Figure 3.3: The Morphological Features in a Corotating Interaction Region
Shown are the morphological profiles of the local plasma variables in the region of a corotating interaction region as a function of time. The symbols F, I, and R refer to the forward shock, interaction region, and reverse shock, respectively. The large increase in the intensity of high-energy particles is observed at the location of the forward and reverse shocks. This is the result of acceleration processes which occur at the shock vicinities.

plasma and field variables as recorded by a spacecraft with the trajectory as shown in Figure 3.2. The large intensity increase in the high-energy particle population is a result of the acceleration processes ongoing in the vicinity of the shock fronts. The vertical dotted line labelled F refers to the passage of the forward shock. Similarly, R refers to the passage of the reverse shock, first the downstream region and then the upstream region is sampled. The vertical dotted line labelled I refers to the location within the interaction region where the accelerated plasma is separated from the decelerated plasma *(Smith and Wolfe, 1979)*. It is to be noted that the horizontal scale is of the order of about 3–5 days at about 3–5 astronomical units.

The pressure within the CIR is the sum of the particle kinetic pressure and the magnetic pressure, it exhibits a large peak within the interaction region. Naturally, the plasma particle density and the magnitude of the magnetic field have a maximum at this same time. The temperature profile can have a different profile than is indicated, but that shown is indicative of a typical event *(Smith and Wolfe, 1977; Smith and Wolfe, 1979)*. Perhaps the most distinctive profile belongs to the solar wind plasma velocity. Within the CIR the magnitude of the plasma velocity is seen to be greater than that of the normal flow which exists upstream of the forward shock. The passage of the reverse shock is demonstrated by the large velocity gradient which decays in time back to pre-CIR passage levels. This large peak is the high-speed stream attempting to penetrate the slower plasma downstream of the reverse shock.

The profiles indicated in Figure 3.3 are only schematic diagrams of an idealized CIR passage and its associated shock pair. In general, these profiles are only observed in a few instances in spacecraft data. If the spacecraft is not yet beyond

a radial distance where the shock pair may have formed, the infinite gradients in the local variables will not be observed. Instead, gradual increases in these quantities may be observed in the leading edge and corresponding gradual decreases may be observed at the trailing edge. If the spacecraft is at a much farther radial distance than where corotating shocks typically form, the shock waves may have already dissipated into large amplitude MHD waves. Again the infinite gradients will be replaced by gradual increases and decreases. It will be seen in the next section that there is an optimum radial distance where forward and reverse shock pairs tend to form and corotate for as many as a dozen solar revolutions before they dissipate.

3.1.2 The Voyager 2 Data

The most extensive data set available for this study, over the specified time interval, belonged to the Voyager 2 spacecraft. The solar wind plasma data was available in the form of the magnitude of the solar wind velocity. It was assumed that the direction of propagation of the solar wind was entirely in the radial direction, consistent with the Parker model of the IMF. The vector magnetic field data was available as measured by the magnetometer aboard the spacecraft. The data was available in hourly averages. The implications of this low resolution will be discussed. The data available to this study from Voyager 1 consisted only of the solar wind magnitude. Voyager 1 encountered Jupiter on DOY 64 of 1979, just 5 weeks prior to the interval of concern here.

Figures 3.4 through 3.9 display the magnitudes of the solar wind velocity and magnetic field as measured by Voyager 2, as well as the components and relative standard deviation of the field. The quantities are hourly averages. Significant

data gaps fortunately appear only in the first fifteen days (Figure 3.4).

The magnetic field magnitude ($|\vec{B}| = F$) is measured in *gammas* (One gamma equals 10^{-5} gauss.). The field components are exhibited in the RTN coordinates described in chapter 1, subsection 1.2.3. Recall that for large values of radial distance, the value of λ_B is predominantly 90° or 270°, depending upon which magnetic sector the spacecraft is in at the time of the observations. The relative standard deviation of the field is given by the directional standard deviation of the field, σ, divided by the field magnitude F, where σ is given by:

$$\sigma = \sqrt{\sigma_r^2 + \sigma_t^2 + \sigma_n^2} \tag{3.1}$$

where σ_r^2, σ_t^2, and σ_n^2 are the hourly field variances in the radial, tangential, and normal directions, respectively. Note that the relative standard deviation of the field is presented on a logarithmic scale. The value of the ordinate represents the respective exponent of 10 of the ratio σ/F.

Inspection of the solar wind and magnetic field magnitude profiles over this data set reveals features similar to those discussed in the previous subsection. That is, six corotating interaction regions are identifiable in this time period. A careful examination of the data reveals, to within the one hour resolution of the data, the best estimate of the spacecraft detection of the passage of the leading and trailing plasma velocity and field gradients. These are summarized in Table 3.1. Entries marked with an asterisk indicate that a data gap exists at the point of an anticipated CIR boundary. The identification of a boundary at these points was by visual interpolation.

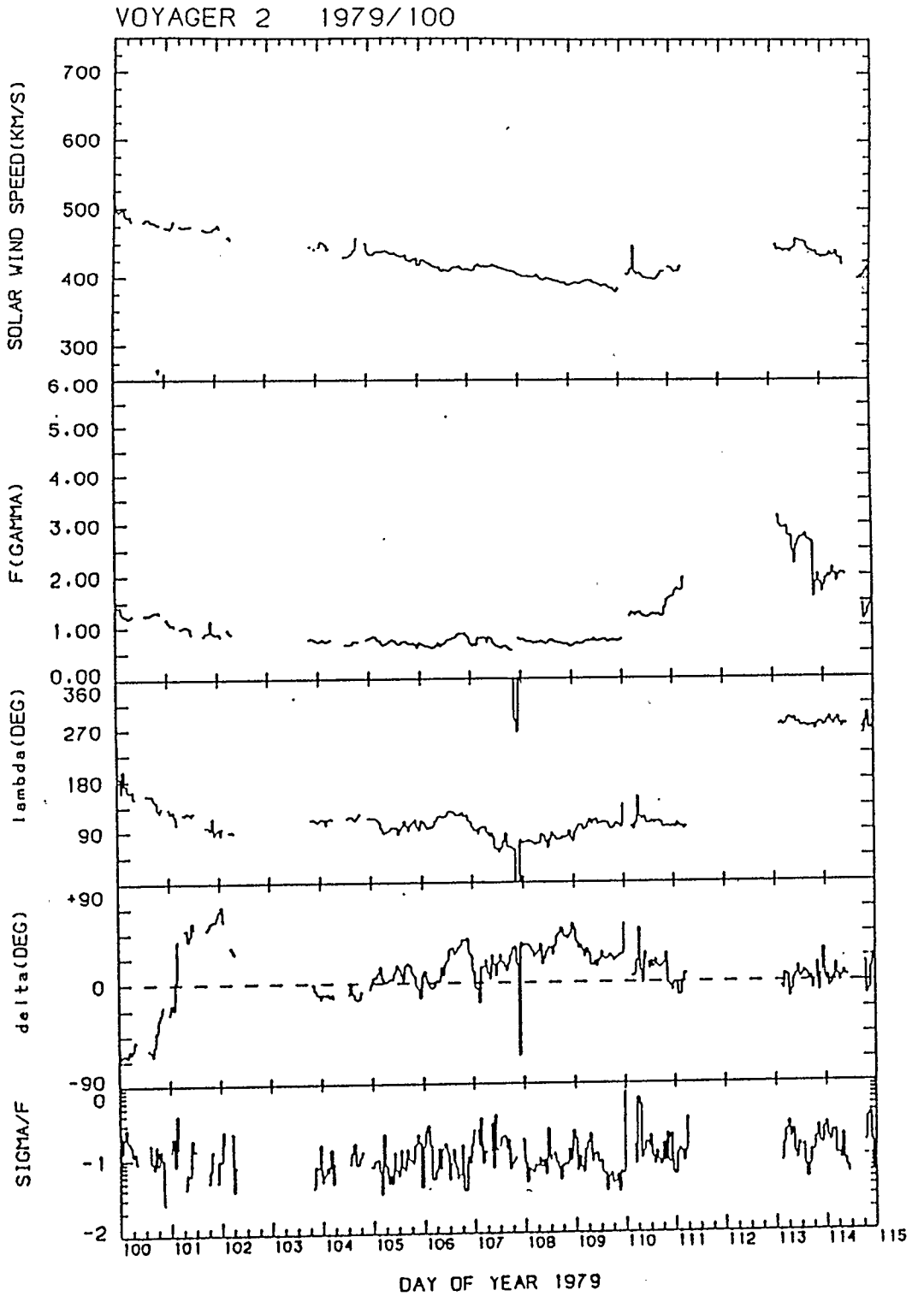

Figure 3.4: The Voyager 2 Data Set: DOY 100–115, 1979

Presented here is the solar wind magnitude and the vector magnetic field data as measured by the Voyager 2 spacecraft from DOY 100 to DOY 115, 1979.

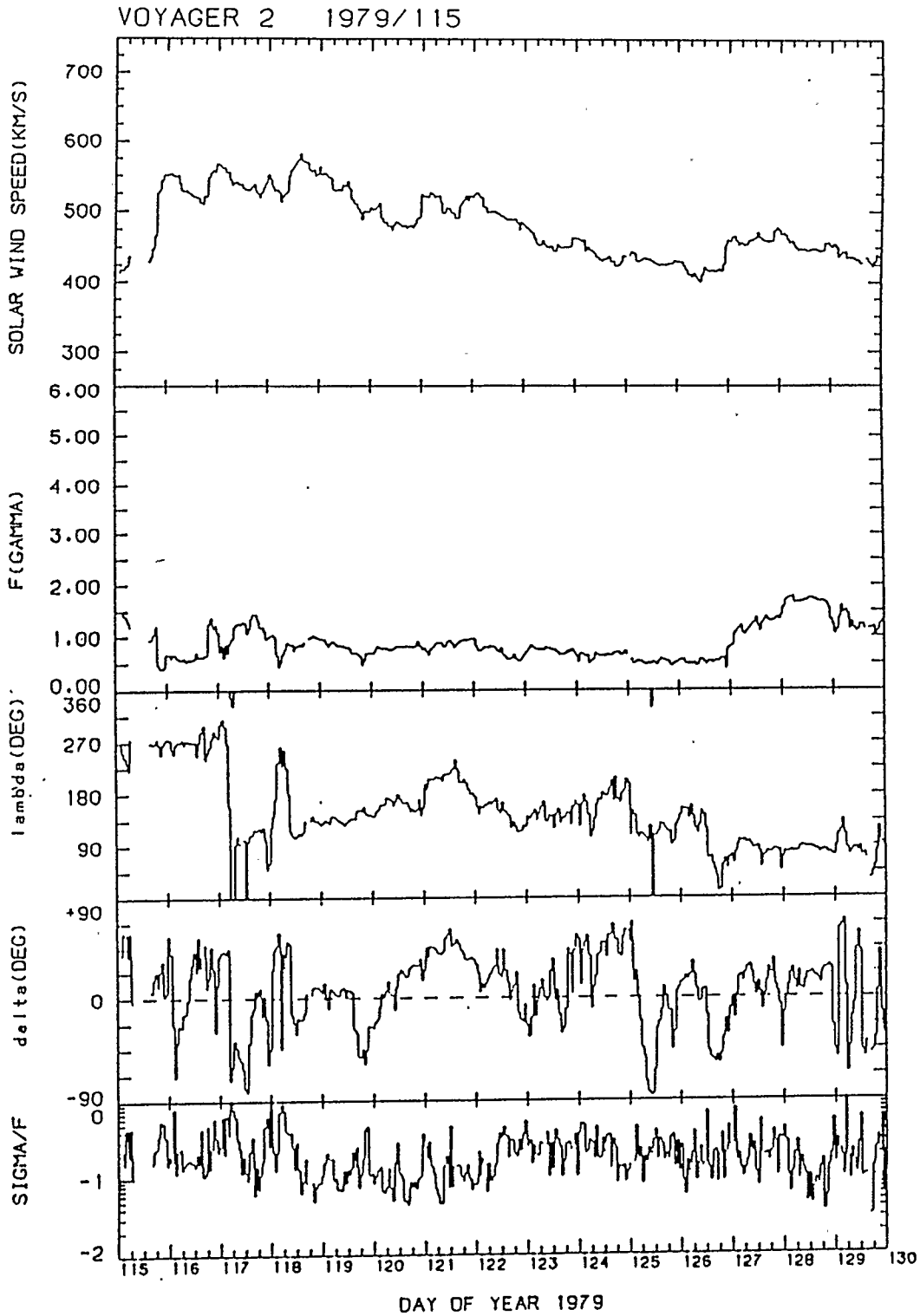

Figure 3.5: The Voyager 2 Data Set: DOY 115–130, 1979

Presented here is the solar wind magnitude and the vector magnetic field data as measured by the Voyager 2 spacecraft from DOY 115 to DOY 130, 1979.

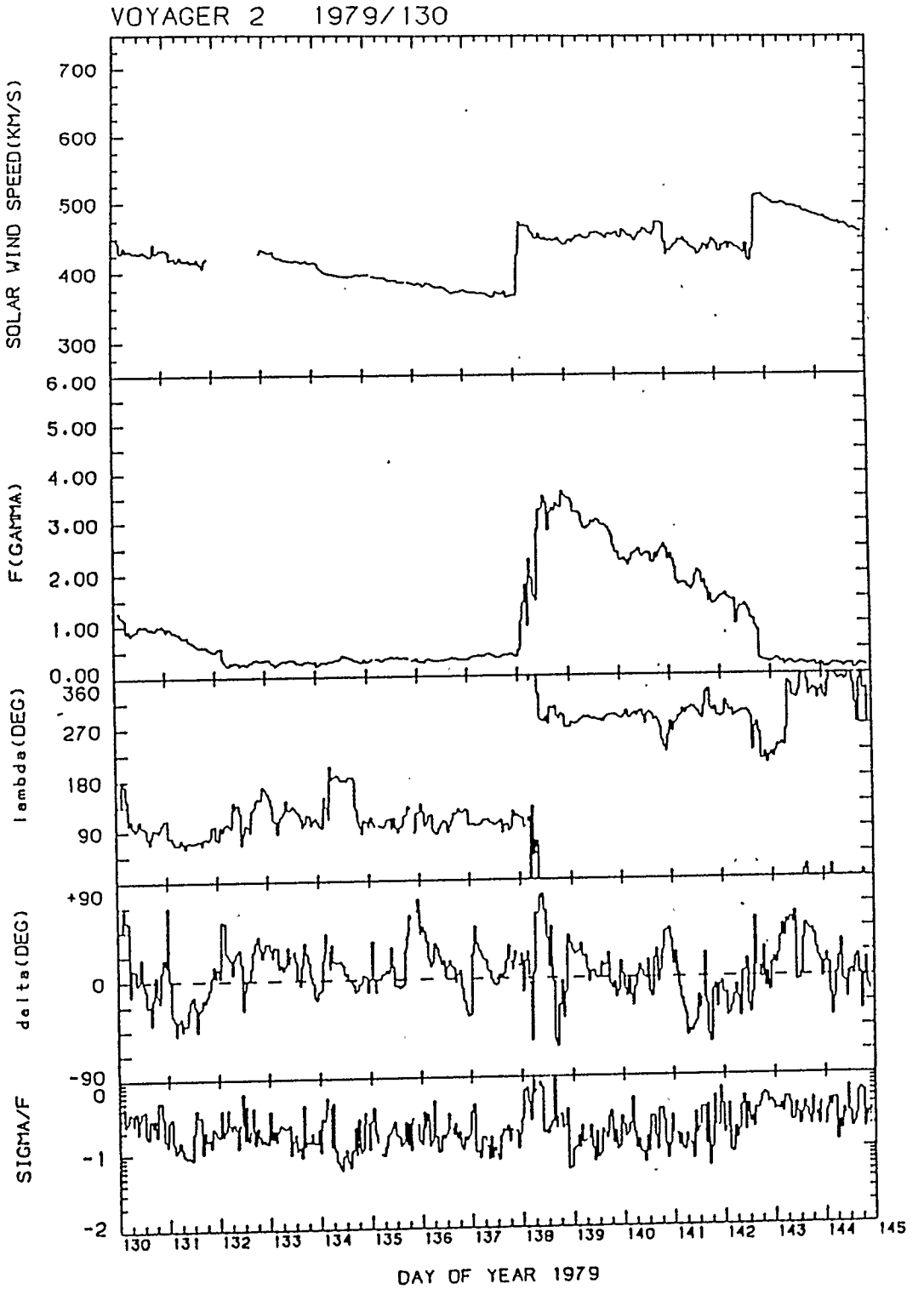

Figure 3.6: The Voyager 2 Data Set: DOY 130–145, 1979

Presented here is the solar wind magnitude and the vector magnetic field data as measured by the Voyager 2 spacecraft from DOY 130 to DOY 145, 1979.

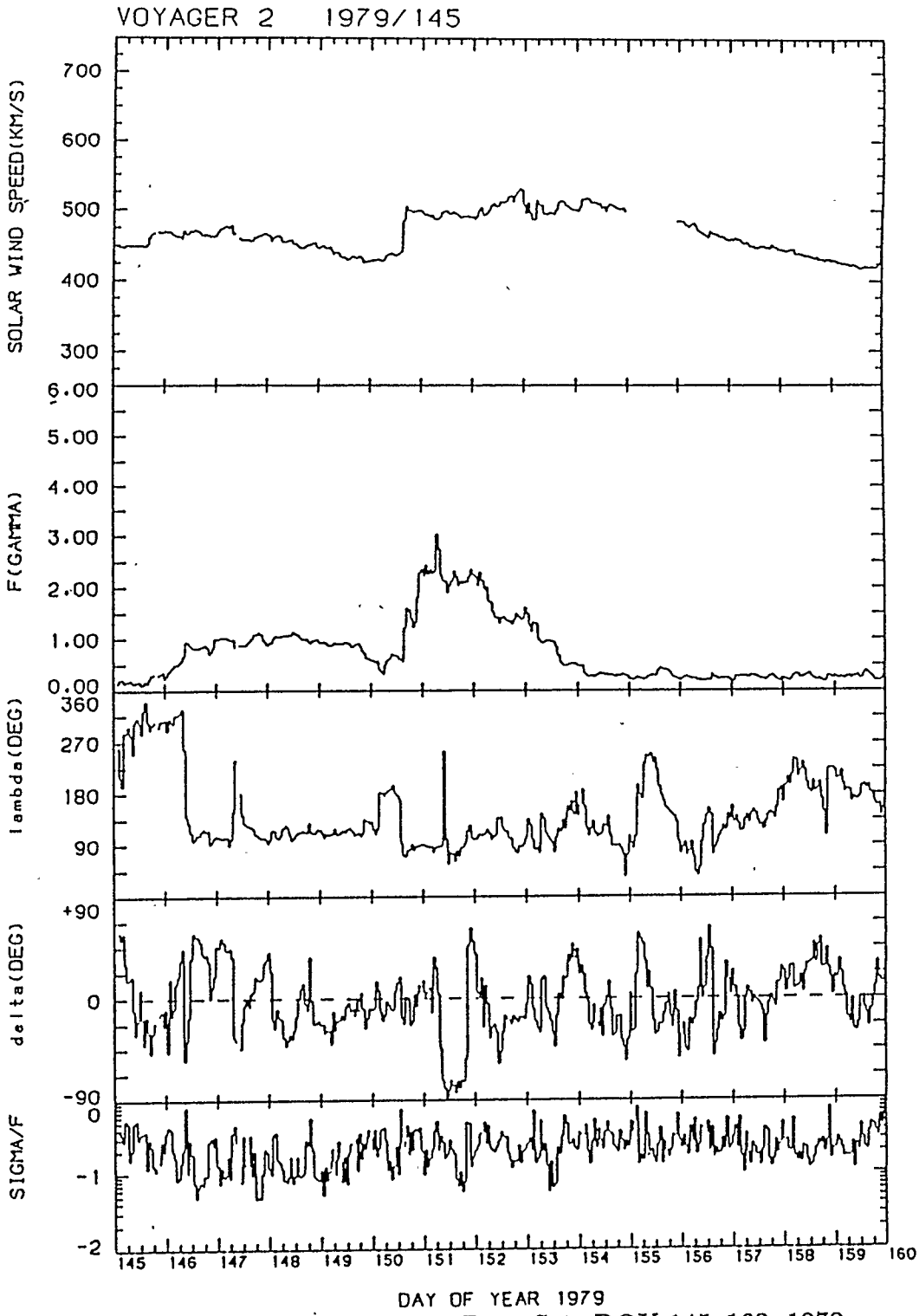

Figure 3.7: The Voyager 2 Data Set: DOY 145–160, 1979

Presented here is the solar wind magnitude and the vector magnetic field data as measured by the Voyager 2 spacecraft from DOY 145 to DOY 160, 1979.

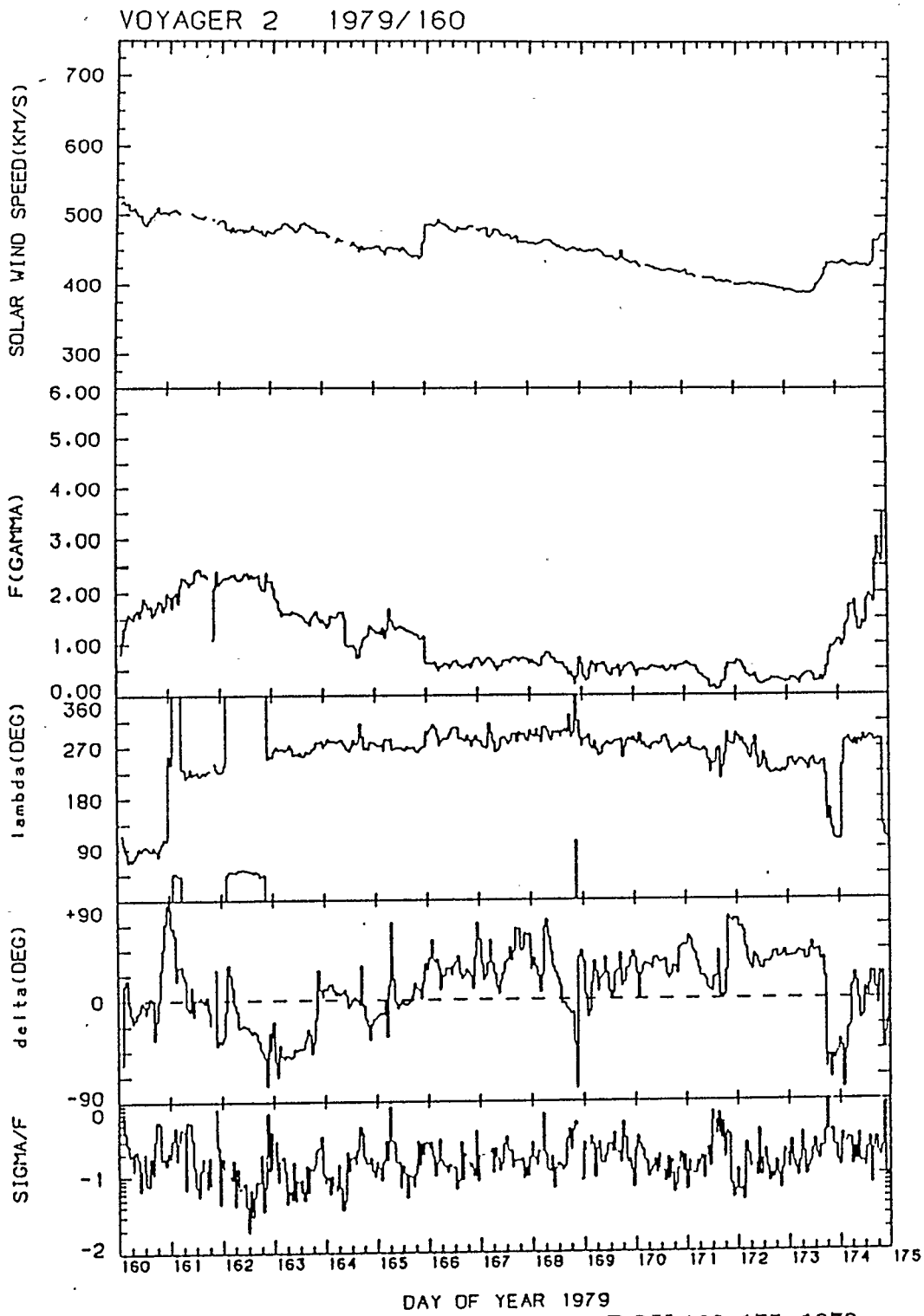

Figure 3.8: The Voyager 2 Data Set: DOY 160–175, 1979

Presented here is the solar wind magnitude and the vector magnetic field data as measured by the Voyager 2 spacecraft from DOY 160 to DOY 175, 1979.

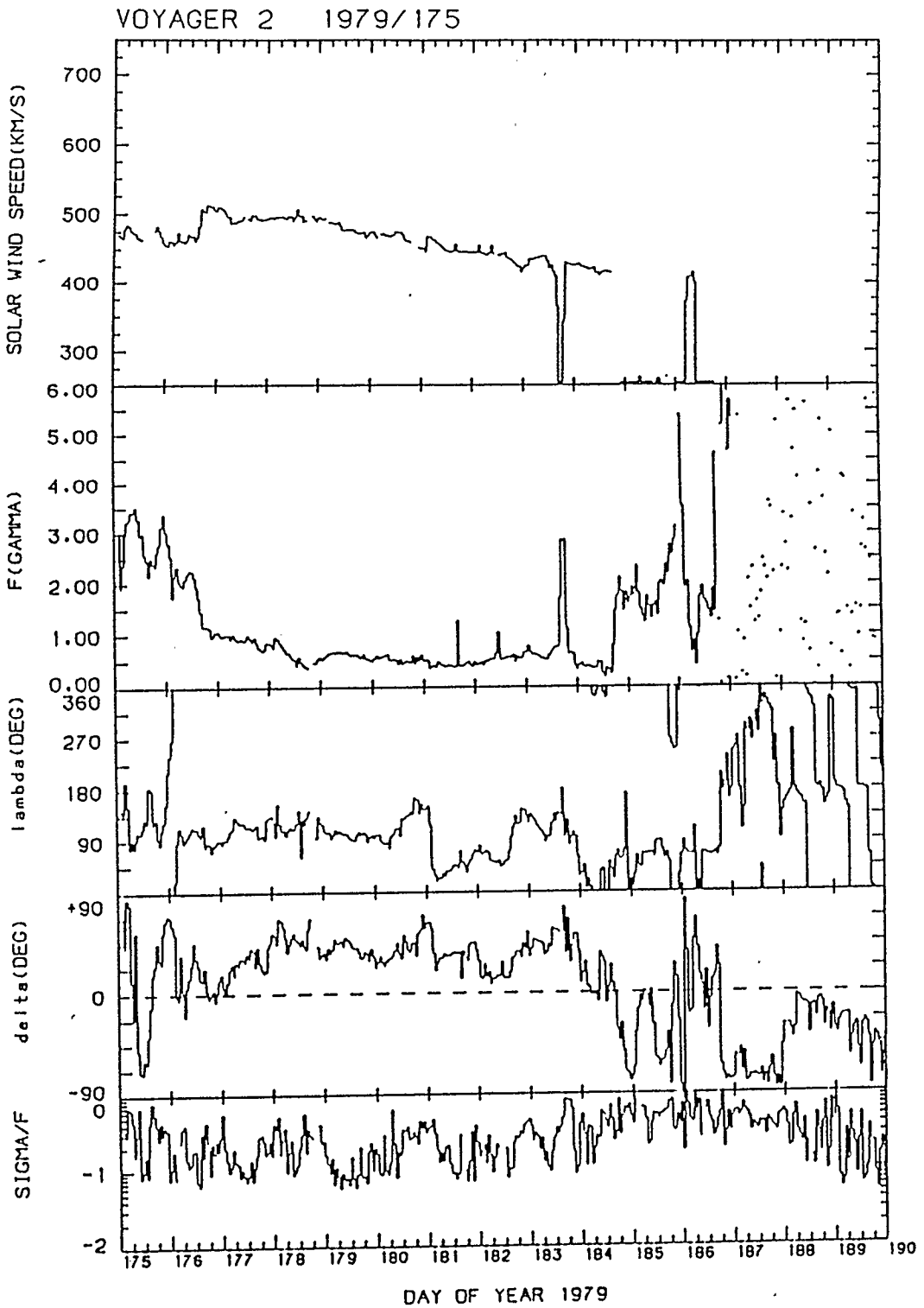

Figure 3.9: The Voyager 2 Data Set: DOY 175–190, 1979

Presented here is the solar wind magnitude and the vector magnetic field data as measured by the Voyager 2 spacecraft from DOY 175 to DOY 190, 1979.

CIR	1	2	3	4	5	6
leading	110, 01*	126, 22	138, 01	150, 14	159, 22	174, 18
trailing	115, 21	132, 02*	142, 17	153, 13	165, 23	176, 15

Table 3.1: The Six CIR's as Detected by Voyager 2
The entries in this table represent the best estimate of the time of passage of the leading and trailing edge of the six suspected corotating interaction regions observed within the data interval of concern. The times indicated are DOY, hour. Entries marked with an asterisk indicate data gaps.

It will be argued in the next section that these six observed CIR's are actually three recurrences of the same two. Evidence supporting the existence of associated shock pairs with these two CIR's will be provided as well. This evidence follows from close examination of the available solar wind plasma and magnetic field data. The available particle data will be reviewed in detail in chapter 4.

3.2 The Recognition of Two Distinct CIR's

The data presented in the previous subsection is subjected to a rigorous examination in this section. Specifically, evidence indicating that the six CIR's observed in the Voyager 2 field and plasma data are actually three recurrences of the same two will be presented. The possibility of a forward and reverse shock pair associated with each of the CIR's will be discussed.

3.2.1 The Period of the Recurrence

The primary test that the features observed in the Voyager 2 data set must be consistent with is a test of their periodicity. That is, if they are to be considered

as features which are recurrent due to the solar rotation, their period of recurrence must be comparable to that of the sidereal period of the latitude from which they originate on the Sun. The sidereal period of the equatorial region on the Sun is approximately 27 days, increasing to $\sim$ 37 days near the poles.

It proves convenient to define a simple notation which describes a particular recurrent feature as observed in the spacecraft data. The notation used will involve the use of a double index; the first index will refer to the *occurrence* of the feature and the second index will refer to the *identification* of the feature. For example, CIR(1,2) refers to the first occurrence of the second CIR, F(2,1) refers to the second occurrence of the first presumed forward shock.

If the assumption is made at this point, as yet unqualified, that a forward shock exists at the leading edge and a reverse shock exists at the trailing edge of each of the CIR's, then periodicities in the recurrence of the two presumed forward and reverse shocks can also be investigated. The times of the presumed shock passages are then given by Table 3.1.

Figure 3.10 is an attempt to represent any periodicities in the CIR's, as defined by their respective presumed forward and reverse shock waves. Each *cell* in Figure 3.10 represents a single day. The upper left-hand cell is DOY 102, 1979 and the lower right-hand cell is DOY 197, 1979. There are 24 days per row in the diagram and thus any feature which occurs cyclically with a period of 24 days should be seen in each cell of a vertical column. The passage times of the presumed forward shock waves are indicated by the heavy, solid lines and those of the reverse shocks by the heavy, sparsely dotted lines. Also shown in the diagram are the daily average values of the longitudinal angle of the IMF, λ_B. In this diagram, λ_B is represented

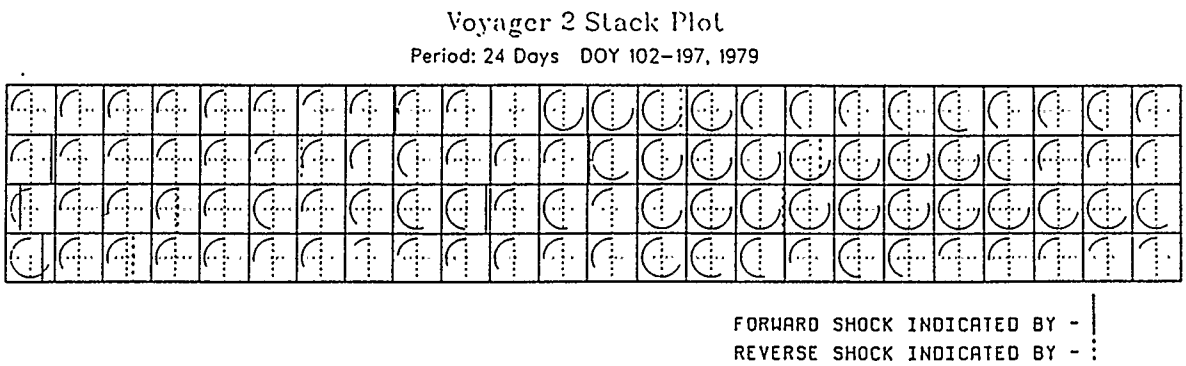

Figure 3.10: Stack Plot of the Voyager 2 Observations in the Data Interval
Each cell in this stack plot represents a single day, the upper left-hand cell is DOY 102, 1979 and the lower right-hand cell is DOY 197, 1979. Indicated is the value of the daily average of λ_B as given by the angle subtended by the arc segment. The location of the presumed forward and reverse shocks at the leading and trailing edges of the 6 CIR's are also shown.

by the arc segment measured counterclockwise from the direction towards the top of the diagram. The sector structure is evident, based on the frequency of the daily averages of λ_B near 90° and 270°.

The choice of 24 days as the period of the *stack plot* was arbitrary, it allowed the vertical alignment of the three recurrences of the presumed second forward shock (F(1,2), F(2,2), and F(3,2) appear in the second, third, and fourth cells of the first column). What is of more importance is the period of the recurrence of the time midpoint of the CIR's, rather than the leading or trailing boundary. This is because the shocks have a propagation velocity not indicative of the general corotating flow. The forward shock has a positive radial velocity and the reverse shock has a negative radial velocity as observed from within the CIR plasma frame. Table 3.2 shows the amount of time between successive passages of the time midpoint of the

CIR Pair	Period
CIR(1,1)-CIR(2,1)	27 days, 10 hrs
CIR(2,1)-CIR(3,1)	22 days, 14 hrs
CIR(1,2)-CIR(2,2)	22 days, 14 hrs
CIR(2,2)-CIR(3,2)	23 days, 15 hrs

Table 3.2: The Period of the Two Observed CIR's, Voyager 2
Shown is the time between successive passages of the three presumed occurrences of the two CIR's as detected by Voyager 2. The period is somewhat less than that of the sidereal period of the equatorial solar region of 27 days.

observed CIR.

Table 3.2 indicates that the period of the observed CIR's is less than that of the solar equatorial sidereal period. This is most easily explained by noting that the leading and trailing edge of the CIR's, that is the presumed forward and reverse shocks, have a propagation velocity which is higher than that of the ambient plasma flow. This larger velocity would reduce the period as observed by the spacecraft detectors.

It is to be emphasized that the conclusion that CIR(1,1), CIR(2,1), and CIR(3,1) are the same feature and that CIR(1,2), CIR(2,2), and CIR(3,2) are the same feature is the optimum conclusion based upon the evidence presented in this section. No significant features other than these appear either before, during or after this time interval. No mistaken recognition of the periodicities can occur due to *aliasing*, or wrongful interpretation as a result of undersampling of the periodic data. There is yet another irrefutable piece of evidence to support this conclusion. The observation of the sector structure observed in the λ_B magnetic field angle displayed in Figures 3.4 through 3.9 and 3.10 indicates a periodicity consistent with that of

the CIR's. Sector boundaries are seen to occur periodically with approximately the same period as that of the CIR's.

Smith and Wolfe *(1979)* have suggested that heliospheric sector boundaries and CIR's may be related through a simple process. The solar wind streams are thought to carry with them the magnetic field lines whose polarity is the same as that of the solar hemisphere of their origin. If the slower plasma originates from one solar hemisphere and the faster plasma originates from the opposite hemisphere, the interface between the plasma streams will involve magnetic fields of opposite polarity. The CIR(1,1), CIR(2,1), and CIR(3,1) features all contain a sector boundary change from a negative to a positive value (ie. λ_B switches from 90° to 270°). The second CIR does not exhibit a sector change within its leading and trailing edge. The recurrence of this sector change in the first CIR indicates that it is indeed the same feature, and cannot be related to the second CIR.

3.2.2 The Voyager 1 Solar Wind Data

Also available for analysis was the solar wind data as measured by the Voyager 1 spacecraft. Recall that the two Voyager spacecraft were very nearly radially aligned during this 80 day time interval and the maximum difference of their radial distances was only $\sim$ 0.45 astronomical units. Consequently, it is justifiable to neglect any corotation delay in the comparison of the Voyager 1 and Voyager 2 observations. The maximum value of the corotation delay, near the end of the time interval when the two spacecraft were separated by the maximum heliolongitude of $\sim 5°$, is only of the order of 9 hours.

Figures 3.11 through 3.13 indicate the value of the solar wind magnitude over

CIR	1	2	3	4	5	6
leading	112, 00*	128, 03*	139, 18	152, 02	161, 02	176, 18
trailing	117, 16	133, 00	145, 10	154, 18*	167, 00*	179, 03

Table 3.3: The Six CIR's as Detected by Voyager 1
The entries in this table represent the best estimate of the time of passage of the leading and trailing edge of the six presumed corotating interaction regions observed within the data interval of concern. The times indicated are DOY, hour. Entries marked with an asterisk indicate a data gap.

the same data interval of DOY 100–180, 1979 as recorded by Voyager 1. These diagrams can be directly compared to the top panel of Figures 3.4 to 3.9.

Careful examination of Figures 3.11 through 3.13 reveals the same six CIR's as are observed in the Voyager 2 profiles. In spite of the fact there was no field data available, a positive identification of the CIR's can be made. The Voyager 1 solar wind profiles are very nearly identical to those of Voyager 2, they only appear as time-shifted due to the larger heliocentric radial distance of Voyager 1. Table 3.3 lists the best estimate of the times of passage of the leading and trailing edges of the 6 CIR's. Again, an asterisk indicates the presence of a data gap at the presumed boundary. The estimated time was obtained by visual interpolation.

Table 3.4 displays the midpoint to midpoint period of the recurrence of the two CIR's. It can be directly compared to Table 3.2. The period of recurrence as observed by Voyager 1 is comparable to those observed by Voyager 2. Ideally, these periods would be the same if the spacecraft were *exactly* aligned radially and the CIR boundaries were smooth surfaces rather than corrugated surfaces.

It is also proposed by Smith and Wolfe *(1979)* that the width of a CIR should

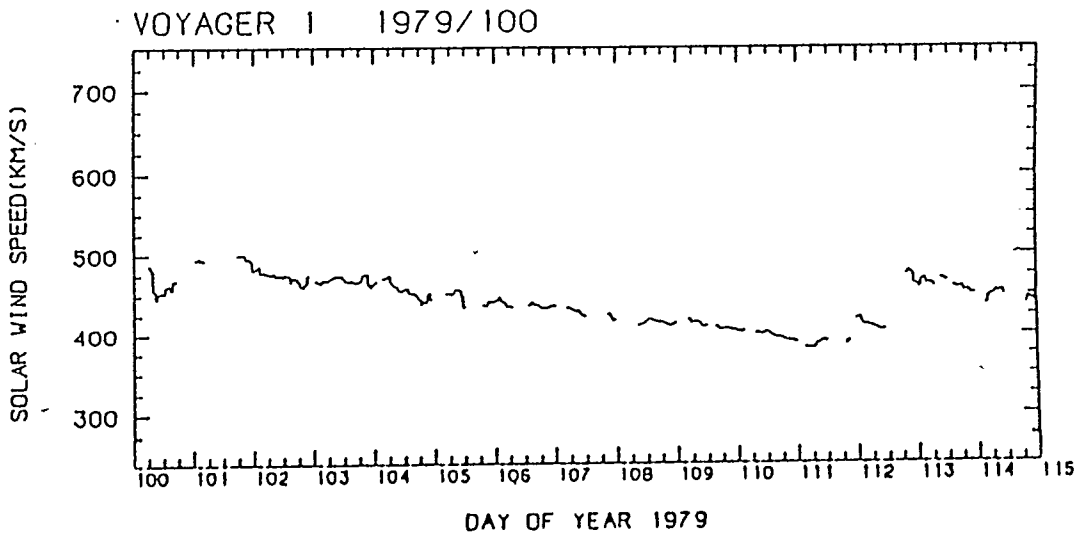

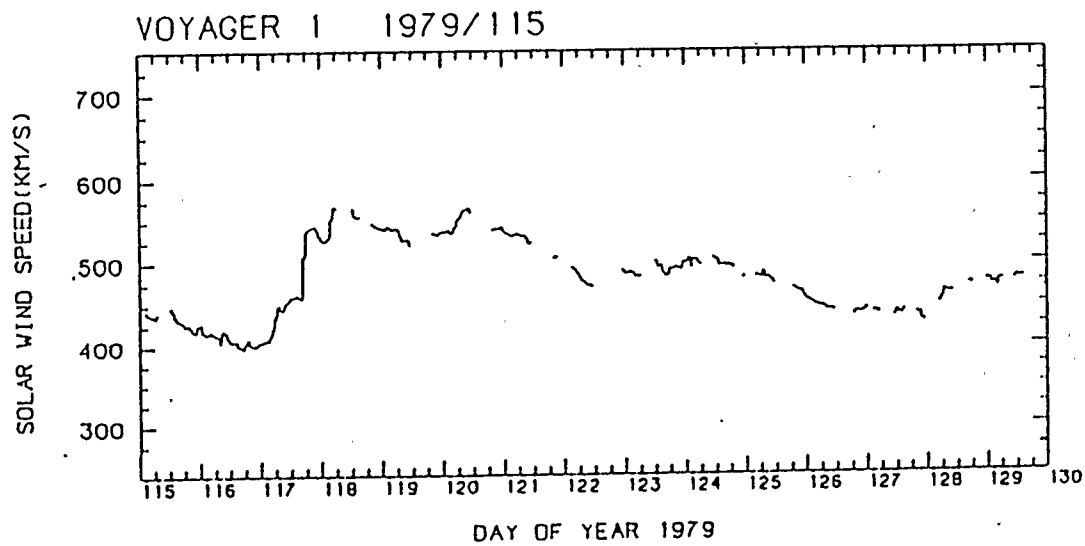

Figure 3.11: The Voyager 1 Data Set: DOY 100–130, 1979

Presented here is the solar wind magnitude as recorded by Voyager 1 from DOY 100–130, 1979.

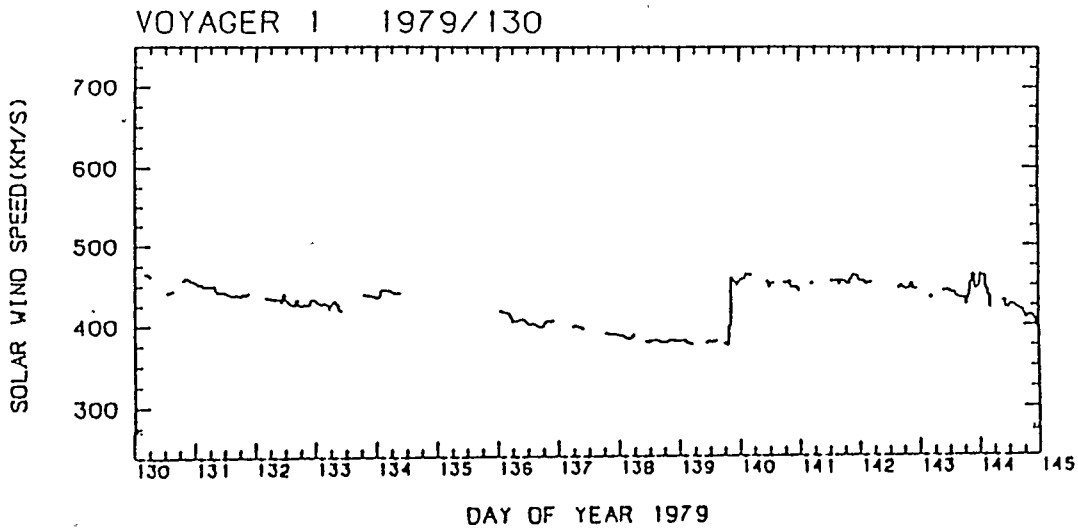

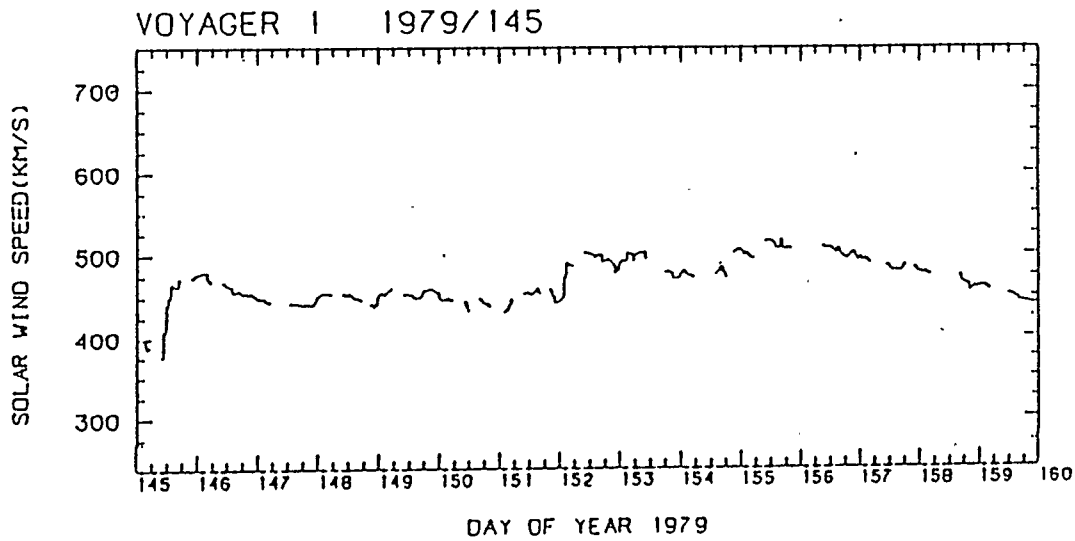

Figure 3.12: The Voyager 1 Data Set: DOY 130–160, 1979

Presented here is the solar wind magnitude as recorded by Voyager 1 from DOY 130–160, 1979.

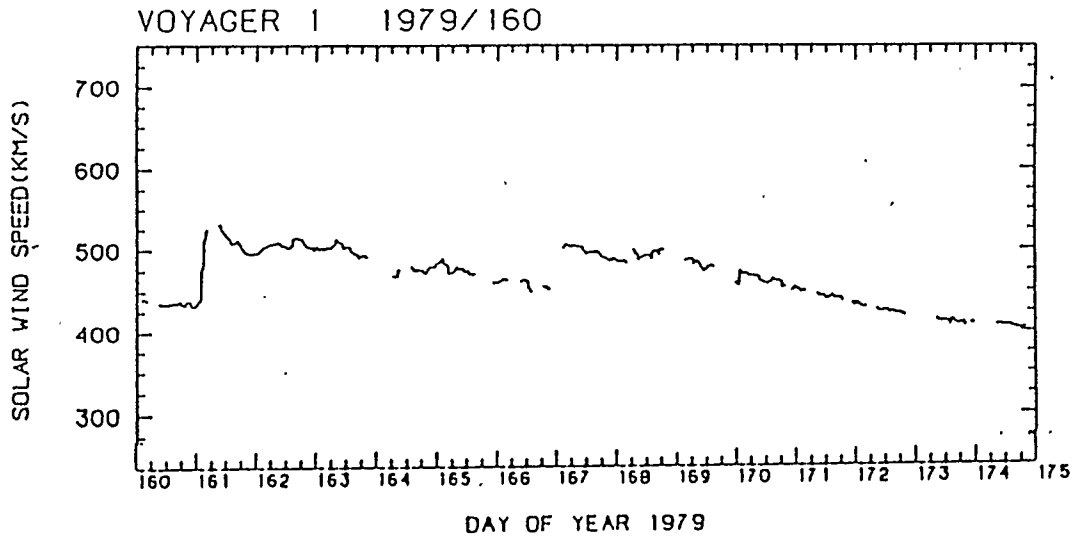

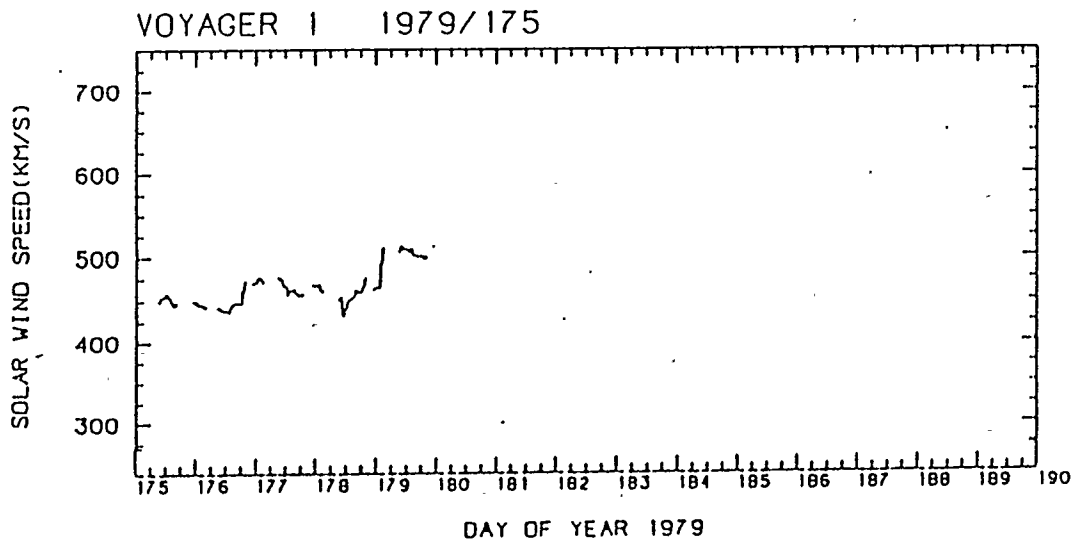

Figure 3.13: The Voyager 1 Data Set: DOY 160–190, 1979
Presented here is the solar wind magnitude as recorded by Voyager 1 from DOY 160–190, 1979.

CIR Pair	Period
CIR(1,1)-CIR(2,1)	27 days, 18 hrs
CIR(2,1)-CIR(3,1)	21 days, 11 hrs
CIR(1,2)-CIR(2,2)	22 days, 20 hrs
CIR(2,2)-CIR(3,2)	24 days, 12 hrs

Table 3.4: The Period of the Two Observed CIR's, Voyager 1
Shown is the time between successive passages of the three observed occurrences of the two CIR's as detected by Voyager 1.

increase with time at the average rate of 1 A.U. per day. Ideally then, an increase in the width of the two CIR's should be observed at Voyager 1. Table 3.5 presents the best estimate of the widths of the two CIR's as observed by both Voyager spacecraft.

Table 3.5 indicates that the three individual observations of the widths of the two CIR's are comparable for the two spacecraft. Also, the average value of the width of each CIR increased slightly as it propagated to the position of Voyager 1, consistent with Smith's observations based upon the Pioneer spacecraft data. Both spacecraft observed a decreasing width of the second CIR with each successive rotation. This could be due to the fact that this CIR is already beginning to dissipate. The forward shock may have already begun to decay into a large amplitude MHD wave.

3.2.3 The Variances of the IMF Vector, Voyager 2 Observations

The compression of the plasma and magnetic field within the corotating region is countered by the magnetic pressure within the CIR. Thus the variance of the

Event	Voyager 2	Voyager 1
CIR(1,1)	5.8 days*	5.7 days*
CIR(1,2)	5.1 days*	4.9 days*
CIR(2,1)	4.6 days	5.6 days
CIR(2,2)	3.0 days	2.7 days*
CIR(3,1)	6.0 days	5.9 days*
CIR(3,2)	1.8 days	2.3 days

Table 3.5: The Widths of the Two Observed CIR's

The widths of the CIR's as observed in each of the three occurrences by each spacecraft are comparable. The average width over the three observations of the two CIR's increased slightly from observations at Voyager 2 to Voyager 1. Entries marked with an asterisk are associated with data gaps, the resulting width is based upon the best estimate of the location of the leading and trailing boundaries.

magnetic field is expected to be greater within an interaction region than on either side of it *(Smith and Wolfe, 1979; Tsurutani et al., 1982)*.

Table 3.6 lists the average IMF variance, calculated from the one hour averaging of the data, in the thirteen distinct regions (or *time subintervals)* in the main data interval. These regions correspond to times prior to, during, and after each of the 6 observations of the CIR's; these appear as regions 2, 6, and 10 for the first CIR and regions 4, 8, and 12 for the second CIR.

Region	Variance (gamma^2)	Ratio
1	0.027	
		3.97 (2/1)
2 CIR(1,1)	0.106	
		2.69 (2/3)
3	0.039	
		2.33 (4/3)
4 CIR(1,2)	0.092	
		21.84 (4/5)
5	0.004	
		83.69 (6/5)
6 CIR(2,1)	0.351	
		16.00 (6/7)
7	0.022	
		10.64 (8/7)
8 CIR(2,2)	0.233	
		30.05 (8/9)
9	0.008	
		22.46 (10/9)
10 CIR(3,1)	0.174	
		8.23 (10/11)
11	0.021	
		42.12 (12/11)
12 CIR(3,2)	0.893	
		28.74 (12/13)
13	0.031	

Table 3.6: The Value of the Field Variance During the Data Interval
Regions 2, 4, 6, 8, 10, and 12 refer to the time intervals corresponding to the 3 occurrences of the two CIR's. Regions 1, 3, 5, 7, 9, 11, and 13 refer to the intervals prior, between, and after the CIR regions. The ratio of the CIR variance to that of the region on either side of it is shown, the variance within a CIR is constantly greater.

It is seen that the variance within a CIR is constantly greater than that of a surrounding region, by an order of magnitude in eight of the twelve possible ratios. This is in agreement with the results of the Pioneer data, lending support to the existence of regions 2,4,6,8,10, and 12 as CIR's.

3.2.4 Probability of Shock Existence

The previous subsections have provided convincing evidence for the recognition of two distinct corotating interaction regions observed by both Voyager spacecraft at a heliocentric radial distance of approximately 5 astronomical units. The purpose of this section is to discuss the existence of a forward and reverse shock associated with each of the two observed CIR's.

In general, the definite identification of a shock wave in the heliosphere requires a data set of much higher resolution than is presented in this study. The jump in the magnetic field data at a shock passage is of the order of 1 second *(Smith and Wolfe, 1976; Gazis and Lazarus, 1981; Tsurutani et al., 1982)*; abrupt jumps observed in the hourly averaged data may not necessarily be the result of true shocks.

An *undeniable* identification of a shock wave must involve analysis of a high time resolution data set consisting of field and plasma data. The vector magnetic field, plasma velocity, density, and temperature are all required. In most cases, as in the present case, this desirable combination is unfortunately not available and hence qualified assumptions necessarily have to be made.

Relatively low resolution data only was available for the present study. This consisted of the one hour averaged solar wind magnitude and magnetic field vector

data for Voyager 2 and the solar wind magnitude for Voyager 1 for the chosen time period of DOY 100–180, 1979. As pointed out earlier, although a definite identification of a shock wave is unfortunately not possible, use can however be made of previous statistical studies regarding the probability of CIR-shock associations at a given heliocentric radial distance.

Analysis of the Pioneer data at a heliocentric radial distance of 5 A.U. indicates that over 90% of all observed CIR's are accompanied by forward shocks, and only about 70% are accompanied by reverse shocks *(Smith and Wolfe, 1977)*. A similar study regarding Voyager 1 data over a distance from 4 to 6 A.U. also suggests that reverse shocks do not appear as frequently as forward shocks at a given radial distance possibly because it requires a larger velocity gradient to form a reverse shock *(Gazis and Lazarus, 1981)*. There is also evidence from two-spacecraft studies that reverse shocks tend to decay earlier than forward shocks, as a result they appear more infrequently at larger helioradial distances.

Hence from the Voyager spacecraft profiles, combined with the probability inferences from other studies, it is concluded the two observed CIR's have associated forward shocks at their leading edges and to a lesser degree of confidence, reverse shocks at their trailing edges. The best-estimate times of passage of these shocks as observed by the Voyager 2 and 1 spacecraft are listed in Tables 3.1 and 3.3. Further analysis can now be carried out upon the specific shock geometry. The next section presents the results of the shock normal angle determination.

	F1		R1		F2		R2	
occurrence	χ	θ_{Bn}	χ	θ_{Bn}	χ	θ_{Bn}	χ	θ_{Bn}
first	28.0	112.3 ±19.8	13.2	91.3 ±0.3	43.7	99.9 ±0.1	28.5	92.3 ±2.8
second	9.6	93.7 ±10.0	37.1	120.9 ±30.4	105.3	138.2 ±30.1	21.1	106.6 ±21.1
third	33.0	90.3 ±0.2	43.0	108.1 ±8.8	86.1	127.7 ±14.3	27.8	85.9 ±55.2

Table 3.7: Average Field Values and 4 Hour Averaging Period
This table shows the values of the shock normal angles and χ, the angle between $\vec{B}_1$ and $\vec{B}_2$ for the three recurrences of the two shock pairs. This table is from the average field values and a four hour up and downstream averaging period. The entries are in degrees.

3.3 Shock Normal Determinations

As a consequence of having only the Voyager 2 magnetic field vector data for the chosen data analysis period, it was necessary that the magnetic coplanarity method was used in the determination of the angle θ_{Bn}. The shock angle was derived using the magnetic coplanarity equation, 2.12, for each of the three occurrences of the two shock pairs, where possible. The values of $\vec{B}_1$ and $\vec{B}_2$ appearing in the magnetic coplanarity equation actually refer to the average upstream and downstream magnetic field data. However, the analysis was also performed using the median values of the field parameters as suggested by Abraham-Shrauner and Yun which are claimed to be better estimates in cases where some data points differ significantly from the rest, thus biasing the average value *(1976)*.

The median and average values of $\vec{B}_1$ and $\vec{B}_2$ were calculated from 24 and 4

	F1		R1		F2		R2	
occurrence	χ	θ_{Bn}	χ	θ_{Bn}	χ	θ_{Bn}	χ	θ_{Bn}
first	19.6	101.9 ±12.2	14.7	91.8 ±0.5	48.1	101.5 ±2.6	20.5	91.3 ±1.6
second	14.2	95.4 ±10.6	62.1	100.9 ±7.9	101.3	135.3 ±24.9	22.2	108.2 ±22.8
third	14.1	90.5 ±0.2	40.2	106.2 ±8.1	66.3	82.4 ±43.6	35.9	---- ----

Table 3.8: Median Field Values and 4 Hour Averaging Period
This table shows the values of the shock normal angles and χ, the angle between $\vec{B}_1$ and $\vec{B}_2$ for the three recurrences of the two shock pairs. This table is from the median field values and a four hour up and downstream averaging period. The entries are in degrees.

hour periods up and downstream of each shock in the eighty day analysis period. The two time periods were chosen such that the advantages of one would offset the disadvantages of the other. Note that the 24 hour averaging period may include large fluctuations which significantly affect the result, whereas the 4 hour averaging period may be considered statistically insignificant.

The uncertainty in the value of the calculated shock angle was determined from the variance in the components of the up and downstream magnetic field vectors. An approximation was used at this point, it was assumed that each component of the magnetic field was Gaussian in nature as adapted by Chao and Chen *(1985)*. It was also assumed that the variance in each component was equal, each being equal to one third of that of the total directional field variance given by the square of equation 3.1.

The shock normals for the data set are summarized in Tables 3.7, 3.8 , 3.9

	F1		R1		F2		R2	
occurrence	χ	θ_{Bn}	χ	θ_{Bn}	χ	θ_{Bn}	χ	θ_{Bn}
first	13.4	94.1 ±4.1	12.2	89.4 ±5.6	42.3	103.1 ±3.9	69.3	95.7 ±5.7
second	10.9	87.0 ±11.8	63.0	87.2 ±8.3	53.5	135.4 ±13.8	39.2	101.0 ±11.0
third	100.9	101.9 ±6.9	34.6	116.5 ±18.9	166.4	---- ----	26.3	---- ----

Table 3.9: Average Field Values and 24 Hour Averaging Period
This table shows the values of the shock normal angles and χ, the angle between $\vec{B}_1$ and $\vec{B}_2$ for the three recurrences of the two shock pairs. Note, the entry for the event F(2,1) was calculated over a 7 hour averaging period to avoid the sector boundary downstream. This table is otherwise from the average field values and a twenty-four hour up and downstream averaging period. The entries are in degrees.

and 3.10. Note that the entries for events F(2,1) and F(3,2) in Tables 3.9 and 3.10 are calculated from an up and downstream averaging period of 7 hours rather than 24 hours in an attempt to avoid the obvious difficulty of the sector boundaries that exist at least 7 hours downstream of the forward shocks. It is noted immediately that there is not usually a large difference in the values as calculated by the methods using the median and average values of the up and downstream field parameters.

In some cases the results given by the 4 hour averaging period appear to be better than those given by the 24 hour averaging period. It should also be noted that there is generally a positive correlation between the uncertainty in the value of θ_{Bn} and the variances in the upstream (σ_1^2) and downstream (σ_2^2) field variances over the averaging interval, as expected. The values of the upstream and downstream field variances are tabulated in Tables 3.11 and 3.12. The blank entries in the R(3,2)

	F1		R1		F2		R2	
occurrence	χ	θ_{Bn}	χ	θ_{Bn}	χ	θ_{Bn}	χ	θ_{Bn}
first	9.9	92.2 ±2.4	5.2	88.8 ±3.7	51.6	112.6 ±7.3	72.3	95.4 ±5.3
second	16.6	74.3 ±20.1	78.8	81.1 ±18.6	44.7	123.6 ±7.3	36.5	101.2 ±12.3
third	95.1	97.0 ±17.4	34.8	120.9 ±23.4	166.5	---- ----	31.8	---- ----

Table 3.10: Median Field Values and 24 Hour Averaging Period
This table shows the values of the shock normal angles and χ, the angle between $\vec{B}_1$ and $\vec{B}_2$ for the three recurrences of the two shock pairs. Note, the entry for the event F(2,1) was calculated over a 7 hour averaging period to avoid the sector boundary downstream. This table is otherwise from the median field values and a twenty-four hour up and downstream averaging period. The entries are in degrees.

event in Table 3.8 and in the F(3,2) and R(3,2) events in Tables 3.9 and 3.10 reflect the difficulty in evaluating the shock geometries for these events due to the large field variances present.

As previously mentioned, the magnetic coplanarity method is not the optimum method in general for finding θ_{Bn}. However, it is the only method available when only the magnetic field data is present. The validity of the values tabulated in Tables 3.7, 3.8, 3.9 and 3.10 can be checked in a qualitative manner.

The *garden hose* angle of the mean interplanetary magnetic field at a radial distance of 4 to 6 A.U.'s from the sun, as given by the Parker model, is approximately 75° to 81° for an average solar wind speed of 400 km/s. For a shock propagating along its normal in an approximate radial direction, its shock angle should be near 90°. That is, under the specified assumption, it is expected that perpendicular

	F1		R1		F2		R2	
occurrence	σ_1^2	σ_2^2	σ_1^2	σ_2^2	σ_1^2	σ_2^2	σ_1^2	σ_2^2
first	0.075	0.020	0.013	0.089	0.091	0.133	0.022	0.104
second	0.119	0.910	0.082	0.211	0.178	1.092	0.122	0.221
third	0.186	1.218	0.139	0.288	0.380	2.616	0.262	0.426

Table 3.11: Field Variances: 4 Hour Averaging Period
Upstream and downstream values of the field variances for a 4 hour averaging period. The entries are in (gamma)^2.

	F1		R1		F2		R2	
occurrence	σ_1^2	σ_2^2	σ_1^2	σ_2^2	σ_1^2	σ_2^2	σ_1^2	σ_2^2
first	0.016	0.068	0.052	0.100	0.030	0.156	0.058	0.082
second	0.109	1.523	0.073	0.245	0.066	0.744	0.093	0.345
third	0.072	0.888	0.104	0.439	0.379	3.938	0.445	1.623

Table 3.12: Field Variances: 24 Hour Averaging Period
Upstream and downstream values of the field variances for a 24 hour averaging period. Note, the entries for the events F(2,1) and F(3,2) were calculated over a 7 hour averaging period to avoid the sector boundary downstream. The entries are in (gamma)^2.

shocks exist at this radial distance. It is already stated that for perpendicular shocks the difference in the direction of the magnetic field across the shock is minimal, and we should expect that the angle between the up and downstream field vectors, χ, is small. Alternatively, it is equivalent to say that the value of $\Delta\vec{B}$ in Figure 2.1 is very small. Therefore to have full confidence in a value of θ_{Bn} in either of the tables the analysis must satisfy two conditions: the value of χ must be *relatively* small and the variances in the up and downstream average fields must be *relatively* small.

The first condition can be observed directly in Figures 3.4 to 3.9. In general, there is little change in the direction of the magnetic field across the shocks as indicated by the values of λ_B and δ_B. The magnetic Rankine-Hugoniot conditions discussed in chapter 2 indicate that there should be little change in the direction of the magnetic field at a perpendicular shock. The field is increased in intensity but there is no refraction of the field lines. This is observed in the Voyager 2 field data.

Chapter 4

LOW ENERGY CHARGED PARTICLE ENHANCEMENTS

4.1 Particle Enhancements

Prior to the *in situ* observations of particle enhancements resulting from acceleration at shock waves in the heliosphere, only theoretical treatments of the problem were possible. However, the deployment of earth-orbiting experiments and interplanetary spacecraft has provided the first opportunity to test and verify, and modify where necessary, the existing theories.

Many review articles and papers have been published in the last decade which summarize the theoretical expectations and/or experimental observations of particle enhancements at shocks waves, both in the heliosphere and in extra-galactic locales such as supernovae. These studies can be broadly classified into two categories according to which acceleration theory, either SDA or Fermi acceleration, is predominantly dealt with.

Table 4.1 is an attempt to indicate this. Shown is a cross-section of review articles and research papers which investigate the acceleration of charged particles via the shock drift or Fermi acceleration mechanisms from either a theoretical or observational viewpoint. The table is presented merely to demonstrate the common viewpoints used in the study of particle acceleration. Generally, there is not

	SDA	Fermi	Both
Observational	Smith, 1979 (r) McDonald, 1981*	McDonald, 1976* Richardson,1985* Richter, 1984 (r) Sanderson, 1985*	Tsurutani, 1982 Ng, 1985 Tan, 1986* Krimigis, 1987 (r) Krimigis, 1988(r)
Theoretical	Armstrong, 1985 (r) Decker, 1985	Bell, 1978 (r) Blandford, 1979 (r) Toptyghin, 1980 (r) Peacock, 1981 (r) Lee, 1982 (r) Decker, 1986b	Armstrong, 1977 (r) Axford, 1981 (r) Pesses, 1982 (r) Forman, 1985 (r) Decker, 1986a Decker, 1988 (r)

Table 4.1: Selected Literature Regarding Particle Acceleration

The entries in this table are a representative fraction of the work concerned with particle acceleration at shock waves. It is not a comprehensive list, but indicates the various approaches used in the study of particle acceleration. More recent efforts concentrate on both the SDA and Fermi mechanisms, rather than one or the other. Entries marked with a (r) indicate a review article, those with a * indicate that a specific mechanism was not explicitly mentioned in the article but was instead inferred.

a strict division between the two mechanisms and Table 4.1 indicates that the latest research efforts realize the importance of both processes. Not only is it now recognized that interior shocks (~2 A.U. or less) are usually, but not exclusively, associated with parallel shocks and the Fermi mechanism, and shocks observed at a further helioradial distance are mainly associated with quasi-perpendicular shocks and the SDA mechanism, the importance of both mechanisms acting simultaneously at the same shock is now being recognized. The modeling done by Decker *(1988)* has indicated how the diffusive mechanism can aid the SDA mechanism by allowing a longer particle-shock interaction time resulting in higher energy gains through the drift process.

Regardless of which acceleration process(es) is (are) considered predominant, the enhancement of charged particle intensities produced by shock waves in the heliosphere can be classified into 3 types *(Pesses et al., 1982; Armstrong et al., 1977)*: energetic storm particle events, shock spike events, and corotating particle events. Although it is the corotating particle events which are of immediate importance in the present study, in correspondence with the plasma and field data presented in chapter 3, it is instructive to briefly mention the other two types of particle enhancements. It is seen that each type of particle event is distinctive and yet all three share important characteristics.

Energetic storm particle events are the enhancements observed as a result of the shock wave of a solar flare. This type of event is generally observed during the long decay phase of observed solar flare ion events. It is the lower-energy ion population which is generally affected by this type of event, typically in the range 0.1–10.0 MeV per nucleon *(Decker, 1981)*. The relative intensity enhancement increases for

decreasing particle energies. The time width of an energetic storm particle event averages approximately 4 to 8 hours. The intensity-time profile appears in the data as a slow pre-shock rise to a maximum, which is sometimes observed at a point a few hours before the actual shock passage, followed by a sudden decrease.

Shock spike events are those enhancements observed near 1 A.U. that are associated with either a solar flare-produced or corotating shock and which are not observed during the solar ion decay phase. The time duration of a shock spike event is significantly narrower than that of an energetic storm particle event, being of the order of one-half to 3 hours. Shock spike events are specifically dealt with in the review by Armstrong et al., *(1977)*.

Corotating particle events are those associated with the forward and reverse shock waves bounding the stream-stream interaction region, as shown in Figure 3.3. The presentation of the particle enhancements associated with the data set introduced in chapter 3 will be delayed until after the next section where the Voyager instrumentation will be discussed.

It is noted *(Pesses et al., 1982)* that there are four features common to all three types of particle enhancements:

- particle flow anisotropies in the vicinity of the shock,
- particle intensity enhancements as a function of θ_{Bn},
- lack of electron events at higher energies,
- and the absence of enhancements associated with slowmode shocks.

The latter two points are not of immediate interest to the present study, the

second point was mentioned in the second chapter and the first point is the subject of chapter 5. For the first time, the Voyager low energy charged particle data will be examined in the vicinity of a shock at a radial distance of ~5 A.U. to see if an anisotropic particle flow exists in the plasma frame in an anti-shockward direction.

4.2 The Voyager LECP Detector

It was recognized in the early 1970's that there would exist before the end of that decade an optimum configuration of the exterior planets that would aid a spacecraft in having a trajectory suitable for close inspection of the Jovian and Saturnian planetary systems, with a further possibility of a Uranian and/or Neptunian encounter. Thus, the *Mariner-Jupiter-Saturn* spacecraft project, later renamed the Voyager Mission, was developed. The primary initial mission objectives included the "exploratory investigations of the Jupiter and Saturn planetary systems and of the interplanetary medium from Earth to Saturn" *(Kohlhase and Penzo, 1977)*. A special issue of the Space Science Reviews *(Sp. Sci. Rev.,* **21**, *1977)* was dedicated specifically to the Voyager project.

The Mission, managed by the Jet Propulsion Laboratory, involved 100 scientists from 38 different institutions. Aboard each of the two planned spacecraft were to be eleven separate scientific investigations. The experiment which provided the particle data to be presented in this chapter was the Low Energy Charged Particle (LECP) experiment.

This was provided to the Voyager Mission by The Johns Hopkins University Applied Physics Laboratory (JHU/APL); the Principle Investigator was Dr. S.M.

Krimigis. Aside from the detailed investigation of the charged particle composition within the magnetospheres of the exterior planets, it was expected that the following very important interplanetary observations would be made *(Krimigis et al.,1977)*:

- The low energy spectra and composition of the galactic cosmic radiation,
- the time variations of the galactic cosmic rays,
- the radial gradient of the galactic cosmic rays,
- the observation of energetic particles of solar flare origin,
- the observation of energetic particles of planetary origin,
- the observation of energetic particles associated with corotating shock pairs,
- and the anisotropy of energetic particles in the vicinity of interplanetary shocks.

A technical description of the LECP is given by Peletier et al., *(1977)* and Krimigis et al., *(1977)*, but here a brief description is given for the sake of completeness. The LECP detector system consists of two subsystems, the Low Energy Magnetospheric Particle Analyzer (LEMPA) and the Low Energy Particle Telescope (LEPT).

The LEPT has the ability to measure the major ion species at energies above 200 keV per nucleon. Data from the LEPT was not used in this study. A detailed description of the $\frac{dE}{dx} \times E$ detector elements of the LEPT are given in Krimigis et al., *(1977)*.

LECP Channel	Lower Passband (keV)	Upper Passband (keV)
PL01	28.0	43.0
PL02	43.0	80.0
PL03	80.0	137.0
PL04	137.0	215.0
PL05	215.0	540.0
PL06	540.0	990.0
PL07	990.0	2140.0
PL08	2140.0	3500.0

Table 4.2: The Voyager 2 PL0 Channel Energy Passbands
The actual energy passbands of the PL0 channels of the Voyager 2 LECP experiment are indicated. These energies refer to the passbands for protons.

The LEMPA measures total kinetic energies in the ~30 keV to ~4 Mev per ion range, without the ability to identify the particle species. The LEMPA actually consists of seven particle detection systems, one of which has provided the particle data to be presented in the next section. Detector alpha is the primary detector used for the measurement of low energy protons or ions. The energies of the detected particles are binned into eight logarithmically spaced energy channels, designated as PL01 to PL08. The actual passbands of each channel are functions of particle species *(Decker et al., 1981)*. Table 4.2 lists the passbands for the PL0 channels corresponding to the detection of protons for Voyager 2.

Because of the fact that the Voyager spacecraft are not spin-stabilized vehicles it was necessary to mount both the LEPT and the LEMPA on a rotating platform in order to obtain angular information about the particle distributions. The platform is stepped sequentially through eight 45° sectors; the stepping rate being either

one revolution per 48 minutes in *cruise mode* (6 stationary minutes per sector) or one revolution per 48 seconds in *planetary encounter mode* (6 stationary seconds per sector). The stepping sequence proceeds through the sectors in the following order: ...8-7-6-5-4-3-2-1-1-2-3-4-5-6-7-8-8-7-..., a cable preventing the continuous rotation of the platform. A combination calibration target/sun shield was in place over sector 8 in order to prevent interference from solar illumination *(Decker et al., 1981)*.

4.3 The PL0 Channels' Particle Data

The data is obtained from the spacecraft as a count rate; that is, for a particular energy range (ie., PL0 channel) the number of particles per time interval. These count rates are presented as intensity versus time profiles in Figures 4.1 and 4.2. Unfortunately, the lowest energy channel of detector alpha aboard Voyager 2, PL01, was inoperable during the data interval of concern. Also included in the figures are the IMF and solar wind magnitude profiles as well as the time of passage of the suspected forward and reverse shock pairs as discussed in chapter 3. The compression of the time scale in comparison to the figures presented in chapter 3 aids in effectively observing the consequence of the shocks upon the profiles of the IMF and the solar wind as well as the particle intensities. All values represent hourly spin-averaged data and data gaps fortunately appear infrequently.

The correlation between the passage of a corotating shock and a rise in the observed particle intensity is evidence that particle acceleration is occurring at these times. This rise in particle intensity provides evidence that the observed

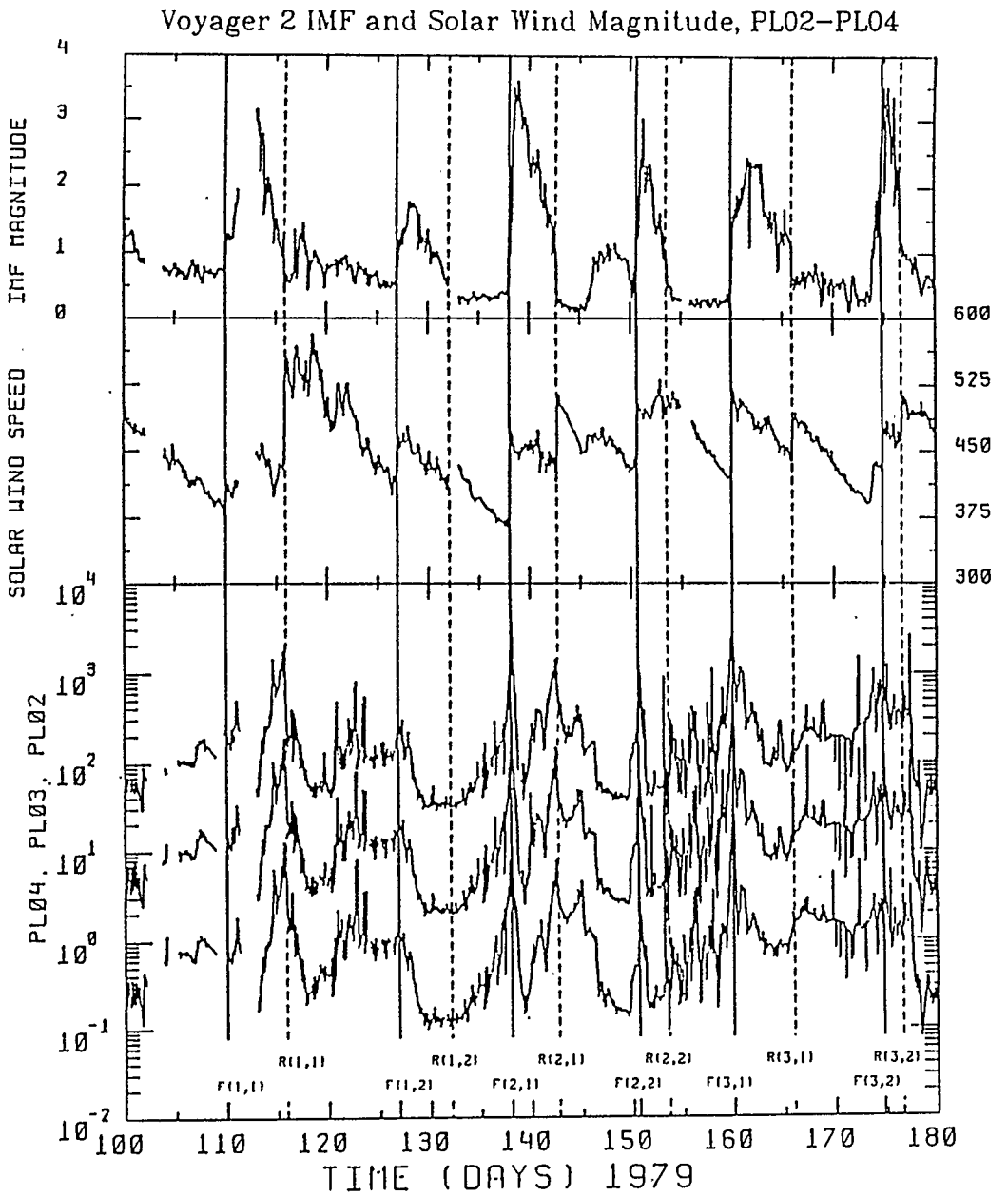

Figure 4.1: The Voyager 2 PL0 Count Rates: PL02–PL04

Indicated in the figure are the hourly spin-averaged count rates of the Voyager 2 PL02–PL04 channels. Also indicated are the IMF and solar wind magnitude profiles as well as the times of passage of the two corotating shock pairs. Evident at every shock passage, excepting F(1,1) where a data gap exists, is the associated enhancement of the particle intensity at each of the indicated energy intervals. The forward shocks are indicated by the solid lines, the reverse shocks by the dashed. The solar wind speed is given in km/h, and the IMF magnitude in gamma's.

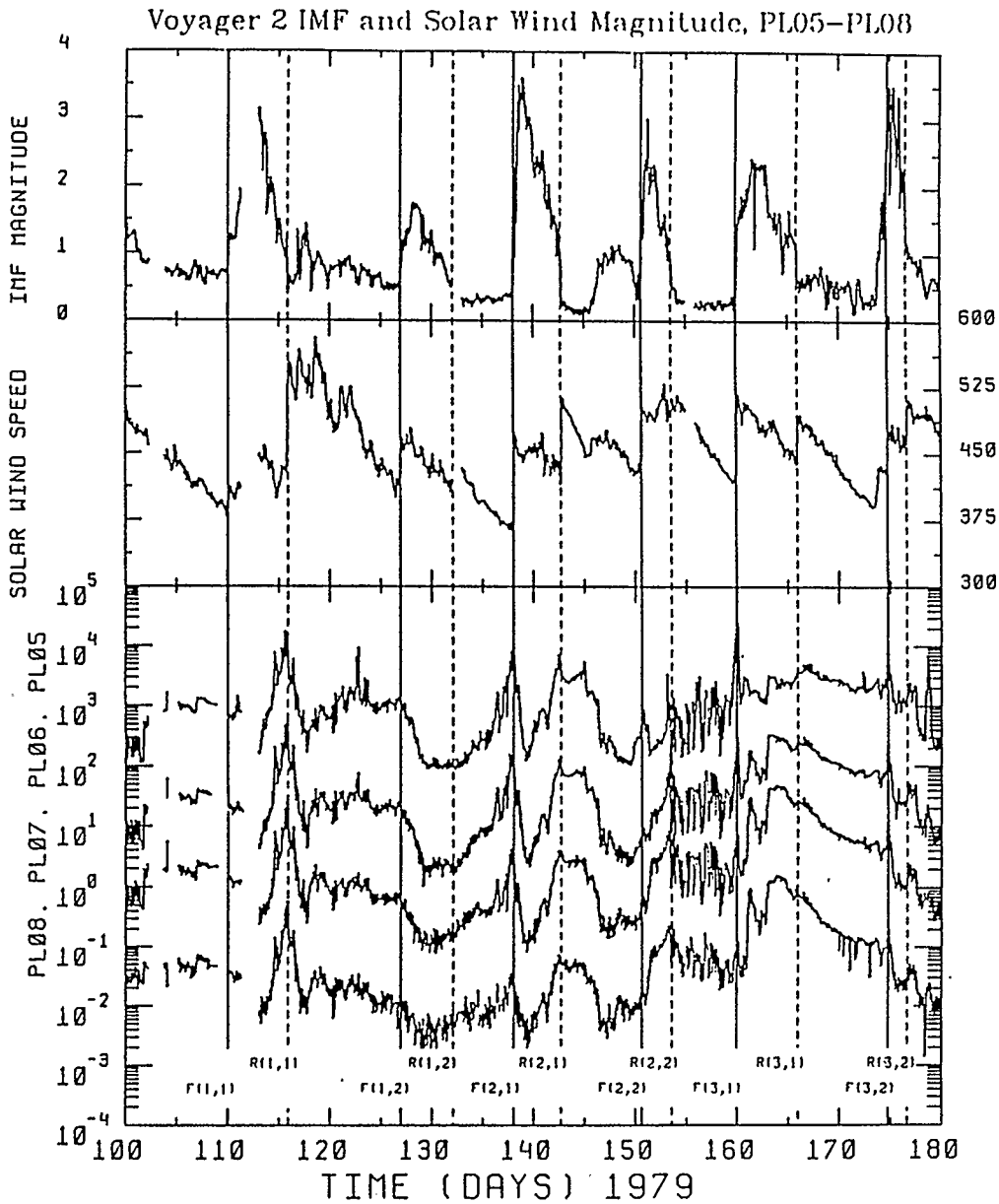

Figure 4.2: The Voyager 2 PL0 Count Rates: PL05–PL08

Indicated in the figure are the hourly averaged count rates of the Voyager 2 PL05–PL08 channels. Also indicated are the IMF and solar wind magnitude profiles as well as the times of passage of the two corotating shock pairs. Evident at every shock passage, excepting F(1,1) where a data gap exists, is the associated enhancement of the particle intensity at each of the indicated energy intervals. The forward shocks are indicated by the solid lines, the reverse shocks by the dashed. The solar wind speed is given in km/h, and the IMF magnitude in gamma's.

plasma disturbances are in fact shock waves, supporting the conclusions in chapter 3. The particle enhancement at the location of F(1,1) is not directly observed in the figures, there being a data gap at that time interval.

Two incidental features are also to be pointed out in the particle intensity data in Figures 4.1 and 4.2. The first is an indication of an acceleration process at approximately DOY 145. There is an associated jump in the magnitudes of both the the IMF and the solar wind data as well as in all energy channels. The enhancement in the lower energy channels is slightly larger indicating the acceleration was more efficient at the lower energies. If this is the result of the passage of a shock wave, the shock cannot be related to either of the recognized two shock pairs. There is no recurrence of this feature in the 80 day data interval. Secondly, the large particle enhancement observed in the higher energy PL0 channels at approximately DOY 163 is likely due to a solar flare ion event *(Decker, 1981)*.

4.4 The Energy Spectra

One of the mission objectives of the LECP detector was the observation of the *energy spectra* of the low energy charged particles in the interplanetary space. The energy spectrum describes the flux of the observed charged particles as a function of their energy. This section first discusses the techniques used in the determination of the particle fluxes from the observed count rates and then presents the evolution of the LECP energy spectra over the data interval.

4.4.1 The Determination of the Particle Flux

The particle flux observed by a detector is defined as the number of particles observed per area per solid angle per time per energy. If j is the flux quantity, then:

$$j = \frac{\Delta N}{\Delta A \Delta \Omega \Delta t \Delta E} \tag{4.1}$$

where ΔN is the observed number of particles per area of detector ΔA, per solid angle $\Delta\Omega$, in the time interval Δt in the energy interval ΔE. The two factors ΔA and $\Delta\Omega$ are physical features of the detector itself. The *geometrical factor* of the detector, g, is defined to be the integration over the detector area and solid angle *(Kessel, 1986)*:

$$g = \int dA d\Omega \tag{4.2}$$

Rearranging equation 4.1, the relationship between the count rate, R, (number of particles observed per time) and the flux (number of particles per geometrical factor per energy per time) is found:

$$R \equiv \frac{\int dN}{\Delta t} = g \int_{E_l}^{E_u} j dE \tag{4.3}$$

where the limits of integration refer to the lower and upper passbands of the detector.

The functional form of the flux quantity j, as a function of the energy E, for galactic cosmic rays is generally assumed to be a power law *(Pomerantz, 1971)* with a spectral index γ:

$$j(E) = j_\circ \left(\frac{E}{E_\circ}\right)^{-\gamma} \tag{4.4}$$

where,

$$j(E_\circ) = j_\circ \tag{4.5}$$

Substituting equation 4.4 into equation 4.3 and rearranging slightly:

$$R = g j_\circ E_\circ^\gamma \int_{E_l}^{E_u} E^{-\gamma} dE \tag{4.6}$$

There are two possible solutions to this integral. The first solution is for $\gamma \neq 1$:

$$R_i = g_i j_\circ \frac{E_\circ^\gamma}{1-\gamma} \left[E_{ui}^{1-\gamma} - E_{li}^{1-\gamma}\right] \tag{4.7}$$

The second solution is for $\gamma = 1$:

$$R_i = g_i j_\circ E_\circ^\gamma \ln\left(\frac{E_{ui}}{E_{li}}\right) \tag{4.8}$$

In equations 4.7 and 4.8, the subscript i has been added in reference to a particular energy channel. Channel i has a count rate of R_i, lower passband energy of E_{li}, an upper passband energy of E_{ui}, and is located within detector whose geometrical detector is g_i.

If channel j is the next higher energy channel of the detector, then an identical set of equations exists for this channel. If ρ_{ij} is defined at this point to be the ratio of the count rates of channels i and j, then the two cases depending upon the value of γ become:

$$\rho_{ij} \equiv \left(\frac{R_i}{R_j}\right) = \left[\frac{E_{ui}^{1-\gamma_{ij}} - E_{li}^{1-\gamma_{ij}}}{E_{uj}^{1-\gamma_{ij}} - E_{lj}^{1-\gamma_{ij}}}\right] \tag{4.9}$$

for $\gamma_{ij} \neq 1$, and:

$$\rho_{ij} \equiv \left(\frac{R_i}{R_j}\right) = \left[\frac{\ln\left(\frac{E_{ui}}{E_{li}}\right)}{\ln\left(\frac{E_{uj}}{E_{lj}}\right)}\right] \tag{4.10}$$

for $\gamma_{ij} = 1$, where γ_{ij} is the value of the spectral index at the energy of the common passband of the two channels i and j.

The fact that the two channels are within the same detector, and thus share the same geometrical factor, has been used in the above two equations by setting the ratio g_i/g_j to unity. More notational simplifications can be made by realizing that channel i and channel j share a common passband: $E_{ui} = E_{lj}$. Let $E_1 = E_{li}, E_2 = E_{ui} = E_{lj}, E_3 = E_{uj} = E_{lk}$, etc. for consecutive energy channels $i, j, k, \ldots$. Also let $\varsigma \equiv (E_2/E_1)$ and $\eta \equiv (E_3/E_2)$ and $\mu \equiv (\gamma_{ij} - 1)$, then equations 4.9 and 4.10 simplify to:

$$\rho_{ij} = \frac{(\varsigma^{\mu} - 1)}{(1 - \eta^{-\mu})} \tag{4.11}$$

for $\gamma_{ij} \neq 1$, and:

$$\rho_{ij} = \frac{\ln \varsigma}{\ln \eta} \tag{4.12}$$

for $\gamma_{ij} = 1$.

The appropriate equation, either 4.11 or 4.12, can be solved iteratively by Newton's method for each ratio of consecutive channels. That is, for a function of μ ($\equiv \gamma_{ij} - 1$), $f(\mu) = 0$, the $(n+1)^{th}$ approximation to the value of μ is given by:

$$\mu_{n+1} = \mu_n - f(\mu_n)/f'(\mu_n)$$

where $f'(\mu_n)$ is the derivative of $f(\mu)$ with respect to μ, evaluated at the nth value of μ.

By this method, seven values of γ_{ij} were calculated from the ratio of the 8 Voyager 2 PL0 channels. This method calculates the value of the spectral index at the common energy passband of the PL0 channels. What is really desired is the value of the spectral index *within* each of the eight energy bins. With this value of γ, the resultant flux can be calculated by equation 4.7 or 4.8.

Figure 4.3 indicates schematically the energy passbands of the PL0 channels as well as the logarithmic mean energy of each channel. The lower energy passband of PL01 is 28 keV and is denoted by E_1. The upper energy passband of PL01 (43 keV) equals the lower energy passband of PL02 and is denoted E_2. The logarithmic mean energy of PL01 is denoted by $\tilde{E}_1$ and is seen to be 37 keV. In a similar fashion, the other energy channels are indicated. The value of the spectral index at a common energy passband is denoted by a double-subscripted γ, the value at a logarithmic mean energy of a passband is denoted by a single-subscripted γ. The value of the logarithmic mean energy spectral index is calculated from the values of the adjacent double-subscripted γ's.

This can be accomplished by performing a parabolic fit to the energy spectrum by adding a quadratic term in the logarithm of the energy to the logarithm of equation 4.4. For example, to find the spectral index in the middle of the PL02 channel, γ_2 at the energy $\tilde{E}_2$ (the logarithmic mean of E_2 and E_3, $\tilde{E}_2 = (E_2E_3)^{1/2}$),

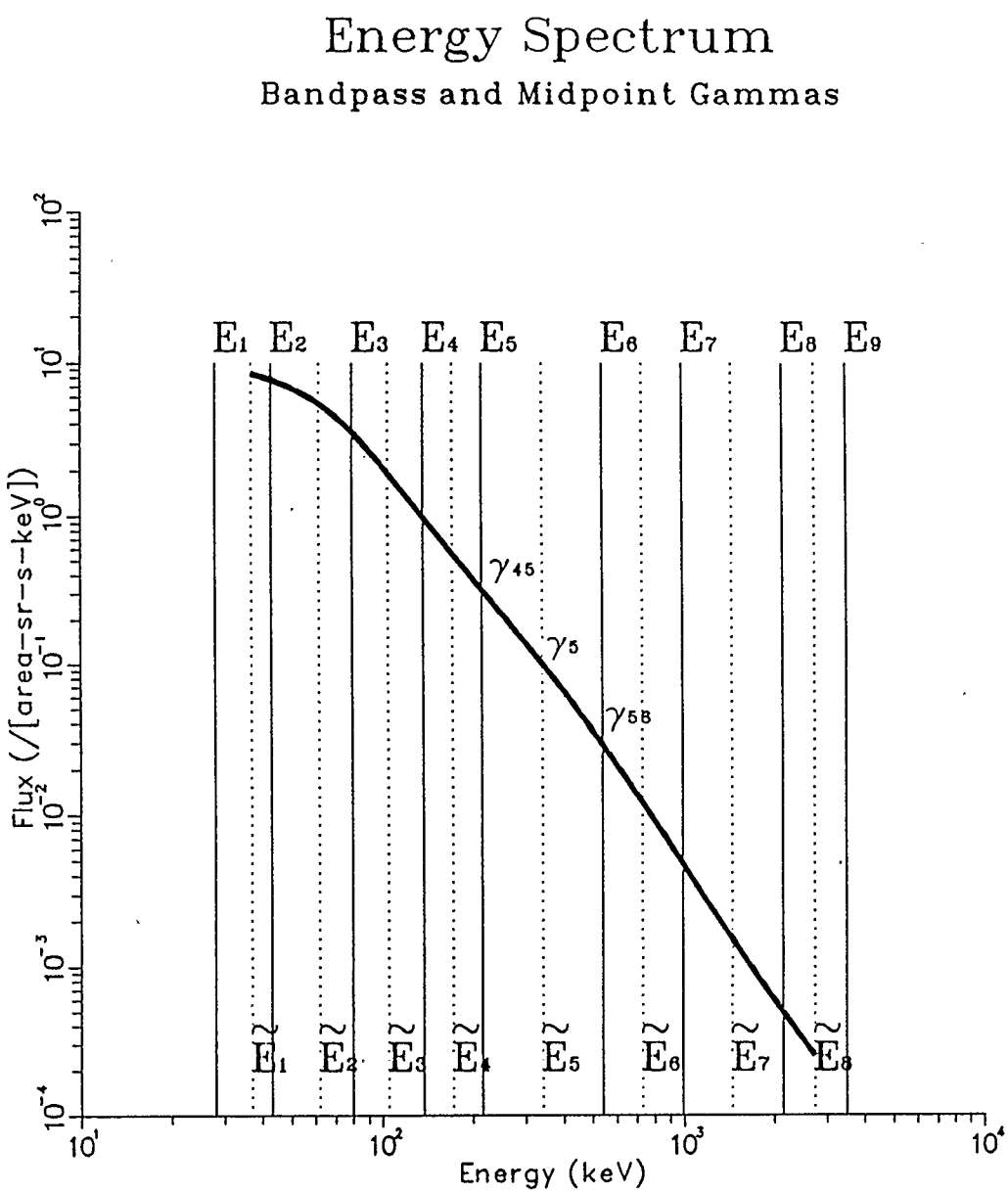

Figure 4.3: The Sample PL0 Energy Spectrum

Indicated in this diagram are the passband energy locations as well as the locations of the logarithmic mean energy values in each of the eight PL0 channels. For example, the value of the spectral index, γ, (equivalently the slope of the log-log plot) is shown at three different locations: the value of γ at the common energy passband of PL04 and PL05 is denoted γ_{45}, that at the common energy passband of PL05 and PL06 is γ_{56}. The value of γ at the logarithmic mean energy of PL05 is γ_5.

begin by taking the logarithm of 4.4 evaluated at $\widetilde{E}_2$ with $E_\circ \equiv E_2$:

$$\ln j(\widetilde{E}_2) = \ln j(E_2) - \gamma_{12}(E_2) \ln\left(\frac{\widetilde{E}_2}{E_2}\right) \tag{4.13}$$

Adding to equation 4.13 a term in $\left[\ln\left(\frac{\widetilde{E}_2}{E_2}\right)\right]^2$,

$$\begin{aligned} \ln j(\widetilde{E}_2) &= \ln j(E_2) - \gamma_{12}(E_2) \ln\left(\frac{\widetilde{E}_2}{E_2}\right) - m\left[\ln\left(\frac{\widetilde{E}_2}{E_2}\right)\right]^2 \\ &= \ln j(E_2) - \left[\gamma_{12}(E_2) + m \ln\left(\frac{\widetilde{E}_2}{E_2}\right)\right] \ln\left(\frac{\widetilde{E}_2}{E_2}\right) \end{aligned} \tag{4.14}$$

The terms in the square brackets above can be identified as the value of the spectral index at the midpoint of the PL02 energy channel,

$$\gamma_2(\widetilde{E}_2) = \gamma_{12}(E_2) + m \ln\left(\frac{\widetilde{E}_2}{E_2}\right) \tag{4.15}$$

note the value of the constant m is given by:

$$m = \frac{d\gamma_2(\widetilde{E}_2)}{d\ln(\widetilde{E}_2)} \tag{4.16}$$

where,

$$d\gamma_2(\widetilde{E}_2) = \gamma_{23} - \gamma_{12}$$

and

$$d\ln(\widetilde{E}_2) = \ln(E_3) - \ln(E_2)$$

Finally then, the value of the spectral index at the logarithmic mean energy of PL02 is given by the following equation:

$$\gamma_2(\tilde{E}_2) = \gamma_{12}(E_2) + \ln\left(\frac{\tilde{E}_2}{E_2}\right)\left[\frac{\gamma_{23} - \gamma_{12}}{\ln\left(\frac{E_3}{E_2}\right)}\right] \tag{4.17}$$

The value of the spectral index at the logarithmic mean energy of the PL0 channels was found from a parabolic fit to the power law energy spectrum, and from the value of the spectral indices at the common passband energies. These were found from the ratio of the count rates of the consecutive PL0 channels. In a similar fashion, the channel midpoint spectral indices in the other channels were found. Of course, certain approximations had to be made in the cases of PL01 and PL08 because there are not two channels bounding these. The summary set of equations used to find the midpoint spectral indices, and ultimately the fluxes at those channel midpoints, is given for reference:

$$\gamma_1(\tilde{E}_1) \approx \gamma_{12}(E_1) + \ln\left(\frac{\tilde{E}_1}{E_1}\right)\left[\frac{\gamma_{23} - \gamma_{12}}{\ln\left(\frac{E_2}{E_1}\right)}\right] \tag{4.18}$$

$$\gamma_2(\tilde{E}_2) = \gamma_{12}(E_2) + \ln\left(\frac{\tilde{E}_2}{E_2}\right)\left[\frac{\gamma_{23} - \gamma_{12}}{\ln\left(\frac{E_3}{E_2}\right)}\right] \tag{4.19}$$

$$\gamma_3(\tilde{E}_3) = \gamma_{23}(E_3) + \ln\left(\frac{\tilde{E}_3}{E_3}\right)\left[\frac{\gamma_{34} - \gamma_{23}}{\ln\left(\frac{E_4}{E_3}\right)}\right] \tag{4.20}$$

$$\gamma_4(\tilde{E}_4) = \gamma_{34}(E_4) + \ln\left(\frac{\tilde{E}_4}{E_4}\right)\left[\frac{\gamma_{45} - \gamma_{34}}{\ln\left(\frac{E_5}{E_4}\right)}\right] \tag{4.21}$$

$$\gamma_5(\tilde{E}_5) = \gamma_{45}(E_5) + \ln\left(\frac{\tilde{E}_5}{E_5}\right)\left[\frac{\gamma_{56} - \gamma_{45}}{\ln\left(\frac{E_6}{E_5}\right)}\right] \tag{4.22}$$

$$\gamma_6(\tilde{E}_6) = \gamma_{56}(E_6) + \ln\left(\frac{\tilde{E}_6}{E_6}\right)\left[\frac{\gamma_{67} - \gamma_{56}}{\ln\left(\frac{E_7}{E_6}\right)}\right] \tag{4.23}$$

$$\gamma_7(\tilde{E}_7) = \gamma_{67}(E_7) + \ln\left(\frac{\tilde{E}_7}{E_7}\right)\left[\frac{\gamma_{78} - \gamma_{67}}{\ln\left(\frac{E_8}{E_7}\right)}\right] \tag{4.24}$$

$$\gamma_8(\tilde{E}_8) \approx \gamma_{78}(E_8) + \ln\left(\frac{\tilde{E}_8}{E_8}\right)\left[\frac{\gamma_{78} - \gamma_{67}}{\ln\left(\frac{E_8}{E_7}\right)}\right] \tag{4.25}$$

4.4.2 The PL0 Energy Spectrum Evolution

Figures 4.4 through 4.7 show the energy spectrum ($\ln j$ vs. $\ln E$) of the PL0 channels as a function of time from DOY 100 to DOY 180, 1979 as measured by Voyager 2. As previously mentioned, the PL01 channel was unfortunately inoperable during the data interval of concern. As a result, the flux for this lowest energy channel was not available. The other seven fluxes of the Voyager 2 PL0 channels were calculated using the method described in the previous section.

The fluxes are calculated from six-hour averaged count rates, and hence are six-hour averaged quantities themselves. As a result of the averaging, the spectra represent omnidirectional (spin-averaged) energy spectra. The directional information obtained by the sectors of each PL0 channel is presented in chapter 5.

It is seen in Figures 4.4 to 4.7 that there is at least a small flux increase in the lowest energy channels within a single six hour averaging period in all but two of the presumed shock waves. The event R(1,2), at DOY 132, hour 02 and the event R(3,1), at DOY 165, hour 23 show no significant flux increases at the time of passage of the shocks. This is accountable by referring to Figure 4.2 and noticing

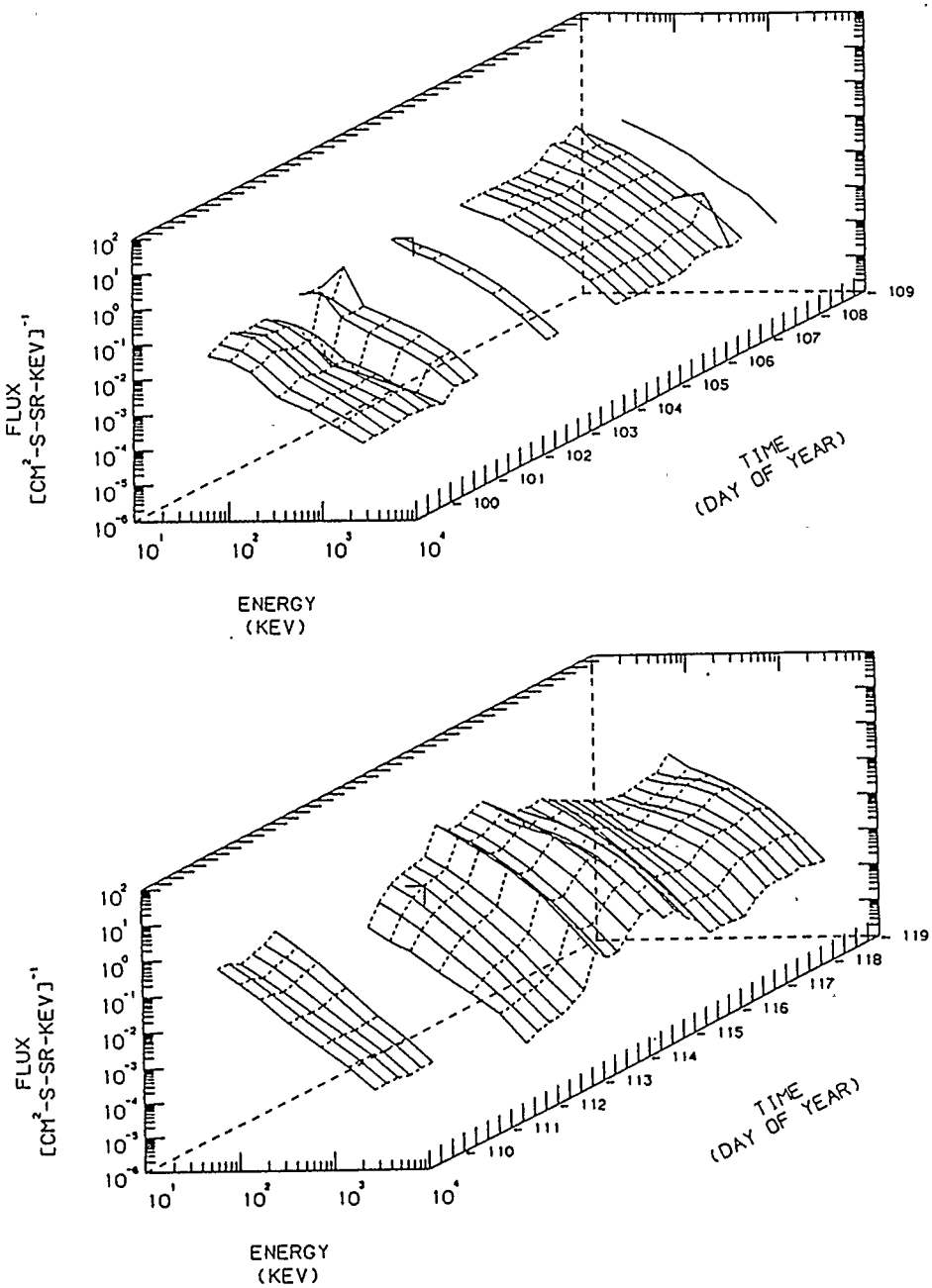

Figure 4.4: The Voyager 2 PL0 Energy Spectrum: DOY 100–119, 1979
The differential energy spectrum of the low energy charged particles as measured by the LEMPA detector PL0 channels is presented over the time interval from DOY 100 to DOY 119, 1979. The fluxes are six-hour spin averaged quantities.

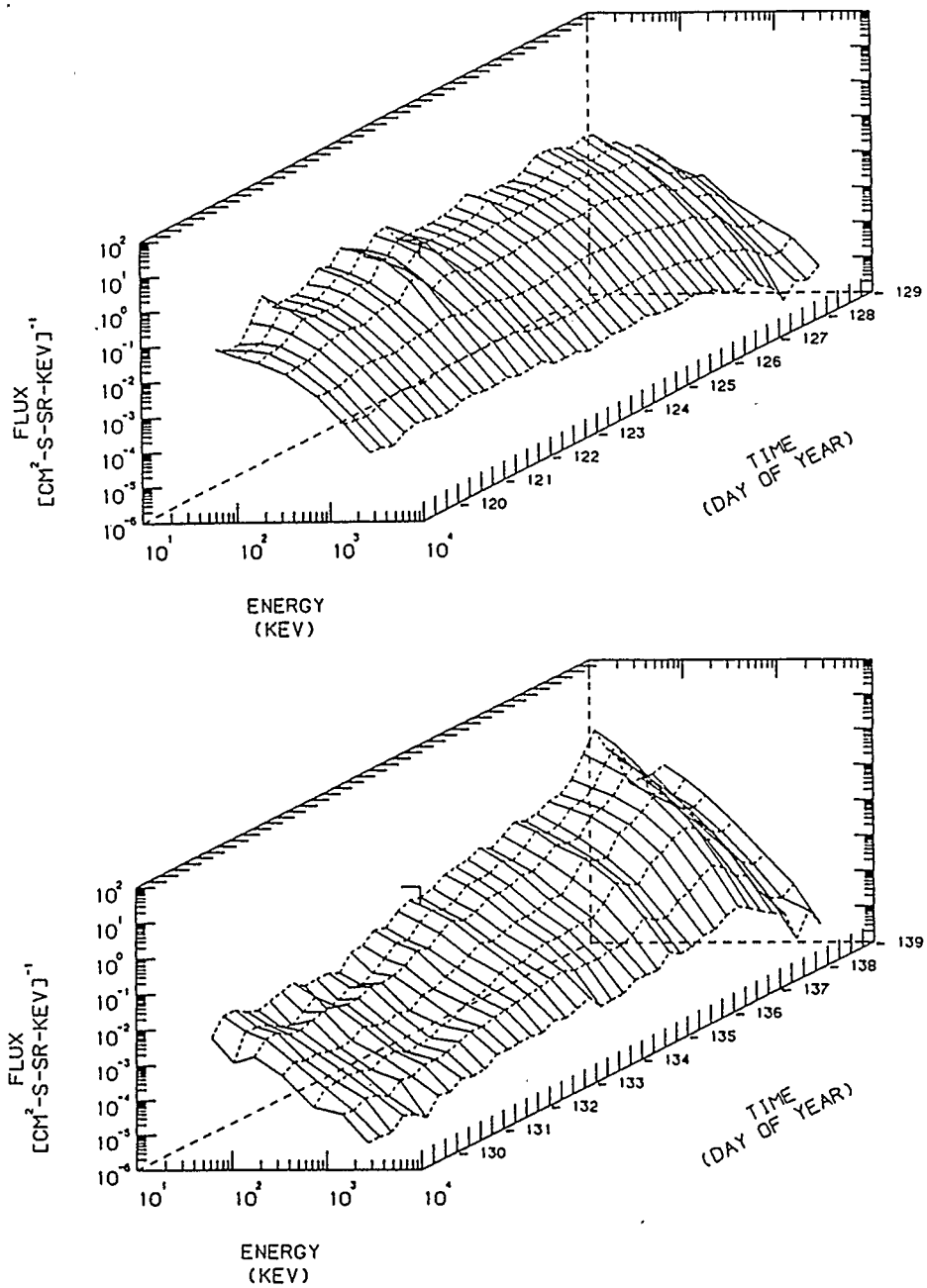

Figure 4.5: The Voyager 2 PL0 Energy Spectrum: DOY 119–139, 1979
The differential energy spectrum of the low energy charged particles as measured by the LEMPA detector PL0 channels is presented over the time interval from DOY 119 to DOY 139, 1979. The fluxes are six-hour spin averaged quantities.

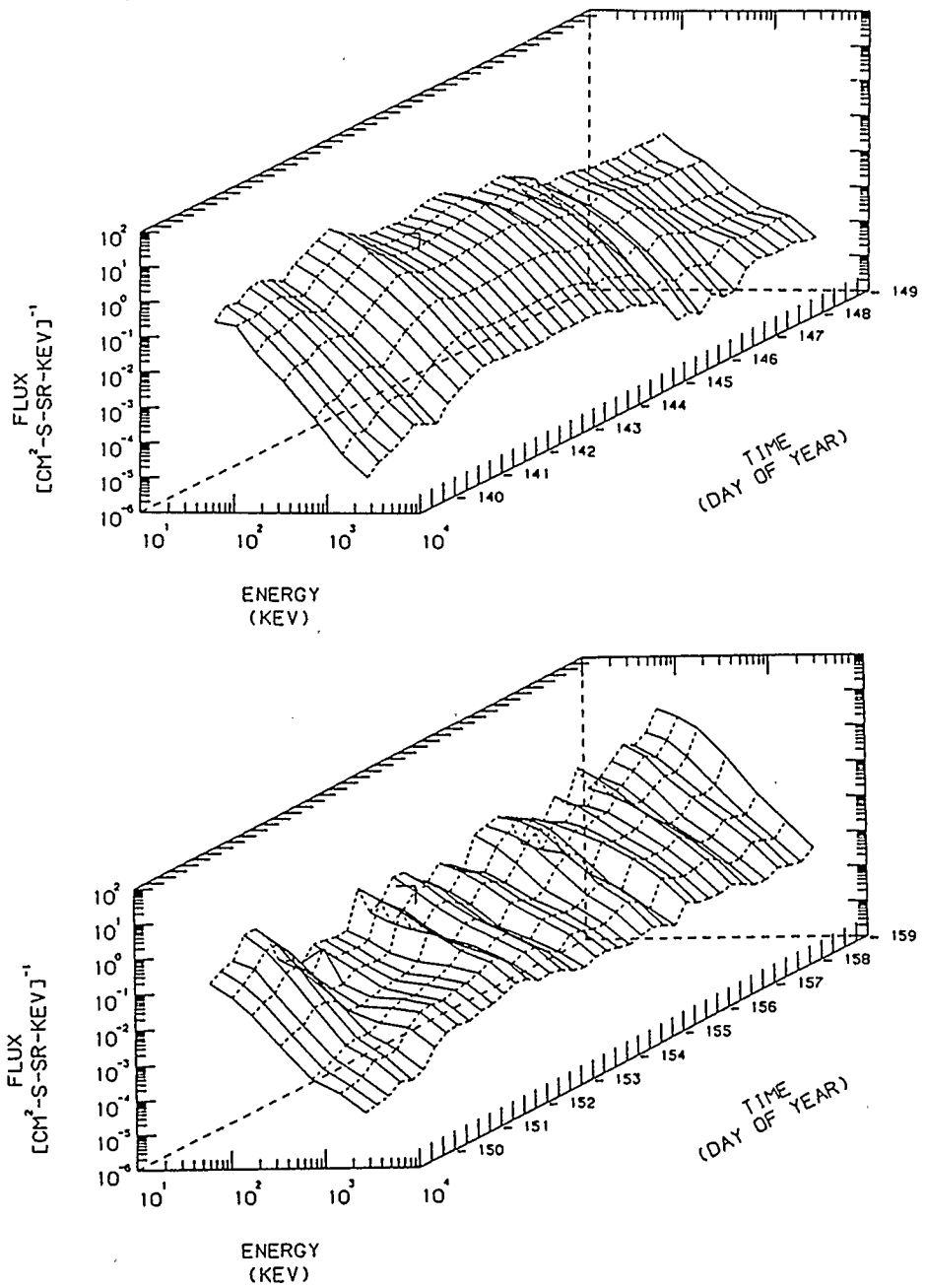

Figure 4.6: The Voyager 2 PL0 Energy Spectrum: DOY 139–159, 1979
The differential energy spectrum of the low energy charged particles as measured by the LEMPA detector PL0 channels is presented over the time interval from DOY 139 to DOY 159, 1979. The fluxes are six-hour spin averaged quantities.

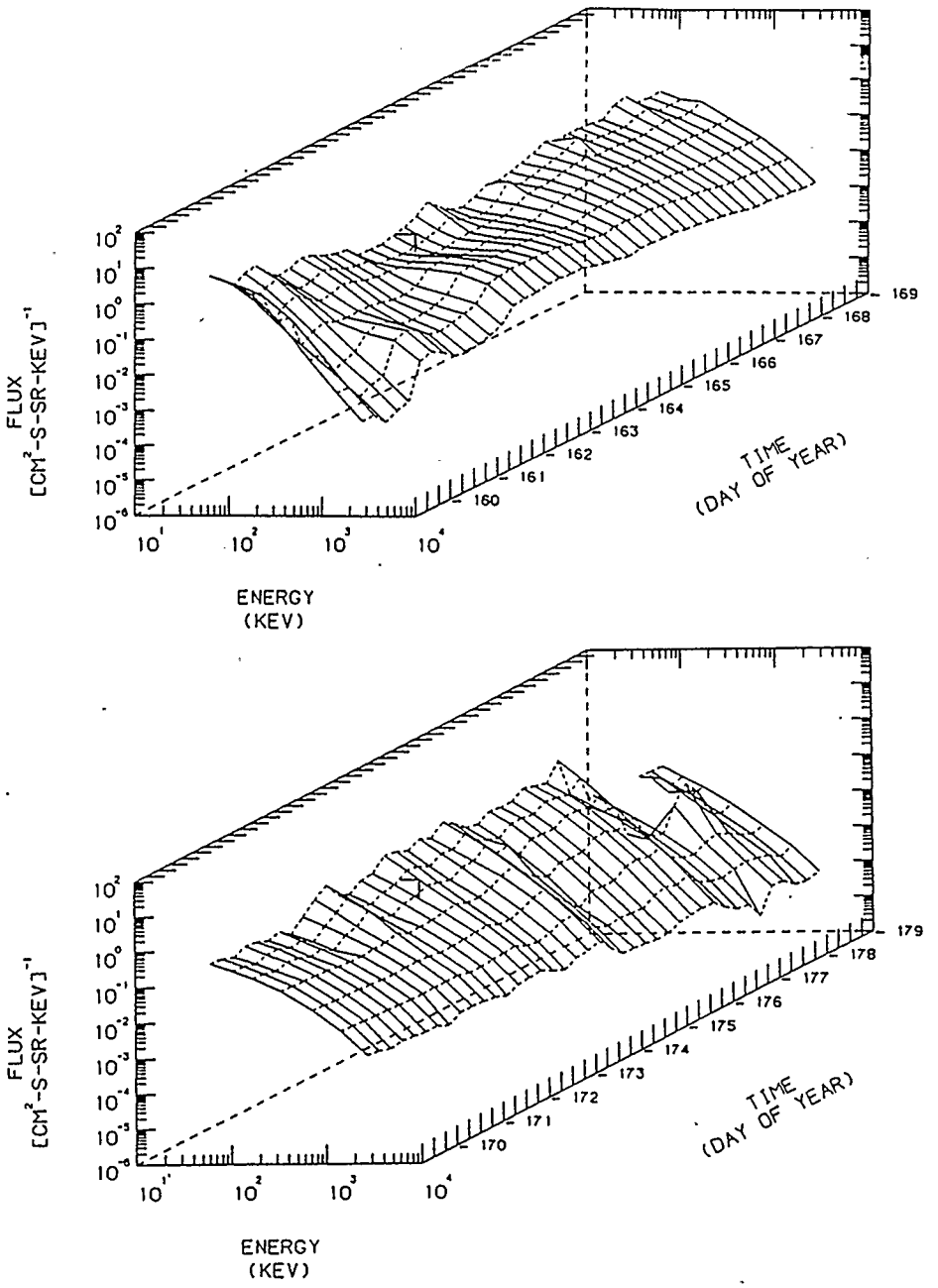

Figure 4.7: The Voyager 2 PL0 Energy Spectrum: DOY 159–179, 1979
The differential energy spectrum of the low energy charged particles as measured by the LEMPA detector PL0 channels is presented over the time interval from DOY 159 to DOY 179, 1979. The fluxes are six-hour spin averaged quantities.

that the count rate increase on the hourly averaged data was very small. The effect of the averaging over six hours has further reduced the amplitude of the particle enhancement.

The lower energy particles ($E < 200$ keV/nucleon) are more significantly enhanced than are those of greater energy, although R(1,1), F(2,1), R(2,1), and R(3,1) indicate acceleration at the higher energies. The event with the single largest flux enhancement is F(2,1). Figure 4.5 shows the lower energy particles' flux is significantly increased at a point immediately prior to the passage of the presumed forward shock. This event is looked at in more detail in chapter five.

It is noted in the PL0 channel energy spectrum that there is no *fold-over* at the lower energies. That is, to as low as PL02 energy the slope of the energy spectrum remains negative (ie. γ remains positive). The missing PL01 data becomes very important with regard to this point. It has been suggested that the lack of an energy spectrum fold-over at a shock locale indicates that the acceleration process extends to below the energy level of the lowest channel *(Richardson, 1985b; Balogh and Erdös, 1981)*. If so, and the particles in the energy range of PL01 show no spectrum flattening, then this may suggest that the source population of the accelerated particles may be the suprathermal solar wind ions with $E < 35$ keV *(Richardson, 1985b and references therein)*.

Chapter 5

CHARGED PARTICLE ANGULAR DISTRIBUTIONS

5.1 Importance of the Sectored Data

The angular distribution of the local low energy charged particle population is obtained by the rotating LECP detector system. The angular information is recorded as the detector scans through the eight 45° coplanar sectors. This angular data is used to fulfill one of the main objectives of the LECP experiment, as mentioned in chapter four: to observe the anisotropy of low energy charged particles in the vicinity of interplanetary shocks.

The theory of the shock drift acceleration process indicates that there is expected a large anti-shockward anisotropy upstream of the shock and an anisotropic particle flow downstream which is peaked perpendicular to the downstream field *(Pesses et al., 1982; Armstrong et al., 1985)*. The interaction of a charged particle with the shock front serves to increase the component of the particle's velocity parallel or anit-parallel (which ever is in the anti-shockward direction) to the upstream magnetic field. Particles that interact with the shock front for a long enough time can increase their anti-shockward component of velocity and can be injected back upstream. This is the origin of the upstream anisotropy. The degree of upstream anisotropy is very large in the case of near perpendicular shocks assuming a single

encounter *(Decker, 1983)*, but it has been suggested that these large anisotropies can also be associated with cases of multiple encounters *(Pesses and Decker, 1986)*. However, the earlier simulation studies of Decker and Vlahos *(1985)* show that the presence of scattering centres in the local up and downstream magnetic fields, while providing the opportunity for multiple shock encounters, generally reduces the particle anisotropies in the vicinity of a shock. The downstream anisotropy perpendicular to the field is the result of the particle attempting to conserve its first adiabatic invariant through the shock front *(Armstrong et al., 1977; Pesses et al., 1982)*.

For the first time using the LECP data from the Voyager 2 data, the particle anisotropies in the vicinity of a corotating shock will be examined *(Decker, private communication, 1988)*. In association with this observed angular data will be the results of a simulation study which attempts to model the same shock as that which produced the observed particle anisotropies. The model parameters are those which describe, as closely as possible, the conditions observed in the vicinity of the modeled shock event. The shock modeled is one of the corotating forward shocks presented in chapters three and four. The observed and simulated particle anisotropies and pitch angle distributions will be presented at times corresponding to a few hours before and after the passage of the shock.

5.2 Transformation from Spacecraft to Plasma Frame

As previously discussed, the Voyager 2 LEMPA sensor is responsible for detecting ions whose energies are within the approximate range of ~30 keV to ~4 MeV per

nucleon. Particles whose energies are as low as this are significantly influenced by the interplanetary magnetic field which is *frozen* into the solar wind plasma as it propagates radially outward from the sun. As a result of the convection of the field lines past the relatively stationary spacecraft detector, sectors of the detector which are on the sunward side tend to be flooded with particle counts. Since it is the particle velocities with respect to the interplanetary magnetic field which are of concern in pitch angle studies, a velocity transformation must be performed to rid the effect of the moving solar wind and its resultant anisotropy. In other words, a transformation must be made from the spacecraft frame, in which the data is recorded, to the relevant co-moving frame of reference.

The importance of such a transformation was first recognized and implemented by Compton and Getting *(1935)* in order to explain the effect of galactic rotation upon the intensity of incident cosmic rays. The magnitude of the first-order induced anisotropy is given by *(Gleeson and Axford, 1968)*:

$$\xi = 2(\gamma + 1)(V_{sw}/v) \tag{5.1}$$

where γ is the spectral index of the particle differential energy spectrum, V_{sw} is the speed of the solar wind, and v is the speed of the particle. Unfortunately, this linear transformation (linear in the ratio V_{sw}/v) is insufficient for lower energy particles. In this case, the condition that $V_{sw} \ll v$ is no longer valid; in fact, this ratio can be as low as $\sim 1/5$ for the LEMPA PL01 channel aboard Voyager 2.

An attempt was made by Ipavitch to perform a non-linear Compton-Getting transformation to the low energy IMP-7 particle data *(Ipavitch, 1974)*. This data pertained to particle energies less than a few hundred keV per nucleon ($V_{sw}/v \sim$

1/12), so higher order terms of the velocity ratio were needed. His technique was limited, however, by the assumption that the angular rates were isotropic in the plasma frame *(Gold et al., 1975)*. Other than a mathematical convenience, there is no physical basis for such a restricted assumption.

A generalized non-linear Compton-Getting transformation procedure was developed in 1975 by Gold *(Gold et al., 1975)* which makes no assumptions regarding the plasma frame angular distribution of particles. Before outlining this procedure, it is necessary to explicitly define the relevant coordinate systems involved.

5.2.1 Coordinate Systems

It is imperative to define a coordinate system that is fixed with respect to the Voyager 2 spacecraft LECP scan plane (LSP), and relate it to the already defined RTN coordinate system. Define the positive x-axis of this new coordinate system, the LSP system, to bisect sector 8 of the LECP scan plane. Therefore the positive y-axis bisects sector 2 and the z-axis forms the right-handed orthogonal triad (See Figure 5.1). Since the Voyager spacecraft are not spin-stabilized vehicles, such a selection of a coordinate system is not too unnatural or burdensome to work with.

In general, the IMF and solar wind vectors are oriented to the LSP such that they can be described by an azimuth and altitude angle in the LSP frame. Note that the solar wind is taken to be solely in the radial direction. Let ϕ_r be the azimuth angle (as measured positive in the counter-clockwise direction from the positive LSP x-axis) and ψ_r be the altitude angle of the solar wind velocity in the LSP frame (See Figure 5.1). The solar wind vector in the LSP frame is given by:

LECP Scan Plane
Coordinate System

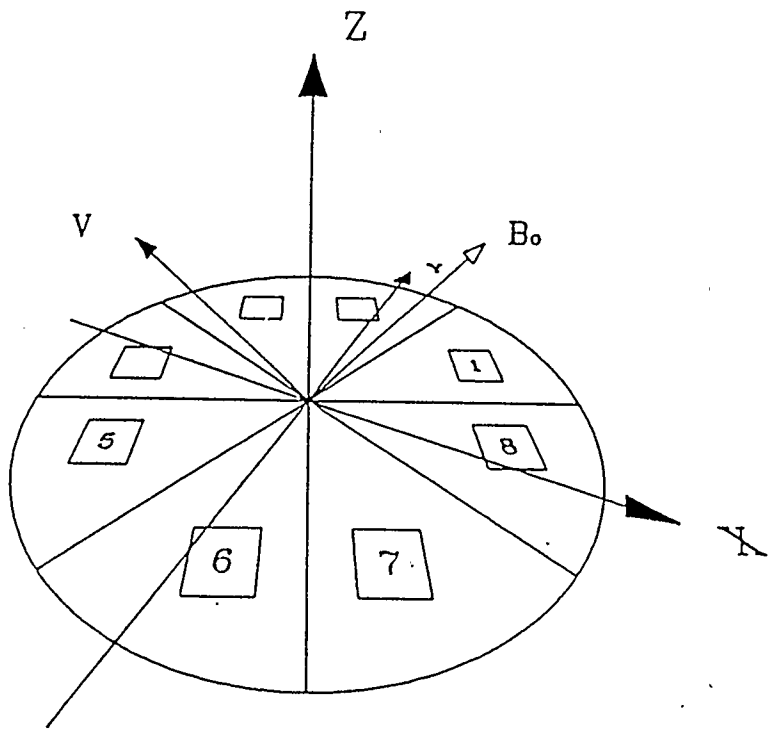

Figure 5.1: The LECP Scan Plane Coordinate System

The LECP scan plane coordinate system is defined such that the positive x-axis bisects sector 8 of the scan plane, the positive y-axis bisects sector 2, and the z-axis completes the right-handed orthogonal system.

$$\vec{V}_{sw} = V_{sw}[\cos\phi_r \cos\psi_r, \sin\phi_r \cos\psi_r, \sin\psi_r] \tag{5.2}$$

and the IMF vector in the LSP frame is given by:

$$\vec{B} = B[\cos\phi_B \cos\psi_B, \sin\phi_B \cos\psi_B, \sin\psi_B] \tag{5.3}$$

Transformations between the LSP frame and the RTN frame are obtained via the general transformation matrix, or its inverse:

$$\begin{pmatrix} L_x \\ L_y \\ L_z \end{pmatrix} = \begin{bmatrix} a_{xr} & a_{xt} & a_{xn} \\ a_{yr} & a_{yt} & a_{yn} \\ a_{zr} & a_{zt} & a_{zn} \end{bmatrix} \begin{pmatrix} L_r \\ L_t \\ L_n \end{pmatrix} \tag{5.4}$$

where the L's are components of a vector, either the IMF or the solar wind, to be expressed in either the LSP or RTN system. The elements of the transformation matrix were graciously provided as part of the Voyager data tape. With the knowledge of the appropriate coordinate systems involved, a Compton-Getting transformation can now be described.

5.2.2 Compton-Getting Transformations

The particle velocities in the LSP frame (unprimed) and the co-moving, or plasma, frame (primed) are related by:

$$\vec{v'} = \vec{v} - \vec{V}_{sw} \tag{5.5}$$

where $\vec{V}_{sw}$ is the solar wind velocity. Note that this is a simple Galilean velocity transformation which is valid since the magnitudes of all the velocities involved are significantly less than the speed of light.

As in chapter four, let the differential energy spectrum in the LSP frame be represented by a simple power law:

$$j(E) = j_\circ \left(\frac{E}{E_\circ}\right)^{-\gamma} \tag{5.6}$$

The particle phase space distribution, $f(v)$, taken here as a function of velocity alone, is related to the differential energy spectrum by *(Forman, 1970)*:

$$f(v) = v^{-2} j(E) \tag{5.7}$$

It was also shown by Forman that the phase space distribution is Lorentz invariant; that is, it satisfies the conditions of Liouville's theorem. As a result of this, the particle distribution functions are equivalent in both the LSP and plasma frames:

$$f(v) = f'(v') \tag{5.8}$$

with

$$f'(v') = v'^{-2} j'(E') \tag{5.9}$$

Combining equations 5.7 and 5.9, it follows that,

$$j'(E') = \left(\frac{v'}{v}\right)^2 j(E) \tag{5.10}$$

This equation directly relates the particle fluxes in the LSP (unprimed) and plasma (primed) frames of reference. Using equation 5.6,

$$j'(E') = \left(\frac{v'}{v}\right)^2 j_\circ \left(\frac{E}{E_\circ}\right)^{-\gamma} \tag{5.11}$$

This equation can be multiplied by $(E'/E')^{-\gamma}$ to obtain the following, after making the simple substitution that $(v'/v)^2 = (E'/E)$,

$$j'(E') = j_\circ \left(\frac{E'}{E}\right) \left(\frac{E'}{E_\circ}\right)^{-\gamma} \left(\frac{E}{E'}\right)^{-\gamma} \tag{5.12}$$

Rearranging this equation slightly,

$$j'(E') = j_\circ \left(\frac{E'}{E_\circ}\right)^{-\gamma} \left(\frac{E'}{E}\right)^{\gamma+1} \tag{5.13}$$

or,

$$j'(E') = j(E') \left(\frac{E'}{E}\right)^{\gamma+1} \tag{5.14}$$

where $j(E')$ is merely that quantity calculated from equation 5.6 evaluated at $E = E'$.

A simple relationship between the quantities E and E' can be derived from equation 5.5. Squaring this equation,

$$v'^2 = \vec{v'} \cdot \vec{v'} = v^2 - 2\left(\vec{v} \cdot \vec{V}_{sw}\right) + V_{sw}^2 \tag{5.15}$$

Letting $\epsilon = (V_{sw}/v)$, and ϕ be the angle between $\vec{v}$ and $\vec{V}_{sw}$, the above equation becomes,

$$\left(\frac{v'}{v}\right)^2 = \left(\frac{E'}{E}\right) = 1 - 2\epsilon\cos\phi + \epsilon^2 \tag{5.16}$$

This can be used in equation 5.14 to derive the aforementioned first-order anisotropy coefficient. From 5.14 and 5.16,

$$j'(E') = j(E')\left(1 - 2\epsilon\cos\phi + \epsilon^2\right)^{\gamma+1} \tag{5.17}$$

In the high energy limit, as $\epsilon \ll 1$, 5.17 expands to,

$$j'(E') \approx (1 - 2\epsilon(\gamma+1)\cos\phi)\, j(E') \tag{5.18}$$

where the first-order anisotropy coefficient, $\xi = 2(\gamma+1)(V_{sw}/v)$ as given by equation 5.1, is recognized as the difference between the fluxes in the plasma and LSP frames.

Note that the spectral index as well as the fluxes are generally directionally dependent *(Gold et al., 1975)* although a spin-averaged gamma is usually sufficient, introducing only a small approximation to the procedure *(Kessel, 1986)*. In the procedures in this study a spin-averaged spectral index was used. The Compton-Getting transformation which produced the plasma frame fluxes from the LSP frame fluxes is given by equation 5.14.

5.3 Numerical Models in Heliospheric Studies

Interest in heliospheric plasma simulations has risen in recent years due to both the technological advancements in computer hardware (and software) and the availability of *in situ* spacecraft data. Previously, simulations were limited because of computational restrictions such as accumulating round-off errors and memory constraints. Present day *supercomputers* and improved algorithms are making realistic

simulations not only feasible but very informative. It is appropriate to introduce the types of simulations in use—this will provide insight into the physics involved and at the same time define relevant terms used in the field of heliospheric plasma simulations.

Plasma simulations are generally of two types *(Birdsall and Langdon, 1986)*, those based upon the kinetic description of a plasma and those based upon the fluid description. Those based upon the fluid description merely integrate the MHD fluid equations presented in chapter one (1.12–1.14). The result describes the collective behaviour of the plasma with no information regarding the individual constituent particles. Kinetic simulations attempt to provide more detailed information by the integration of the Vlasov, or collisionless Boltzmann, equation (1.11) or of the Fokker-Planck equation (1.36).

Particle codes can be considered as a subset of the kinetic simulations mentioned above. They are an attempt to solve the simultaneous problem of the particle dynamics and the field values. That is, the value of the electromagnetic fields determines the particle dynamics while at the same time the motion of the particles determines the fields via the Maxwell equations. The basic algorithm is simple: a number of particles initially exist in an electromagnetic field, the particles are then perturbed slightly and the resulting electromagnetic fields are recalculated from the Maxwell equations. The forces upon each particle are calculated from the new fields. The new forces result in new positions and velocities of the particles, hence current and charge densities, which in turn describe new fields. The calculations are iteratively continued.

It is this type of simulation which can provide an exact plasma description

but is very expensive in terms of computation. These types of simulations are restricted to a relatively few particles ($\sim 10^3$). Fortunately, it has been shown that as little as a few thousand particles can accurately describe the collective behaviour of a plasma consisting of on the order of 10^{24} particles. Also in use are what are termed *hybrid* codes which are combination of the fluid algorithms and the particle codes *(Quest, 1985)*. These techniques involve a fluid description of the electrons but follow the dynamics of the ions explicitly. This is an attempted compromise between the numerous calculations involved in the particle codes and the lack of individual particle information.

The type of simulation used in the present study does not fall precisely into either of the kinetic or fluid categories, although it is definitely more related to the kinetic codes discussed. The simulation used in this study, 'MS2', had its origin prior to 1980. It was to constitute the major effort in the PhD. program of its author, Dr. Robert Decker, at the Department of Physics and Astronomy at the University of Kansas in Lawrence, Kansas. This code has been subject to many revisions and additions and is still finding pertinent applications in the area of heliospheric studies. Details of the algorithm are dealt with in a later section. At this point it is sufficient to compare it with the aforementioned algorithms in a qualitative manner.

MS2 is best described as an *injection algorithm*. The trajectories of individual particles are integrated in the presence of *prescribed* electromagnetic fields. The particles are injected and their equations of motion are integrated individually. The particles are treated merely as test particles, they have no effect upon the electromagnetic fields through the Maxwell equations. In spite of this assumption,

the results of the model have been very informative. The modeling of magnetic fluctuations in the upstream and downstream regions of the simulated shock have provided the opportunity to compare simulated particle anisotropies with those observed in the observed spacecraft data. The model is presented in more detail in the next section.

5.4 Description of MS2

The model employed here, MS2, numerically integrates along the phase space orbit of a charged particle under the conditions describing an oblique, fast mode, collisionless magnetohydrodynamic shock wave. The model is completely general; there are over 30 variable initial parameters, allowing it to be applicable in a wide range of shock acceleration problems. Of critical importance to the acceleration process are the following parameters: the upstream shock normal angle θ_{Bn}, the magnitude of the mean upstream magnetic field $\vec{B}_1$, the shock frame magnitude of the upstream plasma flow into the shock front $\vec{U}_1$, the upstream field variance σ_1^2, and the upstream plasma beta β_1. The corresponding downstream values are determined from those upstream with the aid of the Rankine-Hugoniot 'jump' conditions, as discussed in chapter 2. In this study, these parameters were chosen to as completely as possible correspond to those actually found by the Voyager 2 spacecraft for a specific shock event. These parameters will be discussed in the next section. First it is imperative to describe somewhat in detail the model which was used in this study.

In the most simplistic terms, the model numerically integrates Newton's second

law of motion. In the case of a moving charged particle in the presence of a magnetic field, this equation of motion is also known as the Lorentz equation. In a particular plasma frame (to be discussed), the Lorentz equation is given by:

$$\frac{d\vec{p}(t)}{dt} = \frac{q}{c}\left[\frac{\vec{p}(t)}{m} \times \left(\vec{B}_0 + \vec{b}(z)\right)\right] \tag{5.19}$$

with

$$\frac{d\vec{x}(t)}{dt} = \frac{\vec{p}(t)}{m} \tag{5.20}$$

where $\vec{p}(t)$ is the particle momentum, q and m are the charge and mass of the particle, c is the speed of light, $\vec{B}_0$ is the mean magnetic field, and $\vec{b}(z)$ is a superimposed, zero mean, perpendicular random magnetic field component. This random field component produces a total field which is not in general totally laminar. The component $\vec{b}(z)$ is transverse to the mean component, thus introducing the possibility of particle pitch angle scattering. The form of this random component is also to be discussed. Note that the mass m in the above equations is the relativistic mass so that the simulation can be used for high energy particles.

Some simplifying assumptions regarding the geometry of the situation have been introduced into the procedure. Most importantly, the shock front has been assumed to be planar and infinite in extent. This means that the shock front is essentially uniform for as long as the dynamics of the particle suggests it is interacting with the shock. One can neglect any variation in θ_{Bn} as a result of a spherical shock front. Kessel *(1986)* discusses the extent to which this assumption is valid. Versions of the model used in this study with a curved shock front are

currently under development *(Decker, private communication, 1988)*.

The shock is also assumed to be of negligible thickness, at least in comparison to the particle's gyroradius. As a result of this assumption, the particle 'senses' the shock front only as a kink in the magnetic field. The upstream magnetic field magnitude is instantaneously magnified (for fastmode shocks) to the downstream value as governed by the jump equations. For perpendicular, or quasi-perpendicular shocks ($45° < \theta_{Bn} < 90°$) this is a qualified assumption whereas for quasi-parallel shocks this assumption is suspect *(Greenstadt and Fredericks, 1979; Terasawa, 1979)*.

5.4.1 Model Reference Frames

In performing such a simulation, it is convenient to define three frames of reference. Let K be the frame of reference that is fixed with respect to the shock, and K_i be the frame co-moving with the upstream plasma (i=1) or the downstream plasma (i=2). Figure 5.2 demonstrates the geometry of the shock and the relationship between the three coordinate systems (after *Decker and Vlahos, 1986a*). The shock is assumed to propagate in the direction of its normal vector, n, which is in the negative x direction (in the shock frame), with a constant velocity $\vec{V}_{sh}$. The shock coincides with the y-z plane of the K system. Upstream quantities are negative and downstream quantities are positive as viewed in the K frame.

If $\vec{V}_1$ is the upstream plasma velocity in the inertial frame then the upstream plasma has a flow velocity, as observed from the K system, of

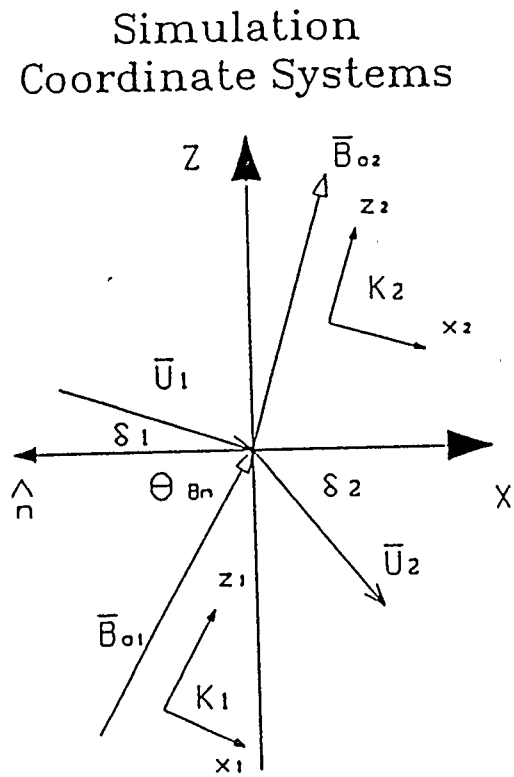

Figure 5.2: The Model Simulation Coordinate Systems

It is convenient to define three coordinate systems in the description of the physics near the shock front. There are coordinate systems fixed with both the upstream and downstream plasma flows (K_i: $i = 1$ upstream, $i = 2$ downstream) as well as with the shock front itself (K).

$$\begin{aligned}\vec{U}_1 &= \vec{V}_1 - \vec{V}_{sh} \\ &= U_1 \left(\cos\left(\delta_1\right), 0, -\sin\left(\delta_1\right)\right)\end{aligned} \tag{5.21}$$

and similarly, the downstream flow velocity is

$$\vec{U}_2 = U_2 \left(\cos\left(\delta_2\right), 0, \sin\left(\delta_2\right)\right) \tag{5.22}$$

where δ_1 and δ_2 are the angles between $\vec{U}_1$ and $\vec{U}_2$ and the shock normal, respectively.

The co-moving frames are defined such that their positive z-axes are in the direction of the local mean magnetic field. The direction of the positive y-axes are in a direction parallel to the y-axis of the K system.

In either of the plasma coordinate systems, there exists no static electric field because of the assumption of infinite conductivity. However, as viewed from the shock frame, there is a constant convective $\vec{U} \times \vec{B}$ electric field which is responsible for a drift of the particle's guiding centre in a direction parallel to the shock front. Recall that it is this drift which lends its name to the process known as 'shock drift' acceleration. The direction of this electric field is in the direction of the positive y-axes in Figure 5.2 . The simulation integrates the particle's motion in the appropriate, either the upstream or downstream, plasma frame. The integration continues until one of several occurrences; a pre-defined temporal or spatial limit is exceeded or a non-physical error is discovered. Such a non-physical error includes non-conservation of the particle's kinetic energy in either plasma frame solely as a

result of the numerical computations. If this is the case, the particle calculation is discontinued and another particle is injected.

The multi-particle procedure involves injecting the particles one at a time with an initial energy (yet another simulation parameter) at a specified distance upstream of the shock front. The ensemble of particles is injected isotropically, each pitch angle and gyrophase is chosen randomly such that there is a uniform probability that a particle will exist initially anywhere on a sphere in velocity space. Any modulation to this initial isotropy is a direct result of interactions with the shock and the ensuing acceleration processes. This modulation is, of course, a function of the initial parameters.

5.4.2 Synthesized Random Magnetic Field Component

As previously mentioned, it is necessary to impose a component of the total magnetic field in a direction perpendicular to the mean field in the up and downstream plasmas. These irregularities provide a mechanism for pitch angle scattering, and thus allow the first-order Fermi acceleration process to occur. In the absence of these scattering centres (ie. a totally laminar field), the particle motion would be helical about the field lines with a constant gyrofrequency and component of velocity parallel to the magnetic field and there would be at most one interaction with the shock front, resulting in only a small chance for significant acceleration by the shock drift method.

The following form of a zero-mean, transverse random magnetic field component, in the appropriate plasma frame, is used by the simulation *(Decker and Vlahos, 1986a, 1986b)*:

$$\vec{b}_i(z) = \hat{x}b_{xi}(z) + \hat{y}b_{yi}(z) \tag{5.23}$$

where the subscript i is 1 upstream and 2 downstream of the shock. Note that $b(z)$ is a function only of the z coordinate which is parallel to the mean field. The $b(z)$ is also static and this implies perfectly elastic scattering. The total field, then, in either plasma frame is:

$$\vec{B}_i(z) = \vec{B}_{0i} + \vec{b}_i(z) \tag{5.24}$$

Note that this form of $b(z)$ ensures that the magnetic field is divergence free. The random field component is synthesized along the mean field, and $b(z)$ is the superposition of 4096 circularly polarized Alfven waves with wavevectors parallel (or anti-parallel) to the mean field *(Decker and Vlahos, 1986a)*. The amplitudes of the Fourier components are derived from a specified functional form of the wavenumber spectrum. The form of the wavenumber power spectral density used in the simulation is *(Hedgcock, 1975)*:

$$P(k) = \frac{2\mu \sin(\pi/\mu)\, z_c \sigma^2}{1 + (kz_c)^{\mu}} \tag{5.25}$$

where μ is the the exponent of the random field power spectrum, σ is the standard deviation of the field, and z_c is the correlation length of the random field.

The values of $b(z)$ are generated along a length of B_{0i} at an equal grid spacing using the functional form of $P(k)$ above and from a generation of random phase angles. For specific details of the Fourier analysis, see Appendix B in Decker and Vlahos, *(1986a)*.

5.5 Determination of the Model Parameters

The purpose of this section is to introduce the particular shock event that is to be simulated. A judicious selection of one of the events described in chapters three and four was necessary for a number of reasons. First and foremost, the event chosen had to have a high probability of being an actual shock. The solar wind speed and magnetic field profiles were to be distinctly representative of a shock passage. Also, data gaps in the particle count rates, solar wind speed, and IMF vector were to be avoided.

The most obvious candidate for the simulation based on this criterion was the forward shock event F(2,1). This shock passage was detected by Voyager 2 at 79/138/01 (YR/DOY/HR). This was fortunate since the coverage was excellent at this time in anticipation of the Jupiter encounter. The parameters used in the simulation were to coincide, where possible, with the physical conditions prevalent at the time of the shock passage. A list of the most relevant parameters derived from the data or taken from the literature are listed:

Mean Upstream Magnetic Field

The average upstream magnetic field magnitude was taken directly from the Voyager 2 magnetometer data as presented in Figure 3.6. The value used in the simulation was 3.5×10^{-6} gauss. As is seen from this diagram, the mean field did not vary appreciably immediately upstream of shock F(2,1) (See also Tables 3.11 and 3.12). The polarity of the IMF at this time and location was such that $\lambda_B \sim 90°$.

Angle of the Shock Normal

The importance of the value of the angle θ_{Bn} has been discussed in chapter 3. The acceleration process is highly sensitive to the value of this parameter and as a result much care has been taken to calculate its value. The value used in the simulation for this parameter was 85°. This value was derived via the magnetic coplanarity method as indicated in Tables 3.7–3.10. According to this theory, the shock normal $\hat{n}$ is given by:

$$\hat{n} = \frac{\left(\vec{B}_{01} \times \vec{B}_{02}\right) \times \left(\vec{B}_{02} - \vec{B}_{01}\right)}{\mid \left(\vec{B}_{01} \times \vec{B}_{02}\right) \times \left(\vec{B}_{02} - \vec{B}_{01}\right) \mid} \tag{5.26}$$

Note that both the average and median values of the upstream and downstream magnetic fields were used in this determination method, as discussed in chapter three. The presence of the sector boundary approximately seven hours after suspected shock limited the coplanarity method. Data prior to this sector boundary was used in the above formula.

Upstream Plasma Flow Velocity

The value used in the simulation was 60 km/s, as derived from shock velocity and solar wind velocity. The shock velocity was estimated by a simple two-point estimate using both Voyager 1 and Voyager 2 spacecraft. The shock was pronounced enough to be easily identified in the solar wind and magnitude field profiles of both spacecraft, as was seen earlier. Accurate knowledge of the radial distances of both spacecraft, which are at essentially the same heliolongitude (0.20 degree difference) and heliolatitude (3.0 degree difference), leads directly to an estimate of the average radial shock speed. This method of course assumes that the velocity of the shock is approximately constant over the distance from Voyager 2 to Voyager 1.

Upstream Alfven Mach Number

The upstream Mach number, Ma_1, was calculated from the usual formula:

$$Ma_1 = U_1/Va_1 = (U_1/B_{01})\sqrt{4\pi\rho_1} \tag{5.27}$$

where Va_1 is the upstream Alfven velocity, ρ_1 is the upstream plasma mass density. This value was calculated from the product of the mass of a proton and the local proton number density. An estimate of the number density as 0.1 cm^{-3} was used as quoted by Goldstein et al., *(1984)*. It is noted though that this value was for Voyager 1 particle data during the same time period and it is assumed that the number density in the vicinity of Voyager 2 is not too far different.

Upstream Plasma Beta

The upstream plasma beta, β_1, was derived from the formula:

$$\beta_1 = \frac{\rho_n k_b (T_{i1} + T_{e1})}{B_{01}^2/8\pi} \tag{5.28}$$

where T_{i1} is the upstream ion temperature and T_{e1} is the upstream electron temperature, $(T_{i1} + T_{e1}) = 2T$. The value of T was obtained by equating the mean kinetic energy of a proton in terms of the thermal velocity and in terms of temperature:

$$\frac{1}{2}mv^2 = \frac{1}{2}k_b T$$

The resultant value of T was found to be 12,100 Kelvin. The value of v, the thermal proton speed, was 1.0×10^6 cm/s, from Goldstein, Burlaga, and Matthaeus, *(1984)*. It is noted that this assumes only one degree of freedom of the protons.

	B	θ_{Bn}	U	δ	Ma
Upstream	3.5×10^{-6} gauss	85.0°	60.0 km/s	0.0°	2.50
Downstream	7.6×10^{-6} gauss	87.7°	27.7 km/s	2.0°	0.78

Table 5.1: The Upstream and Downstream Parameter Sets
The downstream values of the critical parameters in the shock vicinity were calculated from those upstream via the magnetic Rankine-Hugoniot equations. The value of δ indicates the angle between the normal to the shock and upstream (downstream) flow into (out of) the shock.

A correction may be required here if the magnetic field is not strong enough to sufficiently constrain the protons to validate this assumption. Using a full three degrees of freedom, the calculated plasma beta is 0.30 instead of 0.68.

With these values of the upstream parameter set $(\vec{B}_1, \theta_{Bn}, \vec{U}_1, Ma_1)$, the corresponding downstream values were calculated from the magnetic Rankine-Hugoniot equations. The results are presented in Table 5.1.

Upper Time Limit of Integration

A value of 1000 gyroperiods was chosen so as to minimize the simulation run time without cutting off valuable portions of the particle trajectories. No change in the resultant pitch angle distributions occurred as a result of increasing the integration time (subject to the spatial constraint).

Variance of Random Fields

The variance in the upstream and downstream magnetic fields were chosen to correspond with those observed in the original Voyager 2 data. It is important to note that the simulation generates up and downstream fluctuations independently, no attempt is made to carefully transmit upstream waves into the downstream

region.

The field fluctuations generated are actually the superposition of two distinct physical processes. In each region there is a background, or ambient, set of fluctuations as well as a secondary *shock-associated* set. This shock-associated set is an attempt to model MHD waves which may be generated by energetic ions streaming away from the shock *(Decker, 1988)*. The amplitudes of the shock-associated waves are damped such that they decrease with increasing distance from the shock front. The two types of waves are each generated via an equation of the type of 5.25.

Figure 5.3 shows the power spectra of the ambient and shock-associated waves used in this study. Note especially the presence of power of both the ambient and shock-associated waves in the energy range of the Voyager 2 LECP. The condition for resonance between the fluctuations and the particles is:

$$k^{-1} \sim r_{g1} \equiv \frac{mcv_{\perp}}{eB_{01}} \tag{5.29}$$

where $k = (2\pi/\lambda)$ is the wavenumber, λ is the wavelength, r_{g1} is the upstream gyroradius based on the upstream mean magnetic field B_{01}, and $v_{\perp}$ is the component of the particle velocity perpendicular to the upstream mean magnetic field. This resonance condition ensures the possibility of pitch angle scattering.

The ambient upstream and downstream field variances divided by the mean field used in the simulation was, $(i = 1, 2)$:

$$\left(\frac{\sigma_i}{B_{0i}}\right)^2 = 0.04$$

The shock-associated upstream and downstream field variances divided by the mean field used in the simulation was, $(i = 1, 2)$:

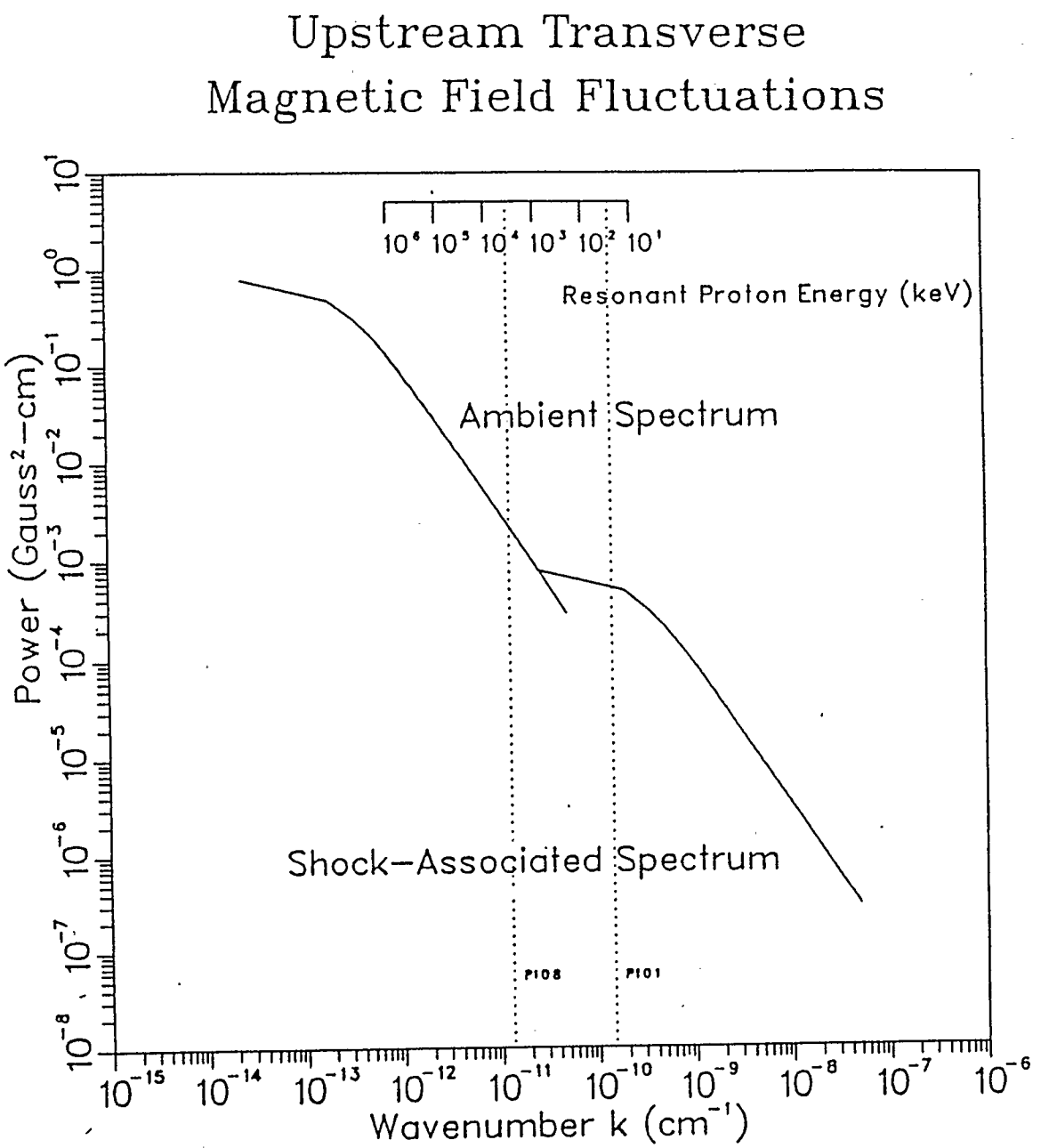

Figure 5.3: The Power Spectra of the Simulated Waves
Note the presence of power at the wavenumbers corresponding to the energy of all Voyager 2 PLO channels for both the ambient and shock- associated fluctuations.

$$\left(\frac{\sigma_i}{B_{0i}}\right)^2 = 0.5$$

Exponent of Random Field Power Spectrum

The value used for the simulation was $\mu = 1.5$ for both the ambient and shock-associated spectra, upstream and downstream. This value was chosen from Owens *(1978)* and Hedgcock *(1975)*.

Correlation Length of Random Field

The correlation length of the random field component can be roughly defined to be the distance over which, on average, two values of $\vec{b}(z)$ will be completely different in both magnitude and direction. It is a quantitative measure of the scale length in the variance of the magnetic field.

The number used in the simulation for the ambient wave field correlation length, z_c, was 4.0×10^{12} cm as listed by Goldstein et al., *(1984)*. The correlation length chosen for the shock-associated wave field was 4.0×10^9 cm as suggested by Decker *(private communication, 1988)*.

Conceptual Plane Spacing

Conceptual planes, parallel to the shock plane, were situated up and downstream of the simulated shock coinciding with distances corresponding to 1, 2, 3, ..., hours before the passage of the shock by Voyager 2. The simulated particle pitch angles were accumulated whenever a simulated particle crossed a plane. The plane spacing corresponding to one hour intervals upstream of the shock are given by $V_{sh} \times 3600$ s $= 1.55 \times 10^{11}$ cm. The one-hour averaged observed data was compared directly with the simulated data accumulated in this manner.

LECP Channel	Lower Passband (keV)	Upper Passband (keV)
PL01	30.0	53.4
PL02	53.4	94.9
PL03	94.9	168.8
PL04	168.8	300.1
PL05	300.1	533.7
PL06	533.7	948.6
PL07	948.6	1688.0
PL08	1688.0	3001.6

Table 5.2: The Simulated Voyager 2 PL0 Channel Energy Passbands
The simulated energy passbands of the PL0 channels of the Voyager 2 LECP experiment are indicated. The logarithmically spaced channels deviate only by a small amount from the values for the real PL0 channels (chapter 4) in the higher energy channels (14% difference for the upper passband of PL08).

The only parameter that varied from run to run of the simulation was the monoenergetic injection energy. In each case, the injection energy was the lower passband limit corresponding to the Voyager 2 LECP, as given by Table 4.2. Table 5.2 provides the simulated energy passbands used in the simulation. These were constructed so as to correspond as closely as possible to those of the actual LECP experiment of Voyager 2. This table can be compared directly to Table 4.2. It is seen that there is only a small discrepancy between the two tables. The simulated channels were chosen as such because of their simple logarithmic progression.

The simulation was run at each of the eight simulated LECP energies and the results were merged together to form the effective total pitch angle distributions. Four hundred particles per initial injection energy were injected one gyroradius upstream with random gyrophase and pitch angles and integrated in the region of

the described conditions. The presentation of the final results is delayed until the next section, where the comparison between the observed and simulated data will be compared in detail.

5.6 The Observed and Simulated Particle Anisotropies

The plasma frame fluxes, in each of the 8 sectors of each PL0 energy channel, were calculated from the observed spacecraft frame fluxes via equation 5.14. The channel midpoint gammas, as discussed in chapter 4, were used in the transformation procedure. The results of these transformations are presented in two distinct formats: particle pitch angle distributions and particle anisotropy plots.

Pitch angle distributions indicate the particle flux detected as a function of their pitch angle. Figures 5.4 and 5.5 present the pitch angle distributions of the original LEMPA data, the transformed data, as well as that from the simulation for two locations corresponding to 3 and 2 hours before the suspected shock passage. The fraction of the total amount of detected particles is plotted on the ordinate. Figures 5.6 and 5.7 present the same for regions corresponding to 1 and 2 hours after the suspected shock passage.

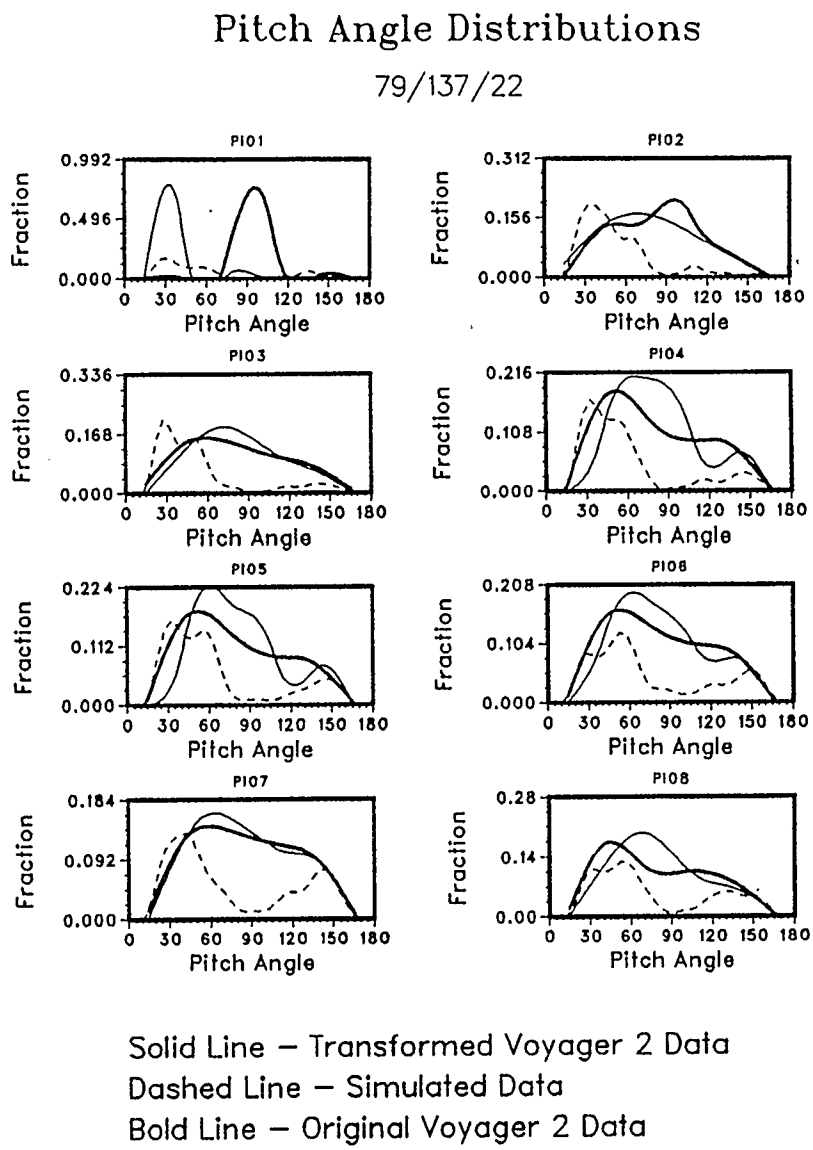

Figure 5.4: Pitch Angle Distributions: PL0 Channels, 79/137/22
Indicated are the upstream pitch angle distributions of the original one hour averaged Voyager 2 data (bold line), the transformed data (solid line), and the simulated data (dashed line) for a time corresponding to 3 hours before the shock passage. The relative fraction of detected particles is plotted on the ordinate as a function of the LSP frame pitch angles. Pitch angles less than 90° correspond to an anti-shockward current.

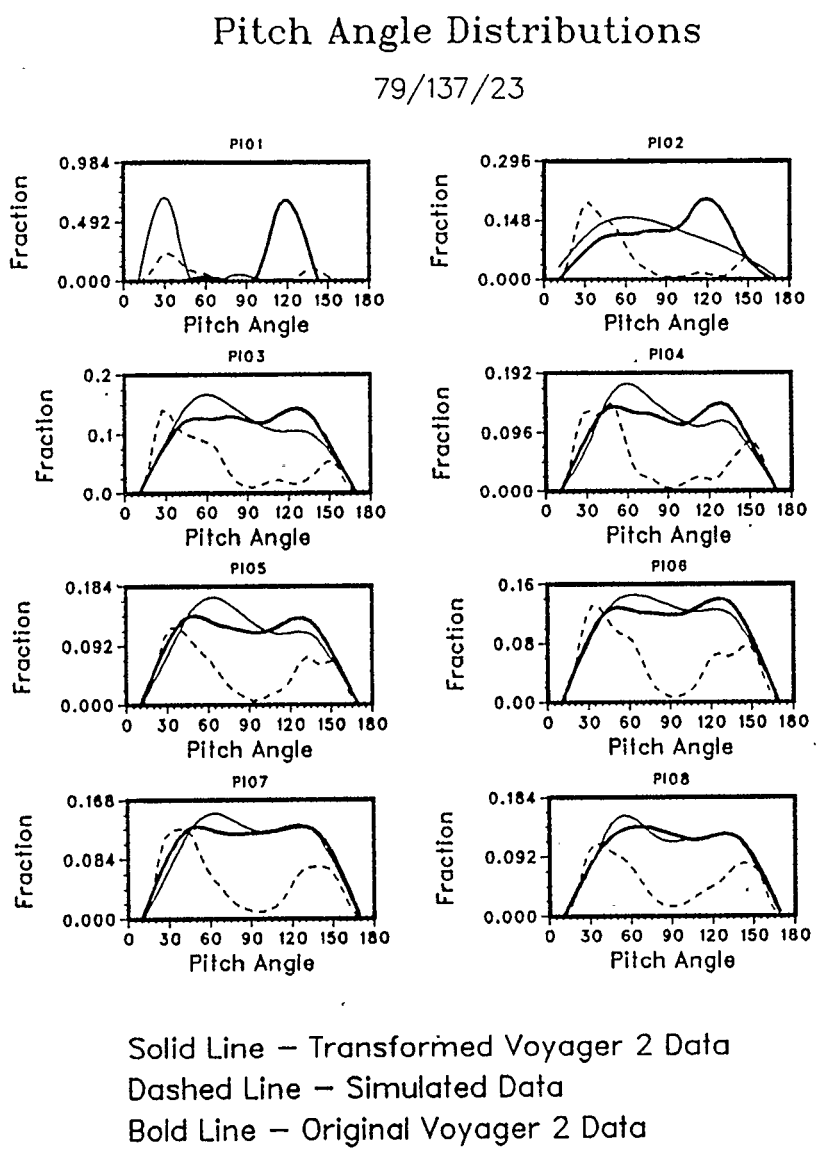

Figure 5.5: Pitch Angle Distributions: PL0 Channels, 79/137/23
Indicated are the upstream pitch angle distributions of the original one hour averaged Voyager 2 data (bold line), the transformed data (solid line), and the simulated data (dashed line) for a time corresponding to 2 hours before the shock passage. The relative fraction of detected particles is plotted on the ordinate as a function of the LSP frame pitch angles. Pitch angles less than 90° correspond to an anti-shockward current.

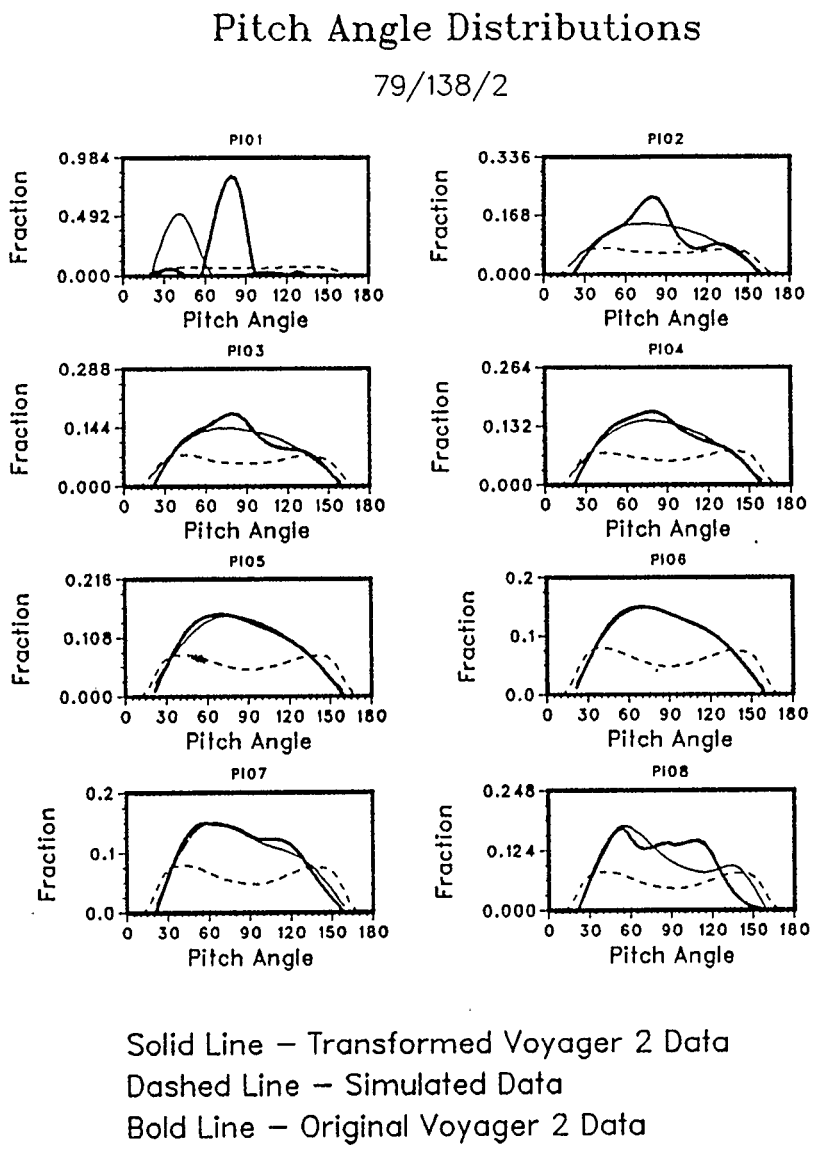

Figure 5.6: Pitch Angle Distributions: PL0 Channels, 79/138/02
Indicated are the downstream pitch angle distributions of the original one hour averaged Voyager 2 data (bold line), the transformed data (solid line), and the simulated data (dashed line) for a time corresponding to 1 hour after the shock passage. The relative fraction of detected particles is plotted on the ordinate as a function of the LSP frame pitch angles. Contrary to the upstream case, pitch angles greater than 90° correspond to an anti-shockward current.

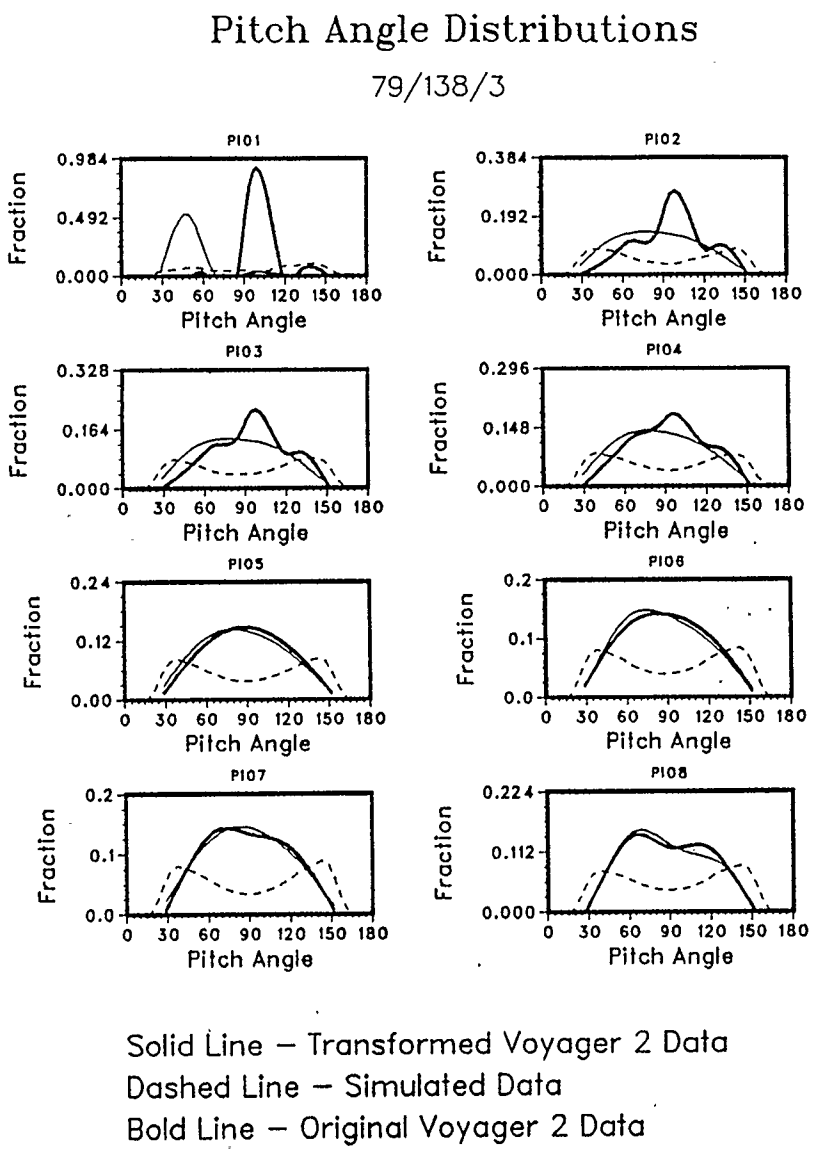

Figure 5.7: Pitch Angle Distributions: PL0 Channels, 79/138/03
Indicated are the downstream pitch angle distributions of the original one hour averaged Voyager 2 data (bold line), the transformed data (solid line), and the simulated data (dashed line) for a time corresponding to 2 hours after the shock passage. The relative fraction of detected particles is plotted on the ordinate as a function of the LSP frame pitch angles. Contrary to the upstream case, pitch angles greater than 90° correspond to an anti-shockward current.

In applying the Compton-Getting transformation it was assumed, for simplicity, that all particles detected within a particular sector had the same pitch angle and had a trajectory coincident with the axis of the conical sector. That is, the LSP altitude angle of the particle trajectory was zero and the azimuthal angle differed from that of the particular sector by 180°. As sector 8 was covered by a calibration target/sun shield, it was necessary to interpolate its incident flux from the values in the nearest sectors. A spline interpolation was employed which utilized the values of the fluxes of surrounding sectors 6, 7, 1, and 2. The procedure used is presented by Press et al., *(1987)*.

Recall from chapter 4 that the one hour averaged PL01 data was unfortunately not available for the energy spectra determinations, and thus a value of the PL01 channel midpoint spectral index was not calculated. However, the sectored PL01 data was available. As a result, for the purposes of the PL01 transformation, the value of the spectral index calculated for PL02 was used. This is not expected to be an unreasonable assumption for an energy spectrum with no apparent fold-over at the lower energies, as is the case here as demonstrated in chapter 4.

The particle anisotropy diagrams, Figures 5.8 to 5.11, indicate the flux into each sector at each energy for the same time periods of the pitch angle distributions. The sectors are as shown in figure 5.1, the positive x-axis of the LSP frame bisecting sector 8. The relative value of the incident flux is proportional to the radial amplitude of the arc sector in each sector. While the two varieties of diagrams contain basically the same information, each has its own advantage. The pitch angle distributions demonstrate the anti-shockward particle flow (once the upstream field polarity is recognized, $\lambda_B \sim 90°$ for the present case) while the

anisotropy plots provide a better visualization of the particle flux in each sector.

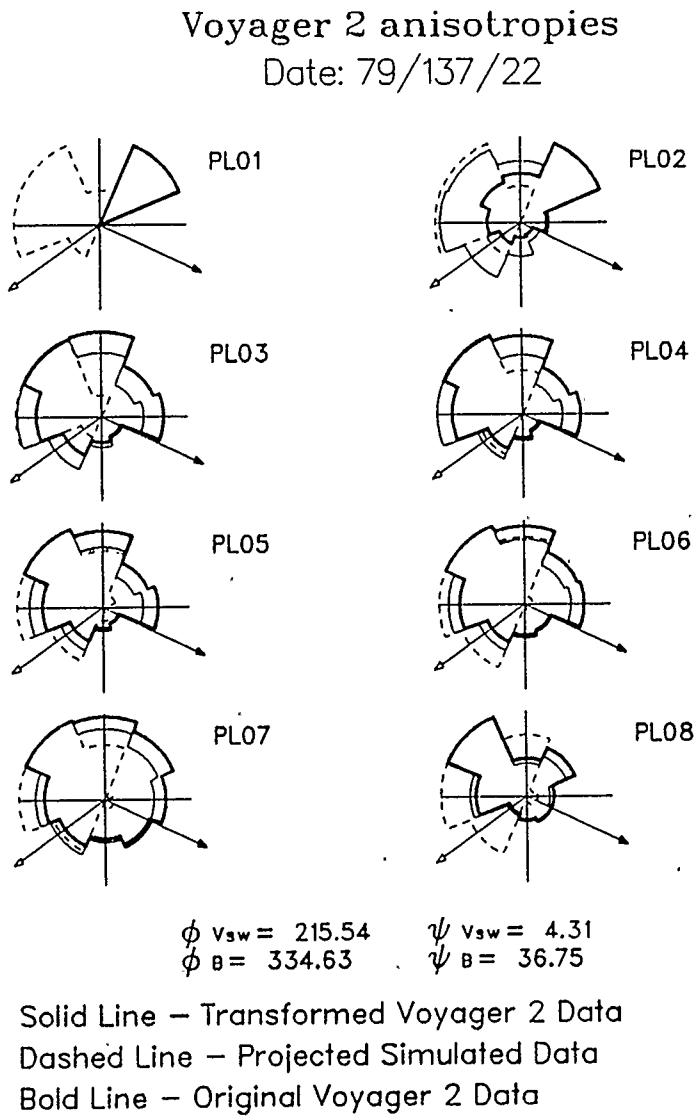

Figure 5.8: Particle Anisotropy Plot: PL0 Channels, 79/137/22

Indicated are the upstream particle anisotropy plots of the original one hour averaged Voyager 2 data (bold line), the transformed data (solid line), and the simulated data (dashed line) for a time corresponding to 3 hours before the shock passage. The relative fraction of detected particles into each sector of the LSP is indicated, the radial amplitude per sector being proportional to the incident flux. The LSP projections of the IMF and (helioradial) solar wind velocity vectors are indicated for reference.

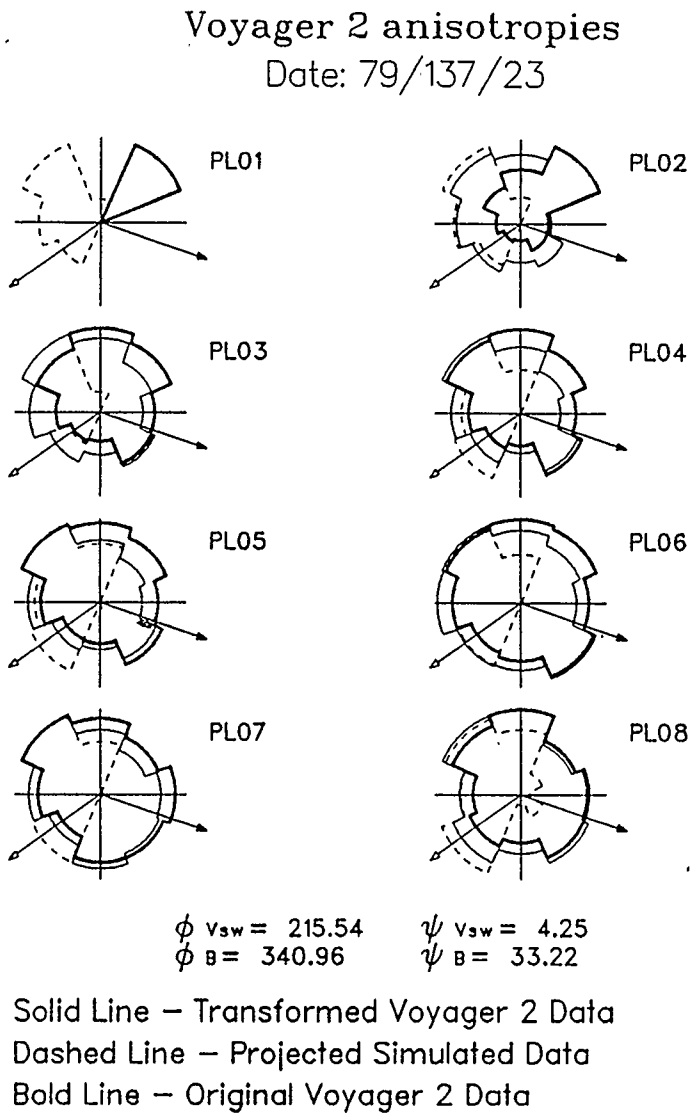

Figure 5.9: Particle Anisotropy Plot: PL0 Channels, 79/137/23
Indicated are the upstream particle anisotropy plots of the original one hour averaged Voyager 2 data (bold line), the transformed data (solid line), and the simulated data (dashed line) for a time corresponding to 2 hours before the shock passage. The relative fraction of detected particles into each sector of the LSP is indicated, the radial amplitude per sector being proportional to the incident flux. The LSP projections of the IMF and (helioradial) solar wind velocity vectors are indicated for reference.

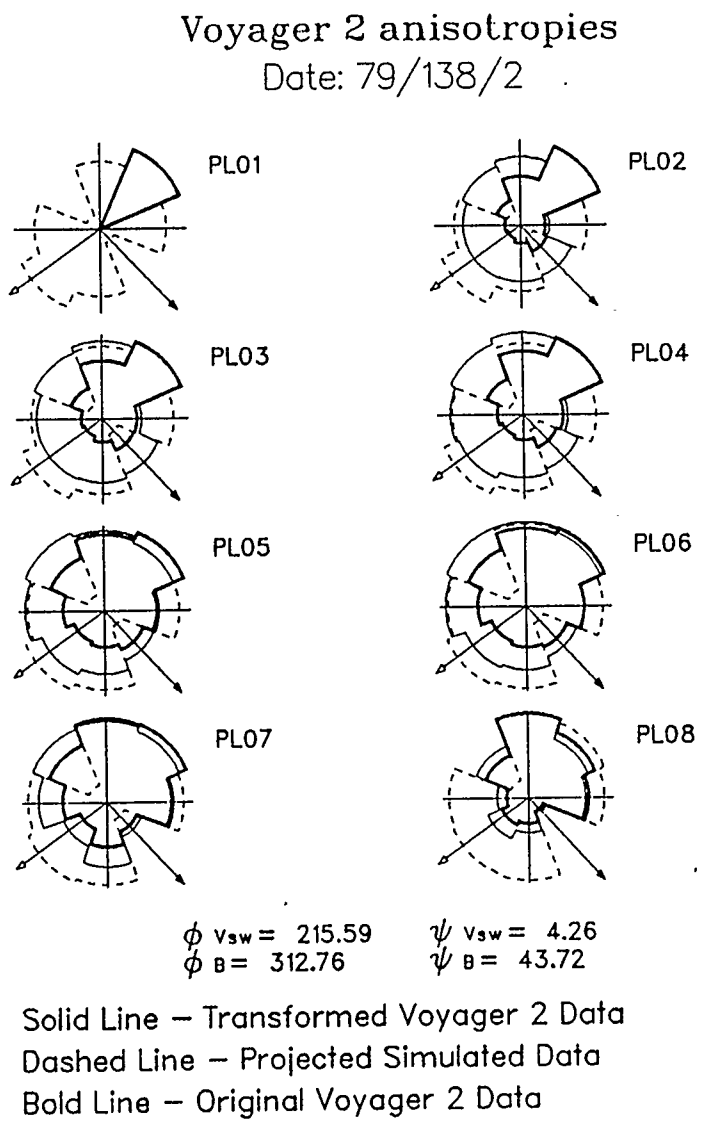

Figure 5.10: Particle Anisotropy Plot: PL0 Channels, 79/138/02

Indicated are the downstream particle anisotropy plots of the original one hour averaged Voyager 2 data (bold line), the transformed data (solid line), and the simulated data (dashed line) for a time corresponding to 1 hour after the shock passage. The relative fraction of detected particles into each sector of the LSP is indicated, the radial amplitude per sector being proportional to the incident flux. The LSP projections of the IMF and (helioradial) solar wind velocity vectors are indicated for reference.

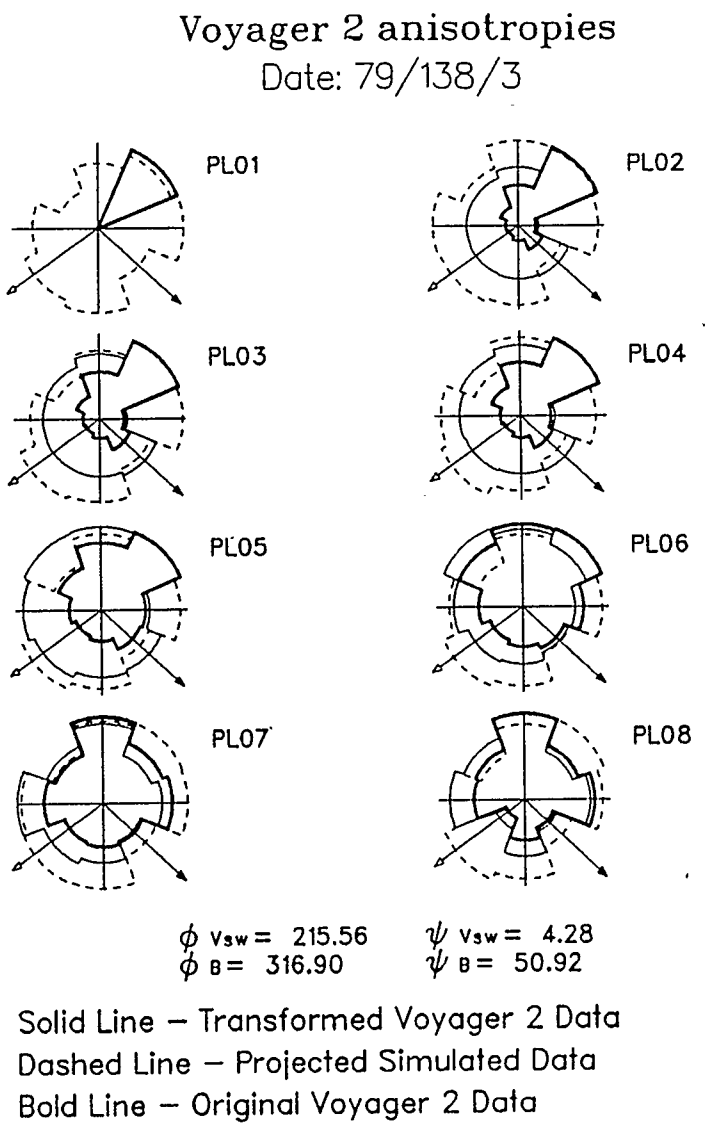

Figure 5.11: Particle Anisotropy Plot: PL0 Channels, 79/138/03

Indicated are the downstream particle anisotropy plots of the original one hour averaged Voyager 2 data (bold line), the transformed data (solid line), and the simulated data (dashed line) for a time corresponding to 2 hours after the shock passage. The relative fraction of detected particles into each sector of the LSP is indicated, the radial amplitude per sector being proportional to the incident flux. The LSP projections of the IMF and (helioradial) solar wind velocity vectors are indicated for reference.

Some explanation is required regarding the representation of the simulated data in Figures 5.8 to 5.11. A physical restriction is imposed upon the observed data that the simulated data is not subject to. The larger the value of ψ_B, the altitude angle of the IMF vector measured from the LSP, the higher is the relative fraction of particles whose observed pitch angle is near or is at 90°. In this case, the observed data appears void of pitch angles near the extreme values of 0° or 180°. This does not imply a true absence of pitch angles near the extreme values, only the inability of the coplanar sectors to detect them. The simulation provides pitch angles over the full possible range from 0° to 180°, ignorant of the physical restrictions imposed upon the observed data due to the spacecraft design.

A procedure has been designed which *projects* the simulated data onto the LSP, effectively inflicting the same restriction and allowing a direct comparison of the observed and simulated anisotropies to be more meaningful. This procedure is outlined briefly.

The IMF unit vector and the unit vector of a particle incident into a sector whose azimuthal angle is ϕ_k ($\phi_k = n\pi/4, n = 1,\ldots,8$) are given by, in the LSP frame:

$$\hat{B} = \hat{x}\cos\phi_B\cos\psi_B + \hat{y}\sin\phi_B\cos\psi_B + \hat{z}\sin\psi_B \tag{5.30}$$

and,

$$\hat{v} = -\left[\hat{x}\cos\phi_k + \hat{y}\sin\phi_k\right] \tag{5.31}$$

The cosine of the angle between $\hat{B}$ and $\hat{v}$, that is, the cosine of the pitch angle

α is given by:

$$\cos\alpha = -\left[\cos\phi_k \hat{B}\cdot\hat{x} + \sin\phi_k \hat{B}\cdot\hat{y}\right] \tag{5.32}$$

where,

$$\hat{B}\cdot\hat{x} = \cos\phi_B \cos\psi_B$$

$$\hat{B}\cdot\hat{y} = \sin\phi_B \cos\psi_B$$

Combining these equations and simplifying,

$$\cos\alpha = -\cos\psi_B \left[\cos\left(\phi_B - \phi_k\right)\right]$$

Solving for ϕ_k,

$$\phi_k = \phi_B \pm \cos^{-1}\left(\frac{-\cos\alpha}{\cos\psi_B}\right) \tag{5.33}$$

Equation 5.33 provides the allowable value(s) for the LSP azimuthal angle of a simulated particle into a particular sector for a given IMF vector and pitch angle. The physical restriction is observed mathematically as the argument of the inverse cosine function. For a given ψ_B, any α such that $\mid(-\cos\alpha/\cos\psi_B)\mid > 1$ implies that value of α could not have been observed by the detector. Thus the simulated data is projected onto the LSP by determining the cutoff pitch angles implied by equation 5.33. For example, for $\psi_B = 43°$ it is seen that $43° < \alpha < 137°$. This, of course, neglects any finite look angle of the sectors, which for the LEMPA is 45°.

The allowable values of the pitch angles resulted in the ϕ_k values as given by equation 5.33 which are those presented in Figures 5.8 to 5.11. There is an imposed

reflectional symmetry about the IMF vector as a result of the single-valued inverse cosine function. The inverse cosine function returns only values of an angle between 0° and 180°, which could be on either side of the IMF vector in the LSP. As a result, the single-sided fluxes were reflected about the IMF vector and binned into the appropriate LSP sectors.

5.6.1 Spearman Rank-Order Correlation

In order to quantify the comparison between the observed and simulated relative fluxes presented in Figures 5.4 to 5.7, a correlation statistic is used. It is possible to *invert* the pitch angle distribution diagrams and plot, at the common pitch angles, the simulated relative flux versus the observed relative flux. If the simulated and observed fluxes were identical at all pitch angles, the data points would be linear and the slope of the line would be unity. Figure 5.12 is an example of such a diagram.

It is seen that there is considerable scatter in the data in Figure 5.12. The slope of the least-squares best fit to the data is 0.986. The linear correlation coefficient, r, for some pair of data sets (x_i, y_i) with means $\bar{x}$ and $\bar{y}$ is given by *(Press et al., 1987)*,

$$r = \frac{\sum_i (x_i - \bar{x})(y_i - \bar{y})}{\sqrt{\sum_i (x_i - \bar{x})^2}\sqrt{\sum_i (y_i - \bar{y})^2}} \tag{5.34}$$

and equals 0.711 for the data in Figure 5.12. However, as pointed out by Press et al. *(1987)*, the statistic r is a poor indicator of how statistically significant the correlation really is. This is because r is calculated without any respect to the

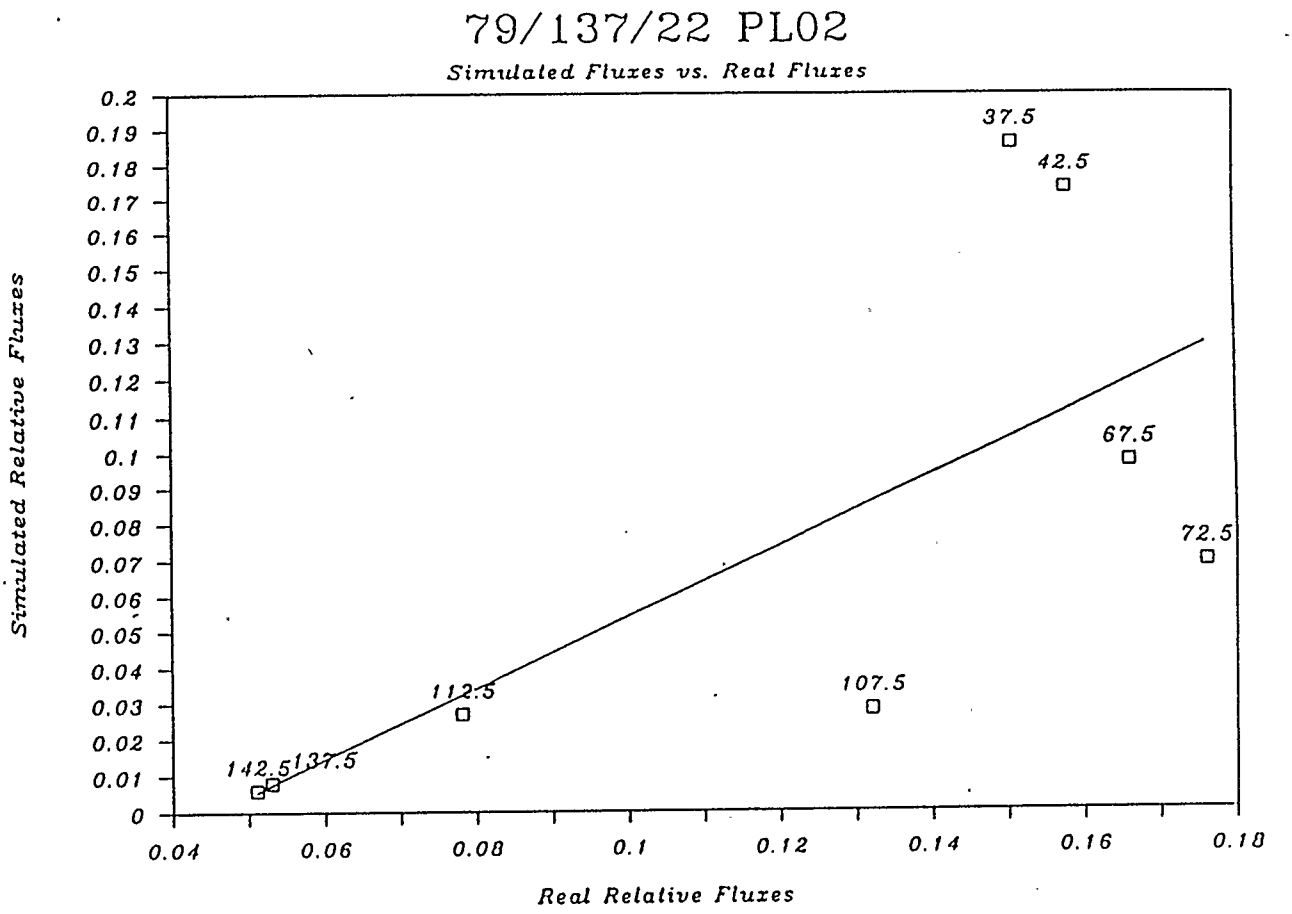

Figure 5.12: The Simulated versus Observed Flux: 79/137/22 PL02
At each of the eight common pitch angles the simulated relative fluxes are plotted versus the observed relative fluxes. The pitch angle represented by each of the data points is indicated in the diagram. For exact correlation between the simulated and observed fluxes at each pitch angle, all data points would lie along the line whose slope equals one. The line indicated is the least-squares linear regression fit.

individual distributions of the data set x_i and y_i.

A better, more robust statistic can be evaluated which better indicates the correlation between the two sets of fluxes. This statistic is referred to as the Spearman rank-order correlation coefficient, r_s, and is simply the linear correlation coefficient of the ranks of the data set. A data set x_i is replaced by its rankings R_i and the set y_i by its rankings S_i. For example, if x_1 has the fourth smallest value among all the x_i, then R_1 equals four. In the case of a tie between two or more of the original data, the rank assigned to each member of the tied group is the mean of the ranks they would otherwise be assigned.

In the case of no ties in the original data, the value of r_s is given by *(Press et al., 1987)*,

$$r_s = 1 - \frac{6D}{N^3 - N} \tag{5.35}$$

where N is the total number of data pairs, and D is the sum of the square of the differences between the rankings,

$$D = \sum_{i=1}^{N} (R_i - S_i)^2 \tag{5.36}$$

When there are ties in the data, the expression for r_s is given by

$$r_s = \frac{1 - \frac{6}{N^3-N}\left[D + \frac{1}{2}\sum_k F_k + \frac{1}{2}\sum_m G_m\right]}{\left[1 - \frac{\sum_k F_k}{N^3-N}\right]\left[1 - \frac{\sum_m G_m}{N^3-N}\right]} \tag{5.37}$$

where $F_k = (f_k^3 - f_k)$ and $G_m = (g_m^3 - g_m)$, with f_k representing the number of ties in the kth group of ties among the ranked data R_i, and g_m representing the number of ties in the mth group of ties among the ranked data S_i.

The data indicated in Figures 5.4 through 5.7 was subjected to the Spearman rank-order correlation analysis and the results are presented in Table 5.3. The entries in the table are, for the corresponding time and energy band, the slope of the least-squares linear regression fit, m_r, the Spearman rank-order correlation coefficient, r_s, and the *significance level* of r_s. As indicated by Press et al. *(1987)*, the statistic r_s is approximately distributed as a Student's t-distribution with $N-2$ degrees of freedom. In this example, the two sets of data are consistent with one another.

5.6.2 Interpretation of the Correlation

From Figures 5.4 and 5.5 it is seen that there is a definite anti-shockward flow of the low energy particles upstream of the shock, consistent with that expected in the case of SDA. Pitch angles less than 90° in these diagrams correspond to particles flowing away from the shock, those greater than 90° correspond to particles flowing toward the shock. In the observed data, this upstream anti-shock anisotropy is seen to be larger at the lower energy, transformed data, especially at locations nearer to the shock. The bold line represents the original (spacecraft frame) data and is included in the pitch angle distribution diagrams to illustrate the effect of the Compton-Getting transformation upon the particle fluxes at the various energies. Generally, the upstream anti-shockward anisotropies seen in the simulated data are larger than those observed in the observed data.

Unexpectedly, there is observed a second *shockward* upstream anisotropy of smaller amplitude in both the observed and simulated data. The value of the pitch angle at which this second anisotropy is seen is at the approximate supplemen-

Time	Energy	m_r	r_s	Significance
79/137/22	PL01	0.162	0.548	0.159
	PL02	0.986	0.762	0.028
	PL03	-0.045	0.214	0.610
	PL04	0.082	0.452	0.260
	PL05	0.173	0.259	0.536
	PL06	0.163	0.262	0.531
	PL07	-0.057	-0.048	0.911
	PL08	0.231	0.567	0.143
79/137/23	PL01	0.257	0.445	0.269
	PL02	1.077	0.619	0.102
	PL03	0.363	0.262	0.531
	PL04	-0.253	-0.238	0.570
	PL05	-0.226	-0.143	0.736
	PL06	-0.728	-0.262	0.531
	PL07	-0.948	-0.524	0.182
	PL08	-0.249	-0.119	0.779
79/138/02	PL01	0.006	-0.049	0.909
	PL02	0.011	0.195	0.643
	PL03	-0.057	-0.235	0.575
	PL04	-0.150	-0.488	0.220
	PL05	-0.163	-0.355	0.388
	PL06	-0.142	-0.232	0.581
	PL07	0.033	0.042	0.921
	PL08	0.103	0.381	0.352
79/138/03	PL01	0.001	-0.319	0.441
	PL02	-0.005	0.119	0.779
	PL03	-0.227	-0.190	0.651
	PL04	-0.114	0.190	0.651
	PL05	-0.344	-0.572	0.138
	PL06	-0.278	-0.669	0.070
	PL07	-0.521	-0.886	0.003
	PL08	-0.093	-0.030	0.943

Table 5.3: The Comparison of the Observed and Simulated Data

The quantitative comparison of the observed, transformed angular Voyager 2 LECP data with that of the simulated data for the forward shock event F(2,1) is provided. Indicated is the regression slope of the observed versus simulated data, m_r, along with the Spearman rank-order correlation coefficient r_s. The last column is the t-distribution of r_s and indicates $(1-p)$, where p is the probability that the two data sets are statistically uncorrelated.

tary angle of that at which the main anisotropy occurs. For example, for a large anisotropic flux occurring at a pitch angle of $\sim 30°$, there is generally a second anisotropic flux observed at $\sim 150°$. It is noted that the relative amplitude of the second anisotropy in the simulated data increases at locations closer to the shock front, especially in the higher energy channels, whereas that of the observed data decreases. The significance of this is not yet fully understood.

Figures 5.6 to 5.7 indicate that downstream of the shock there is a particle flux peaked perpendicular to the mean IMF in the observed data, but there is generally no anisotropy observed in the simulated data. Small shockward ($\alpha < 90°$) flows exist initially in the observed data but fade at successive distances from the shock. The very large simulated anisotropies have disappeared, but there is still evidence of small shockward and anti-shockward fluxes.

The anisotropy plots provide a better indication of the effects of the Compton-Getting transformation upon the original Voyager 2 LEMPA data. Clearly, Figures 5.8 through 5.11 show that the sunward side sector, generally sector 1, is inundated with particles as a result of solar wind velocity. The large flux into sector 1 is observed in the original (bold line) data. The effects of the transformation procedure are first clearly seen in the PL02 energy range, both up and downstream of the shock. The large anisotropy due to the relative velocity of the plasma and the LSP frames of reference is removed.

The apparent lack of transformed data in the PL01 channel is misleading. The influx of particles into sector 1 at this energy range is so large that, by comparison, those of the other sectors are insignificantly small and do not appear on these diagrams. The flux into sector 1 of the PL01 channel is of the order of 10^3 times

that of the other sectors. Consequently, the transformation has little effect and the transformed data appears coincident with that of the original data.

The transformation procedure produces upstream anisotropy plots which appear semi-circular on the side of the LSP in which the LSP projection of the IMF vector enters. This is merely the indication of a field-aligned flow, without explicit reference to the location of the shock or value of the pitch angle. The second anisotropy, anti-parallel to the mean IMF, is observed as a non-negligible radial amplitude in the sector 180° from that in which the LSP projection of the IMF vector enters the LSP.

The downstream anisotropy plots indicate a larger flux into the sectors which are perpendicular to the LSP projection of the IMF vector in the observed data but a high degree of isotropy exists in the simulated data (except for the sectors removed as a result of the projection of the simulated data onto the LSP). If the value of ψ_B was zero, an exactly isotropic anisotropy plot would be a circle. For an anisotropy perpendicular to the mean IMF projection, the anisotropy plot would only contain sectors perpendicular to the LSP projection of the IMF vector.

The interpretation of the Spearman rank-order correlation coefficient must be performed with some care. It must be understood that such a correlation attempts to describe the relative association between the corresponding anisotropies between the observed and associated pitch angle data, if any exists. It is independent of the amplitude of the anisotropies, it only provides information between the location of the observed and simulated anisotropies. Examination of Table 5.3 indicates that the correlation between the two data sets is not *statistically* significant. Although the statistic r_s is described as a robust quantity, it is still somewhat sensitive to

slight shifts between the locations of the anisotropic peaks in Figures 5.4 to 5.7.

As an example of the sensitivity of r_s examine the PL03 energy bin of Figure 5.4. Unarguably, there is a similarity between the morphology in the profiles of the observed, transformed data and that of the simulated data. In both situations there appears a bimodal distribution with a large, primary peak in the $\alpha < 90°$ range and a smaller, secondary peak in the $\alpha > 90°$ range. However, the location of the maximum flux in the simulated data occurs at a slightly smaller pitch angle than does that for the observed, transformed data. This slight shift between the maxima of the distributions is felt in the ranking of the data prior to the calculation of r_s. It results in large terms in the evaluation of the quantity D in equation 5.36, which then produces a value of r_s which is too large, influencing the evaluation of the statistical significance.

The real utility of r_s lies in its ability to *confirm* the association between the simulated and observed data. The value of the slope of the least-squares regression fit between the two data sets at the common pitch angle can aid in the confirmation of the association, its ideal value being close to unity. However, a complete interpretation of the degree of association must include all bits of evidence; the pitch angle diagrams as well as the values of r_s and m_r.

It is obvious from this evidence that the lower energy ranges (PL01–PL04) are more effected by the acceleration due to the shock passage than are the higher energy ranges, in both the observed and simulated data. This is consistent with the energy spectra presented in chapter 4, where it was observed the particles whose energies were in the (at least) PL02–PL04 range were significantly affected by the shock passages. The value of r_s indicates that the association between the

simulated and observed data is much better at the lower energy ranges, especially upstream.

The fact that the simulated data's primary upstream anisotropy is much larger than that of the observed data is very likely due to the choice of wave activity in the vicinity of the shock. It has been shown *(Decker, 1985)* that the introduction of upstream wave activity reduces the particle anisotropies but does not eliminate them. This may suggest that a larger field variance could have been chosen for the simulation. The estimate of the field variance used was derived from the one-hour averaged Voyager data and perhaps was much larger in reality than that used.

The origin of the second shockward anisotropy, in both the observed and the simulated data, may be attributed to one of two causes. Firstly, the introduction of the upstream waves may have produced efficient magnetic scattering centres which provided the observed shockward flux of particles. In this case, there would be a true shockward current. Secondly, the field variance itself may have been responsible for the second observed anisotropy *(Decker, private communication, 1988)*. There may be enough of the perpendicular component of the IMF superimposed upon the mean value such that, momentarily, the total field may be quite different from that of the mean field. In this instance, the particle flux could be still be anti-shockward but the measured pitch angle would be approximately the supplement of that expected.

The largest dicrepancy between the observed and simulated data was the inability of the simulation to accurately predict the downstream anisotropies observed in the observed data. The source of this downstream anisotropy is from the particle's attempt to conserve its first adiabatic invariant across the shock front. As a

particle moves along its trajectory from one magnetic field to another of a higher magnitude (upstream to downstream for a fast-mode shock), it attempts to increase its value of its velocity component perpendicular to the magnetic field. This mechanism is not apparently reproduced in the simulation.

The simulation integrates the particle's equation of motion until a shock crossing is sensed (the value of x changes sign) and the particle's momentum and position at the shock are then tranformed into the new plasma frame and used as the initial conditions for the integration into the new field. The simulation generates the upstream and downstream fields independently and makes no attempt to match fields at the shock boundary. This discontinuity of the magnetic field at the shock and the injection procedure into the new field may be likely the reason the simulated particles are not observed to conserve their first adiabatic invariant. A new version of the simulation which does attempt to match the upstream and downstream fields at the shock has since been written *(Decker, 1987)*. Perhaps this new model feature can shed light upon the discrepancy found here.

Some fundamental differences between the simulated and observed events that could be cause for a discrepancy in their angular distributions should be noted here. In general, the flow of the upstream plasma into the shock front (in the shock frame) could have a component parallel to the shock front *(Decker, 1988)*. If so, the particle dynamics may have been slightly different in the observed event. Related to this is the value of $\vec{U}_1$ used in the simulation; its estimate was based upon a simplistic two-point observation of the event F(2,1) by both Voyager spacecraft, assuming that the shock travelled in the direction of its normal. A more complete data set could have provided a more accurate value of the shock speed and thus of

$\vec{U}_1$.

The simulated particles were injected isotropically upstream with discrete initial energies, those corresponding to the 8 lower energy passbands of detector alpha of the Voyager 2 LECP experiment. At 400 particles per energy passband, this corresponded to a flat input energy spectrum. This is only a crude approximation to reality, it is expected that the energy spectrum of low energy particles in the heliosphere is continuous, decreasing with increasing particle energy as in Figure 4.3.

Perhaps most importantly, it must be noted that the observed data is presented in the co-moving plasma frame while the simulated data is presented in the shock frame. The velocity of the upstream plasma frame with respect to the shock frame is $\vec{U}_1 = 60$ km/s and that of the downstream plasma frame with respect to the shock frame is $\vec{U}_2 = 27.7$ km/s. The transformation velocity between the two frames, $\vec{U}_1$ or $\vec{U}_2$, is insignificant compared to the velocity of even the lowest energy particles and therefore can be safely neglected. It is interesting to note that the transformation of the simulated particles into the upstream plasma frame would result in even larger anisotropies, possibly indicating again that too small an upstream field variance was provided to the simulation.

5.7 Summary

This thesis has been concerned with the acceleration of low energy charged particles by fast mode magnetohydrodynamic corotating heliospheric shock waves. Chapter one presented the physical description of the heliosphere as well as the basic physics

describing the modulation of cosmic rays. This material served as a background for the later chapters.

Chapter two discussed the phenomenon of MHD waves in a plasma. The macroscopic plasma properties upstream of the shock were seen to be related to those downstream by the use of the magnetic Rankine-Hugoniot equations; for a given set of upstream parameters $(\vec{B}_1, \theta_{Bn}, \vec{U}_1, Ma_1)$, the corresponding quantities downstream were found. Techniques used in the inference of shock geometries were presented, and it was found that the actual technique to be used was dictated by the available data. Finally, the two major mechanisms of particle acceleration at shocks, shock drift acceleration and the Fermi mechanism, were introduced.

The available Voyager 1 and 2 magnetic field and plasma data presented in chapter three suggest the recurrence of 2 corotating interaction regions three times during the time interval DOY 100–180, 1979. Features associated with the detection of corotating interaction regions are identified in the plasma and field data of the Voyager spacecraft (primarily Voyager 2). Evidence presented indicating the recurrence of two forward and reverse shock pairs includes: a test of periodicity, the effect upon the field and plasma data at both spacecraft, the width of the CIR's as a function of time and radial distance, and a test of the relative field variance within the presumed CIR's. Finally, the shock geometries as defined by the single parameter θ_{Bn} are presented for each occurrence of the expected shocks.

Chapter four indicated that the evolution of the low energy particle spectrum as recorded by the Low Energy Charged Particle experiment aboard Voyager 2 during the data interval of concern is consistent with particle acceleration at the location of the shock passages. A significant rise in the particle fluxes is a direct

result of energization within the ~30–4000 keV/nucleon range. Acceleration below ~200 keV was seen to be particularly evident.

It was seen in chapter five that the angular distributions of the plasma frame low energy particles in the vicinity of the event F(2,1) were seen to be consistent with the theory of SDA. Upstream of the shock there existed large anti-shockward particle anisotropies while downstream the anisotropies had shifted to perpendicular to the mean field. The presence of magnetic field fluctuations implied the probability of particle acceleration by the Fermi mechanism, but it was seen that the particle anisotropies thought indicative of SDA were still very evident.

In addition to the observed Voyager 2 angular distributions the results of a particle acceleration simulation were also presented in chapter five. The model parameters were chosen to coincide with those describing the conditions prevalent in the locale of the observed forward shock event F(2,1). The results of the simulated anisotropies upstream of the shock were consistent with those observed in the Voyager 2 data, particularly at the lower energy ranges of less than ~200 keV. The simulated upstream anisotropies were larger than those observed, however. Downstream, the simulation failed to produce significant field-perpendicular anisotropies.

As indicated by Armstrong et al. *(1984)*, all available data should be considered in the recognition of an acceleration region in the heliosphere: particle intensity profiles, particle energy spectra, magnetic field and plasma data, as well as the angular distributions of the particles in the shock vicinity. It can be concluded, based upon the evidence presented in this thesis, that significant low energy particle energization is occurring at the regions occupied by fast mode MHD corotating

shock waves in the heliosphere.

Bibliography

Abraham-Shrauner, B., Determination of Magnetohydrodynamic Shock Normals, *J. Geophys. Res.*, **77**, 736, 1972.

Abraham-Shrauner, B., S.H. Yin, Interplanetary Shocks Seen by Ames Plasma Probe on Pioneer 6 and 7, *J. Geophys. Res.*, **81**, 2097, 1976.

Armstrong, T.P., G. Chen, E.T. Sarris, S.M. Krimigis, Acceleration and Modulation of Electrons and Ions by Propagating Interplanetary Shocks, *Study of Interplanetary Traveling Phenomena (STIP)*, eds. M.A. Shea, D.F. Smart, S.T. Wu, D. Reidel Publishing Co., 367, 1977.

Armstrong, T.P., M.E. Pesses, R.B. Decker, Shock Drift Acceleration, *Collisionless Shocks in the Heliosphere: Reviews of Current Research*, eds. B.T. Tsurutani, R.G. Stone, American Geophysical Union, Washington, D.C., 1985.

Axford, W.I., The Three Dimensional Structure of the Interplanetary Medium, *Study of Traveling Interplanetary Phenomena (STIP)*, eds. M.A. Shea, D.F. Smart, S.T. Wu, D. Reidel Publishing Co., 145, 1977.

Axford, W.I., The Acceleration of Galactic Cosmic Rays, *The Origin of Cosmic Rays*, eds. G. Setti, G. Spada, A.W. Wolfendale, 339, 1981.

Balogh, A., G. Erdös, The Energy Spectrum of 35-1000 keV Protons in Shock Associated Events, *Proc. Int. Conf. Cosmic Rays 17th*, 1981.

Barnes, C.W., Hydrodynamic Waves in the Interplanetary Medium, *Solar-Terrestral Physics*, Carovillano, R.L., J.M. Forbes, eds., D. Reidel Publishing Co., **104**, 1983.

Barnes, C.W., J.A. Simpson, Evidence for Interplanetary Acceleration of Nucleons in Corotating Interaction Regions, *Ap. J.*, **210**, L91, 1976.

Bell, A.R., The Acceleration of Cosmic Rays in Shock Fronts - I, *Mon. Not. R. astr. Soc.*, **182**, 147, 1978.

Bell, A.R., The Acceleration of Cosmic Rays in Shock Fronts - II, *Mon. Not. R. astr. Soc.*, **182**, 443, 1978.

Birdsall, C.K., A.B. Langdon, *Plasma Simulation via Computer Simulation*, McGraw Hill Book Co., Toronto, 1985.

Blandford, R.D., Fermi Acceleration by Shock Waves, *A.I.P. Conf. Proc. No. 56*, eds. J. Arens, C. Max, C. McKee (American Institute of Physics), 1979.

Blandford, R.D., J.P. Ostriker, Particle Acceleration by Astrophysical Shocks, *Ap. J.*, **221**, L29, 1978.

Boyd, T.J.M., J.J. Sanderson, *Plasma Dynamics*, Barnes and Noble, Inc., New York, 1969.

Burlaga, L., Hydromagnetic Waves and Discontinuities in the Solar Wind, *Space Sci. Rev.*, **12**, 600, 1971.

Burlaga, L., MHD Processes in the Outer Heliosphere, *NASA Technical Memorandum 86137*, August 1984.

Chao, J.K., Y.H. Chen, On the Distribution of θ_{Bn} for Shocks in the Solar Wind, *J. Geophys. Res.*, **90**, 149, 1985.

Chen, F., *Introduction to Plasma Physics*, Plenum Press, New York, 1984.

Christon, S.P., On the Origin of the MeV Energy Nucleon Flux Associated with CIRs, *J. Geophys. Res.*, **86**, 8852, 1981.

Colburn, D.S., C.P. Sonett, Discontinuities in the Solar Wind, *Space Sci. Rev.*, **5**, 439, 1966.

Compton, A.H., I.A. Getting, An Apparent Effect of Galactic Rotation on the Intensity of Cosmic Rays, *Phys. Rev.*, **47**, 817, 1935.

Decker, R.B., The Modulation of Low-Energy Proton Distributions by Propagating Interplanetary Shock Waves: A Numerical Simulation, *J. Geophys. Res.*, **86**, 4537, 1981.

Decker, R.B., Formation of Shock-Spike Events at Quasi-Perpendicular Shocks, *J. Geophys. Res.*, **88**, 9959, 1983.

Decker, R.B., The Role of Drifts in Diffusive Shock Acceleration, APL Preprint submitted to *Ap. J.*, June 1987.

Decker, R.B., Computer Modeling of Test Particle Acceleration at Oblique Shocks, APL Preprint submitted to *Sp. Sci. Rev.*, 1988.

Decker, R.B., M.E. Pesses, S.M. Krimigis, Shock-Associated Low-Energy Ion Enhancements Observed by Voyagers 1 and 2, *J. Geophys. Res.*, **86**, 8819, 1981.

Decker, R.B., L. Vlahos, Shock Drift Acceleration in the Presence of Waves, *J. Geophys. Res.*, **90**, 47, 1985.

Decker, R.B., L. Vlahos, Modeling of Ion Acceleration Through Drift and Diffusion at Interplanetary Shocks, APL Preprint, Submitted to *J. Geophys. Res.* March 1986a.

Decker, R.B., L. Vlahos, Numerical Studies of Particle Acceleration at Turbulent, Oblique Shocks with an Application to Prompt Ion Acceleration During Solar Flares, APL Preprint, Accepted for Publication in *Ap. J.*, July 1986b.

deHoffmann, F., E. Teller, Magneto-Hydrodynamic Shocks, *Phys. Rev.*, **80**, 692, 1950.

Dorman, L.I., *Cosmic Rays, Variations and Space Explorations*, American Elsevier Publishing Co. Inc., New York, 1974.

Fisk, L.A., Solar Modulation of Galactic Cosmic Rays, 2, *J. Geophys. Res.*, **76**, 221, 1971.

Fisk, L.A., Solar Modulation High Energy Particles and Quanta in Astrophysics, McDonald, F.B., C.E. Fichtel, eds., D. Reidel Publishing Co., 1974.

Fisk, L.A., Solar Cosmic Rays - Their Injection, Acceleration, and Propagation, *Solar-Terrestrial Physics*, Carovillano, R.L., J.M. Forbes, eds., D. Reidel Publishing Co., **104**, 1983a.

Fisk, L.A., Solar Modulation of Galactic Cosmic Rays, *Solar-Terrestrial Physics*, Carovillano, R.L., J.M. Forbes, eds., D. Reidel Publishing Co., **104**, 1983b.

Fisk, L.A., The Acceleration of Energetic Particles in the Solar Wind, *Solar-Terrestrial Physics*, Carovillano, R.L., J.M. Forbes, eds., D. Reidel Publishing Co., **104**, 1983c.

Fisk, L.A., M.A. Lee, Shock Acceleration of Energetic Particles in Corotating Interaction Regions in the Solar Wind, *Ap. J.*, **237**, 620, 1980.

Forman, M.A., The Compton-Getting Effect for Cosmic-Ray Particles and Photons and the Lorentz-Invariance of Distribution Functions, *Planet. Space Sci.*, **18**, 25, 1970.

Forman, M.A., G.M. Webb, Acceleration of Energetic Particles, *Collisionless Shocks in the Heliosphere: A Tutorial Review*, eds. R.G. Stone, B.T. Tsurutani, American Geophysical Union, Washington, D.C., 1985.

Gazis, P.R., A.J. Lazarus, The Radial Evolution of the Solar Wind, 1-10 A.U., *Solar Wind 5, NASA Conf. Publ. CP-2280*, 509, 1983.

Gazis, P.R., A.J. Lazarus, K. Hester, Shock Evolution in the Outer Heliosphere: Voyager and Pioneer Observations, *J. Geophys. Res.*, **90**, 9454, 1985.

Gibson, E., *The Quiet Sun*, NASA Scientific and Technical Information Office, 1973.

Gleeson, L.J., G.M. Webb, The Propagation of Cosmic-Rays in the Interplanetary Region, *Fundamentals of Cosmic Physics*, Vol. 6, 187, 1980.

Gleeson, L.J., I. Axford, *Ap. J.*, bf 154, 1011, 1968.

Gold, R.E., C.O. Bostrom, E.C. Roelof, D.J. Williams, Anisotropy Measurements of $\approx$ 50 keV Solar Protons, *Cont. Intl. Cosmic Ray Conf. 14th*, 1975.

Goldstein, H., *Classical Mechanics*, 2nd edition, Addison-Wesley, Reading, Mass., 1980.

Goldstein, M.L., L.F. Burlaga, W.H. Matthaeus, Power Spectral Signatures of Interplanetary Corotating and Transient Flows, *NASA Technical Memorandum 86051*, January 1984.

Goodrich, C., Numerical Simulations of Quasi-Perpendicular Collisionless Shocks, *Collisionless Shocks in the Heliosphere: Reviews of Current Research*, eds. B. T. Tsurutani, R. G. Stone, American Geophysical Union, Washington, D.C., 1985.

Hedgcock, P.C., Measurements of the IMF in Relation to the Modulation of Cosmic Rays, *Solar Phys.*, **42**, 497, 1975.

Holt, E.H., R.E. Haskell, *Foundations of Plasma Dynamics*, MacMillan, New York, 1965.

Hundhausen, A.J., Some Macroscopic Properties of Shock Waves in the Heliosphere, *Collisionless Shocks in the Heliosphere: A Tutorial Review*, eds. R.G. Stone, B.T. Tsurutani, American Geophysical Union, Washington, D.C., 1985.

Hundhausen, A.J., L.F. Burlaga, A Model for the Origin of Solar Wind Stream Interfaces, *J. Geophys. Res.*, **80**, 1845, 1975.

Ipavitch, F.M., The Compton-Getting Effect for Low Energy Particles, *Geophys. Res. Lett.*, **1**, 149, 1974.

Jokipii, J.R., Propagation of Cosmic Rays in the Solar Wind, *Rev. Geophys. Sp. Sci.*, **9**, 27, 1971.

Jokipii, J.R., Particle Drift, Diffusion, and Acceleration at Shocks, *Ap. J.*, **255**, 716, 1982.

Jokipii, J.R., A. Morfill, On the Origin of High-Energy Cosmic Rays, *Ap. J.*, **290**, L1, 1985.

Kalikhman, L.E., *Elements of Magnetogasdynamics* (chapter 7), eds. A.G.W. Cameron, W.B. Saunders Co., Philadelphia, 1967.

Kennel, C.F., F.L. Scarf, F.V. Coroniti, C.T. Russell, K.-P. Wenzel, T.R. Sanderson, P. van Nes, W.C. Feldman, G.K. Parks, E.J. Smith, B.T. Tsurutani, F.S. Mozer, M. Temerin, R.R. Anderson, J.D. Scudder, M. Scholer, Plasma and Energetic Particle Structure Upstream of a Quasi-Parallel Interplanetary Shock, *J. Geophys. Res.*, **89**, 5419, 1984a.

Kennel, C.F., J.P. Edmiston, F.L. Scarf, F.V. Coroniti, C.T. Russel E.J. Smith, B.T. Tsurutani, J.D. Scudder, W.C. Feldman, R.R. Anderson, F.S. Mozer, M. Temerin, Structure of the November 12, 1978, Quasi-Parallel Interplanetary Shock, *J. Geophys. Res.*, **89**, 5436, 1984b.

Kessel, R.L., *Gone With the Solar Wind: A Study of Protons Accelerated by Interplanetary Shocks*, Ph.D. Thesis, Univ. of Kans., Lawrence, 1986.

Kohlhase, C.E., P.A. Penzo, Voyager Mission and Description, *Space Sci. Rev.*, **21**, 77, 101, 1977.

Krimigis, S.M., Observations of Energetic Ions and Electrons at Interplanetary Shocks and Upstream of Planetary Bow Shocks by the Voyager Spacecraft, *Proc. of Intl. Sym. on Collisionless Shocks*, 1987.

Krimigis, S.M., T.P. Armstrong, W.I. Axford, C.O. Bostrom, C.Y. Fan, G. Gloeckler, L. Lanzerotti, The Low Energy Charged Particle (LECP) Experiment on the Voyager Spacecraft, *Space Sci. Rev.*, **21**, 329, 1977.

Krimigis, S.M., D. Venkatesan, In Situ Acceleration and Gradients of Charged Particles in the Outer Solar System Observed by the Voyager Spacecraft, *Astrophysics and Space Science*, **144**, 463, 1988.

Lee, M.A., L.A. Fisk, Shock Acceleration of Energetic Particles in the Heliosphere, *Space Sci. Rev.*, **32**, 205, 1982.

Lee, M.A., Coupled Hydromagnetic Wave Excitation and Ion Acceleration at Interplanetary Traveling Shocks, *J. Geophys. Res.*, **88**, 6109, 1983.

Lepping, R.P., P.D. Argentiero, Single Spacecraft Method of Estimating Shock Normals, *J. Geophys. Rev.*, **76**, 4349, 1971.

McDonald, F.B., B.J. Teegarden, J.H. Trainer, T.T. von Rosenvinge, W.R. Webber, The Interplanetary Acceleration of Energetic Nucleons, *Ap. J.*, **203**, L149, 1976.

McDonald, F.B., J.H. Trainer, J.D. Mihalov, J.H. Wolfe, W. R. Webber, Radially Propagating Shock Waves in the Outer Heliosphere: The Evidence From Pioneer 10 Energetic Particle and Plasma Observations, *Ap. J.*, **246**, L165, 1981.

McQuarrie, D. A., *Statistical Mechanics*, Harper & Row, New York, 1976.

Murtha, J.M., *Cosmic Rays and their Time and Spatial Variations*, University of Calgary Physics 598 Report (Independant Study), 1986.

Nicholson, D.R., *Introduction to Plasma Theory*, John Wiley & Sons, Toronto, 1983.

Ng, C.K., Coronal and Interplanetary Propagation, Interplanetary Acceleration, Cosmic-Ray Observations by Deep Space Network, and Anomalous Component, *Proc. Int. Conf. Cosmic Rays 19th*, 1985.

O'C Drury, L., An Introduction to the Theory of Diffusive Shock Acceleration of Energetic Particles in Tenuous Plasmas, *Rep. Prog. Phys.*, **46**, 973, 1983.

Ostriker, J.P., Acceleration of Galactic Cosmic Rays by Supernova Shocks in the Interstellar Medium, *A.I.P. Conf. Proc. No. 56*, eds. J. Arens, C. Max, C. McKee (American Institute of Physics), 1979.

Parker, E.N., Dynamics of the Interplanetary Gas and Magnetic Fields, *Ap. J.*, **128**, 664, 1958.

Parker, E.N., Dynamical Theory of the Solar Wind, *Sp. Sci. Rev.*, **4**, 666, 1965.

Peacock, J.A., Fermi Acceleration by Relativistic Shock Waves, *Mon. Not. astr. Soc.*, **196**, 135, 1981.

Peletier, D.P., S.A. Gary, A.F. Hogrefe, Mariner-Jupiter-Saturn Low Energy Charged Particle Experiment, *IEEE Trans. Nucl. Sci.*, **NS-24**, 795, 1977.

Pesses, M., R.B. Decker, T.P. Armstrong, The Acceleration of Charged Particles in Interplanetary Shock Waves, *Space Sci. Rev.*, **32**, 185, 1982.

Pesses, M., R.B. Decker, On Ion Acceleration in Interplanetary Quasi-Perpendicular Shock Waves, *J. Geophys. Res.*, **91**, 4143, 1986.

Pomerantz, M. A., *Cosmic Rays*, Van Nostrand Reinhold Co., Toronto, 1971.

Press, W.H., B.P. Flannery, S.A. Teukolsky, W.T. Vetterling, *Numerical Recipes*, Cambridge University Press, 1987.

Quenby, J.J., The Theory of Cosmic-Ray Modulation, *Sp. Sci. Rev.*, **37**, 201 1983a.

Quenby, J.J., Theoretical Studies of Interplanetary Propagation and Acceleration, *Space Sci. Rev.*, **34**, 137, 1983b.

Quest K.B., Simulation of Quasi-Parallel Collisionless Shocks, *Collisionless Shocks in the Heliosphere: Reviews of Current Research*, American Geophysical Union, 35, 1985.

Richardson, I.G., Spectra of 35-1600 keV Ions in Corotating Ion Enhancements at 1 AU, Preprint submitted to *Planet. Space Sci.*, 1985a.

Richardson, I.G., Anisotropy of >35 keV Ions in Corotating Particle Events at 1 AU, *Planet. Space Sci. Rev.*, **33**, 147, 1985b.

Richter, A., K. Hsieh, A. Luttrell, E. Marsch, R. Schwenn, Review of Interplanetary Shock Phenomena Near and Within 1 A.U., *Collisionless Shocks in the Heliosphere: Reviews of Current Research*, eds. B.T. Tsurutani, R.G. Stone, American Geophysical Union, Washington, D.C., 1985.

Russell, C.T., M.M. Hoppe, Upstream Waves and Particles, *Space Sci. Rev.*, **34**, 155, 1983.

Sanderson, T.R., R. Reinhard, P. van Nes, K.-P. Wenzel, Observations of 3-Dimensional Anisotropies of 35-1000 keV Protons Associated with Interplanetary Shocks, *ESA Preprint*, 1984.

Sanderson, T.R., R. Reinhard, P. van Nes, K.-P. Wenzel, Observations of 35-1600 keV Protons and Low-Frequency Waves Upstream of Interplanetary Shocks, *J. Geophys. Rev.*, **90**, 3973, 1985.

Scholer, M., Diffusive Acceleration, *Collisionless Shocks in the Heliosphere: Reviews of Current Research*, eds. B.T. Tsurutani, R.G. Stone, Washington, D.C., 1985.

Siscoe, G.L., Three-Dimensional Aspects of Interplanetary Shock Waves, *J. Geophys. Res.*, **81**, 6235, 1976.

Siscoe, G.L., Solar System Magnetohydrodynamics, *Solar-Terrestrial Physics*, Carovillano, R.L., J.M. Forbes, eds., D. Reidel Publishing Co., **104**, 1983.

Singer, S., M.D. Montgomery, Detailed Directional and Temporal Properties of Solar Energetic Particles Associated with Propagating Interplanetary Shock Waves, *J. Geophys. Res.*, **76**, 6628, 1971.

Smith, E.J., Interplanetary Shock Phenomena Beyond 1 A.U., *Collisionless Shocks in the Heliosphere: Reviews of Current Research*, eds. B.T. Tsurutani, R.G. Stone, American Geophysical Union, Washington, D.C., 1985.

Smith, E.J., J.H. Wolfe, Observations of Interaction Regions and Corotating Shocks Between One and Five AU: Pioneers 10 and 11, *Geophys. Res. Let.*, **3**, 137, 1976.

Smith, E.J., J.H. Wolfe, Pioneer 10, 11 Observations of Evolving Solar Wind Streams and Shocks Beyond 1 A.U., *Study of Interplanetary Traveling Phenomena (STIP)*, eds. M.A. Shea, D.F. Smart, S.T. Wu, D. Reidel Publishing Co., 1977.

Smith, E.J., J.H. Wolfe, Fields and Plasmas in the Outer Solar System, *Space Sci. Rev.*, **23**, 217, 1979.

Steinolfson, R.S., M. Dryer, Numerical MHD Simulation of Interplanetary Shock Pairs, *J. Geophys. Res.*, **80**, 1223, 1975.

Stone, E.C., The Voyager Missions to the Outer System, *Space Sci. Rev.*, **21**, 75, 1977.

Stone, E. C., R.E. Vogt, F.B. McDonald, B.J. Teegarden, J.H. Trainer, J.R. Jokipii, W.R. Webber, Cosmic Ray Investigations for the Voyager Missions; Energetic Particle Studies in the Outer Heliosphere-And Beyond, *Space Sci. Rev.*, **21**, 355, 1977.

Tan, L.C., G.M. Mason, Energetic Proton and Helium Fluxes Associated with Interplanetary Shocks and their Relationship to the Solar Wind Composition, *University of Maryland Preprint 86-205.*

Terasawa, T., Energy Spectrum and Pitch Angle Distribution of Particles Reflected by MHD Shock Waves of Fast Mode, *Planet. Space Sci.*, **27**, 193, 1979.

Toptyghin, I.N., Acceleration of Particles by Shocks in a Cosmic Plasma, *Space Sci. Rev.*, **26**, 157, 1980.

Tsurutani, B.T., E.J. Smith, K.R Pyle, J.A. Simpson, Energetic Protons Accelerated at Corotating Shocks: Pioneer 10 and 11 Observations from 1 to 6 AU, *J. Geophys. Res.*, **87**, 7389, 1982.

Tsurutani, B.T., E.J. Smith, D.E. Jones, Waves Observed Upstream of Interplanetary Shocks, *J. Geophys. Res.*, **88**, 5645, 1983.

Tsurutani, B.T., R.P. Lin, Acceleration of >47 keV Ions and >2 keV Electrons by Interplanetary Shocks at 1 AU, *J. Geophys. Res.*, **90**, 1, 1985.

Van Allen, J., Galactic Cosmic Ray Intensity from 1 to 9 A.U., *Geophys. Res. L.*, **3**, 425, 1976.

Van Allen, J., B. Randall, Interplanetary Cosmic Ray Intensity: 1972- 1984 and Out to 32 A.U., *J. Geophys. Res.*, **90**, 1399, 1985.

van Nes, P., R. Reinhard, T.R. Sanderson, K.-P. Wenzel, The Energy Spectrum of 35- to 1600-keV Protons Associated with Interplanetary Shocks, *J. Geophys. Res.*, **89**, 2122, 1984.

Vasil'yev, V.N., I.N. Toptyghin, A.G. Chirkov, Interaction of Energetic Particles with the Front of a Shock Wave in a Turbulent Medium, *Geomag. and Aero.*, **18**, 279, 1978.

Venkatesan, D., Cosmic Ray Picture of the Heliosphere, *APL Technical Digest*, January-March, 1985.

Venkatesan, D., R.B. Decker, S. Krimigis, Radial Gradient of Cosmic Ray Intensity From a Comparative Study of Data From Voyager 1 and 2 and IMP 8, *J. Geophys. Res.*, **89**, 3735, 1984.

Venkatesan, D., R.B. Decker, S. Krimigis, J. Van Allen, The Galactic Cosmic Ray Intensity Minimum in the Inner and Outer Heliosphere in Solar Cycle 21, *J. Geophys. Res.*, **90**, 2905, 1985.

Viñas, A.F., M. Goldstein, M. Acuna, Spectral Analysis of Magnetohydrodynamic Fluctuations near Interplantary Shocks, *NASA Technical Memorandum 85119*, November 1983.

Viñas, A.F., J.D. Scudder, Fast and Optimal Solution to the "Rankine-Hugoniot Problem", *J. Geophys. Res.*, **91**, 1986.

Wenzel, K.-P., R. Reinhard, T.R. Sanderson, E.T. Sarris, Characteristics of Energetic Particle Events Associated with Interplantary Shocks, *ESA Preprint*, 1984.